②

AD-A204 364

CALSPAN-UB
RESEARCH CENTER

TECHNICAL REPORT

DTIC
SELECTED
FEB 1 3 1989
D

CALSPAN
UB
RESEARCH CENTER

89   2   10   132

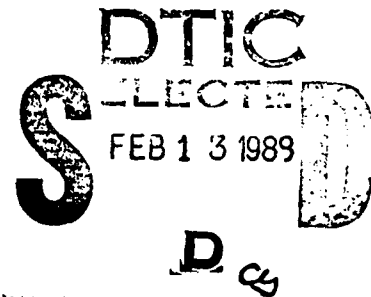**CALSPAN·UB**
RESEARCH CENTER

AFOSR·TR· 8 9 - 0 0 3 3

STUDIES OF THE STRUCTURE OF ATTACHED AND
SEPARATED REGIONS OF VISCOUS/INVISCID INTERACTION
AND THE EFFECTS OF COMBINED SURFACE ROUGHNESS AND
BLOWING IN HIGH REYNOLDS NUMBER HYPERSONIC FLOWS
FINAL REPORT

Covering Period 1 August 1985 - 1 June 1988
CUBRC Report No. 88682
December 1988

DTIC
S ELECTE
FEB 1 3 1989
D

Contract No. F-49620-85-C-0130

Prepared for:

AIR FORCE OFFICE OF SCIENTIFIC RESEARCH
BOLLING AIR FORCE BASE, D.C. 20332

Principal Investigator:

Michael S. Holden
Physical Sciences Department
Telephone No. (716) 631-6853

89 2 10 132

REPORT DOCUMENTATION PAGE

1a. REPORT SECURITY CLASSIFICATION		1b. RESTRICTIVE MARKINGS
Unclassified		
2a. SECURITY CLASSIFICATION AUTHORITY		3. DISTRIBUTION/AVAILABILITY OF REPORT
		Approved for Public Release
2b. DECLASSIFICATION/DOWNGRADING SCHEDULE		Distribution is Unlimited
4. PERFORMING ORGANIZATION REPORT NUMBER(S)		5. MONITORING ORGANIZATION REPORT NUMBER(S)
CUBRC REPORT NO. 88682		AFOSR·TR· 89-0033

6a. NAME OF PERFORMING ORGANIZATION	6b. OFFICE SYMBOL (If applicable)	7a. NAME OF MONITORING ORGANIZATION
Calspan-UB Research Center		AFOSR/Directorate of Aerospace Sciences
6c. ADDRESS (City, State and ZIP Code)		7b. ADDRESS (City, State and ZIP Code)
4455 Genesee Street Buffalo, NY 14225		Building 410 Bolling, AFB, DC 20332-6448

8a. NAME OF FUNDING/SPONSORING ORGANIZATION	8b. OFFICE SYMBOL (If applicable)	9. PROCUREMENT INSTRUMENT IDENTIFICATION NUMBER
AFOSR	NA	F49620-85-C-0130

8c. ADDRESS (City, State and ZIP Code)	10. SOURCE OF FUNDING NOS.			
BlCT 410 BOLLING AFB DC 20332-6448	PROGRAM ELEMENT NO.	PROJECT NO.	TASK NO.	WORK UNIT NO.
11. TITLE (Include Security Classification) Studies of the structure of attached & separated regions (Cont. #16)	61102F	2307	A1	

12. PERSONAL AUTHOR(S) M.S. Holden, R. Bergman, J. Harvey, G. Duryea, & J. Moselle

13a. TYPE OF REPORT	13b. TIME COVERED	14. DATE OF REPORT (Yr., Mo., Day)	15. PAGE COUNT
Final	FROM 8/1/85 TO 6/1/88	88,12,02	126

16. SUPPLEMENTARY NOTATION (title continued) of Viscous/Inviscid interaction and the effects if combined surface roughness and blowing in high Reynolds number hypersonic flows.

17 COSATI CODES			18 SUBJECT TERMS (Continue on reverse if necessary and identify by block number)
FIELD	GROUP	SUB. GR	Holographic Interferometry, Hypersonic flow,
	20.04		Boundary layer experiment

19. ABSTRACT (Continue on reverse if necessary and identify by block number)

Two studies have been performed. The first examined the detailed structure of a hypersonic boundary layer over a cone/flare configuration. The second study measured heat transfer, pressure and skin friction over a blowing and roughness model. A new holographic interferometer system was designed and constructed for the studies.

20. DISTRIBUTION/AVAILABILITY OF ABSTRACT	21 ABSTRACT SECURITY CLASSIFICATION
UNCLASSIFIED/UNLIMITED ☒ SAME AS RPT. ☐ DTIC USERS ☐	Unclassified

22a. NAME OF RESPONSIBLE INDIVIDUAL	22b. TELEPHONE NUMBER (Include Area Code)	22c. OFFICE SYMBOL
LEN SAKELL	202-767-4935	AFOSR/NA

DD FORM 1473, 83 APR   EDITION OF 1 JAN 73 IS OBSOLETE   UNCLASSIFIED

AFOSR-ABSTRACT

This final report describes the research conducted under Contract F-49620-85-C-0130 from August 1985 to June 1988. Earlier work conducted under this contract was reported in Annual report number 86681[1] and in papers AIAA-86-0267[2] and AIAA-86-0384[3] presented at AIAA meetings. The studies reported here are a continuation of the earlier work directed toward the detailed experimental investigation of the structure of attached and separated boundary layers in hypersonic boundary layers. Our most recent studies comprised of two investigations. The first was a study to examine the detailed structure of the hypersonic boundary layer over a large cone/flare configuration. Here the emphasis was on the development and use of instrumentation with which to obtain flow field measurements of the mean and fluctuating properties of the attached and separated shear layers. We describe the development and use of holographic interferometry and electron beam techniques in the high Mach number and Reynolds number environment developed in the shock tunnel. In the second study, detailed measurements of heat transfer, pressure and skin friction were made on a unique "blowing and roughness" model which was constructed to simulate the aerothermal phenomena associated with a rough ablating maneuverable re-entry vehicle. In this latter study, which was conducted in conjunction with an AFWAL program, the emphasis was placed on the development and use of unique heat transfer and skin friction instrumentation to obtain measurements of the combined effects of blowing and roughness and to understand how such effects influence boundary layer separation in regions of shock wave/boundary layer interaction. Each of the two programs were focused around providing the information with which to construct and evaluate the modeling which is required in the time-averaged Navier-Stokes equations to predict the structure of compressible hypersonic boundary layers in regions of strong pressure gradient, shock wave/boundary layer interaction and flow separation over smooth, rough and ablating surfaces.

1. "Shock Wave/Turbulent Boundary Layer Interaction in High-Reynolds Number Hypersonic Flows," M.S. Holden, et al, CUBRC Report No. 86681, July 1987.
2. "A Review of Aerothermal Problems Associated with Hypersonic Flight," M.S. Holden, AIAA 24th Aerospace Sciences Meeting, January 6-9, 1986.
3. "Studies of the Heat-Transfer and Flow Characteristics of Rough and Smooth Indented Noseshapes. Part I. Steady Flows," M.S. Holden, AIAA 24th Aerospace Sciences Meeting, January 6-9, 1986.

An electron beam was constructed, based on the original design concept developed by Harvey and Lin, to obtain density and temperature measurements as well as density fluctuation measurements in high Reynolds number turbulent flows for local ambient pressure levels of up to 100 torr. This electron beam differs in three important respects from earlier guns: 1) it can be operated at significantly higher pressure, 2) it is so compact that it will fit within wind tunnel models 3) it uses novel approaches to focus the beam outside the gun and isolate the guns interior from the test environment. Multiple systems are used to obtain spatially resolved measurements across the boundary layer which provide the capability to obtain turbulent scale size measurements from correlations of the data. The gun is operated in a nitrogen environment and has been calibrated successfully up to 100 torr. The system has a frequency response of up to 700 kHz.

A new holographic interferometer system has been designed and fabricated specifically for use with Shock Tunnel studies of viscous/inviscid interaction phenomena in hypersonic flows. A reconstruction and analysis system has also been assembled and used to process the holograms recorded during the studies of blowing and roughness.

The unique "blowing and roughness" heat transfer and skin friction instrumentation developed during this contract was used successfully to measure surface roughness and blowing on turbulent boundary layers over a cone at Mach numbers from 11 to 16. Two types of roughness and blowing heat transfer gages, a calorimeter gage and a multi-element thin film gage, were developed during this contract. The calorimeter gage was constructed with a silver calorimeter element containing two roughness elements and insulated injection passages molded into it. A nickel thin film resistance thermometer is to sense the temperature of the calorimeter element. This gage was used successfully to obtain average local heating measurements to determine the effects of mass addition on cone heating. The distribution of heating over and between the roughness elements was determined for a range of blowing rates and freestream conditions with the multi-element thin film gage. The thin film elements were distributed over the roughness elements and on the base between the roughness elements and the injection passages. A new skin friction gage, in which there was blowing through the floating sensing element, was used successfully to measure the effects of blowing and roughness on surface shear. Again two roughness elements were molded into the surface of the transducer and injection passages are incorporated into the gage. The results

iv

of the measurements with these gages are presented together with comparisons with earlier measurements at lower Mach numbers and prediction techniques.

TABLE OF CONTENTS

TABLE OF CONTENTS (Cont.)

LIST OF FIGURES

LIST OF FIGURES (Cont.)

LIST OF FIGURES (Cont.)

xi

LIST OF FIGURES (Cont.)

Section I

INTRODUCTION

In the development of advanced prediction techniques required to design and predict the aerothermal loads on sophisticated, advanced Air Force maneuverable airbreathing hypersonic vehicles, there are a number of key flow/field and flow/surface interaction phenomena that must be modelled which require the insight and measurement of detailed experimental study. The modelling of the turbulent flow structure of the flow over transpiration-cooled and rough ablating surfaces is an area where a detailed understanding of the mixing process between the injected fluid, the roughness elements, and the air at the base of the turbulent boundary layer is required. Likewise, in the external flow, the development of turbulent scale size and intensity in a hypersonic turbulent boundary layer subjected to strong pressure gradients and incident shocks remains a major unresolved problem. The current program is directed toward providing detailed surface and flow field measurements to aid in the resolution of these two issues.

During the course of the current and previous AFOSR contract, a detailed review was made of the intrusive and non-intrusive measurement techniques which coulc be applied to define the flow field in the high dynamic pressure and temperature environment generated in regions of shock wave-boundary layer interaction in hypersonic flows. On the basis of this study, we began a program of research and development to provide the flow field measurements necessary for the models of turbulence required to predict the characteristics of regions of strong shock wave/boundary layer interaction. We selected and developed holographic interferometer techniques to provide an improved flow visualization technique and a method to provide quantitive flow field density measurements. We also developed total temperature and pitot pressure probes with sufficient robustness and accuracy to provide important mean flowfield measurements.

Amongst other measurement techniques examined were laser velocimetry, laser-induced fluoresence (LIF), hot wire and hot film techniques, and mean and fluctuating density measurement using an electron beam. While both LIF and velocimetry techniques have been shown to work well in low speed flows, these techniques require significant development and investment in intrumentation. Hot film rather than hot wire techniques would appear to hold promise for intrusive fluctuation measurements, although further developments are required. Such a development program is currently

1

being conducted in conjunction with the graduate program supported by the NAA/DOD hypersonics training grant. Recent developments in electron beam technique has made this technique attractive for mean and fluctuating density measurements and we selected this technique for turbulence measurements in our Shock Tunnels. We outline our initial development of this technique and further developments in holographics interferometry in the following section of the report.

The major accomplishments of the current contract have been the development and use of unique heat transfer and skin friction instrumentation to obtain measurements of the combined effects of roughness and blowing on the heat transfer, skin friction and flap forces on a manuverable re-entry vehicle configuration in hypersonic, high Reynolds number flows. In these studies which were conducted in conjunction with an AFWAL program, we also developed a unique transpiration-cooled model, the roughness and blowing characteristics of which could be varied to provide the measurements required to evaluate the separate and combined effects of blowing and surface roughness. The roughness characteristics, the effects of bluntness and angle of attack, the distribution of blowing and the flap configuration could all be varied independently to provide a broad range of measurements for code evaluation. The experimental studies were conducted at freestream Mach numbers from 11 to 16, for Reynolds numbers up to 100E6 and wall-to-freestream temperature ratios from 0.1 to 0.3. The roughness Reynolds numbers $\left(U_{\tau} k / \mathcal{V}_{w} \right)$ were varied from 20 to 300 covering the transitional to fully rough regime. Nondimensional blowing rates $B' = \dot{m} / \rho u C_H$ were varied from .1 to 5 to simulate small blowing rates to blow-off conditions. In part two of the report, we describe in detail the models instrumentation and the initial results from the first series of studies.

Large surface ablation resulting from heat transfer rates generated on the windward ray of the heat shield close to the nosetip and on the control surfaces of MRVs flying at high angles of attack will be of critical concern to the designer of missiles that maneuver during re-entry. Unlike conventional ballistic missiles where the blowing from the heat shield is relatively small, the development of small MRVs with biconic frustum configuration, coupled with the requirements to fly at large angles of attack and use highly deflected control surfaces, has made an understanding of the aerothermodynamics of rough, highly ablating thermal protection and control systems of considerable importance. The deployment of highly ablating decoys has raised similar problems. To develop an accurate predictive capability to describe the ablation rates

2

of the nosetip, heat shield, and control surfaces, it is necessary to understand and model the separate and combined effects of surface blowing and surface roughness. Our recent studies of roughness, shape and spacing effects on ablating and non-ablating MRV configurations suggest not only that the subsonic studies are inapplicable to the heating of heat shields in hypersonic flow, but also that the basic modelling of the roughness drag and the mechanisms of heating in the theoretical models is highly questionable.

The effects of combined blowing and surface roughness on the aerothermal performance of the control surfaces of MRVs are potentionally more important than those on the heat shield. Both surface roughness and blowing on the frustum act to reduce flap force by decreasing the momentum close to the surface and thickening the boundary layer immediately upstream of this flap. The large pressure gradients and pressure levels generated on the deflected flap can cause a dramatic thinning of the boundary layer along the flap at a point of peak pressure which results in large local heating levels. These heating rates are enhanced by large surface roughness effects resulting from locally large K/δ's.

The introduction of mass at the base of the boundary layer results in a reduction in momentum in the wall layer which, like roughness, will make the boundary more susceptible to separation and ultimately result in a reduction in flap force as shown in figures 1 and 2. However, injecting mass into the boundary layer will also severely distort the temperature and velocity distribution at the base of the boundary layer which has the potential to cause a reduction in heat transfer and skin friction to the wall. Because momentum reduction on rough walls at the base of the boundary layer results principally from the drag of the roughness elements, the introduction of mass at the rough wall could significantly change the basic mechanisms that control momentum and energy exchange. Our experience with transpiration-cooled nosetips[1] as well as those of Voisinet[2] on wind tunnel walls suggests that calculating the combined effects of mass addition and surface roughness (as is done in most prediction techniques) by using the product of the 'influence factors' (based on measurements of the separate effects of roughness and blowing) is invalid.

As demonstrated in studies by Holden[3], the entropy layer (a region of low momentum gas generated by the air processed by the highly curved section of the shock generated by a blunt nosetip) can cause a dramatic reduction in the forces

3
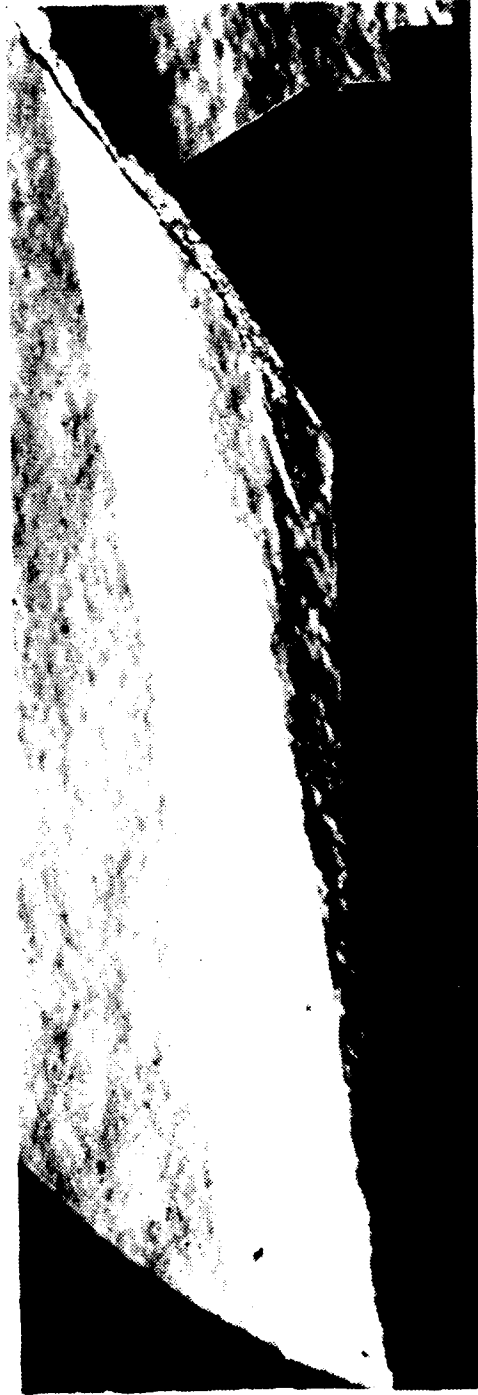
(a) UNSEPARATED

(b) SEPARATED

Figure 1   FLOW OVER THE ROUGH MRV CONFIGURATION WITH A 30° FLAP DEFLECTION

4
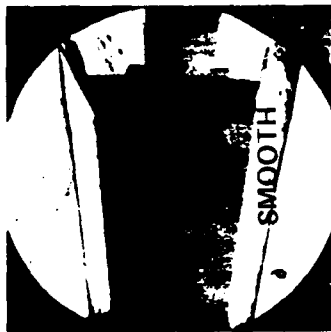
FLAP FORCE

$$\frac{c_{N_{ROUGH}}}{c_{N_{SMOOTH}}} = 0.33$$

$c_{N_{ROUGH}} = 0.175$

$c_{N_{SMOOTH}} = 0.530$
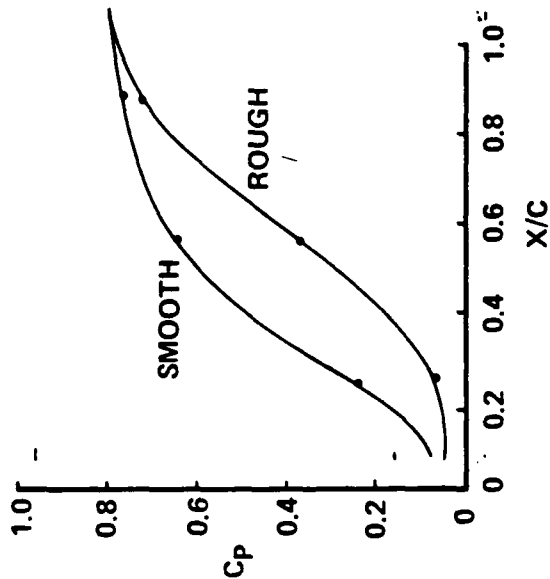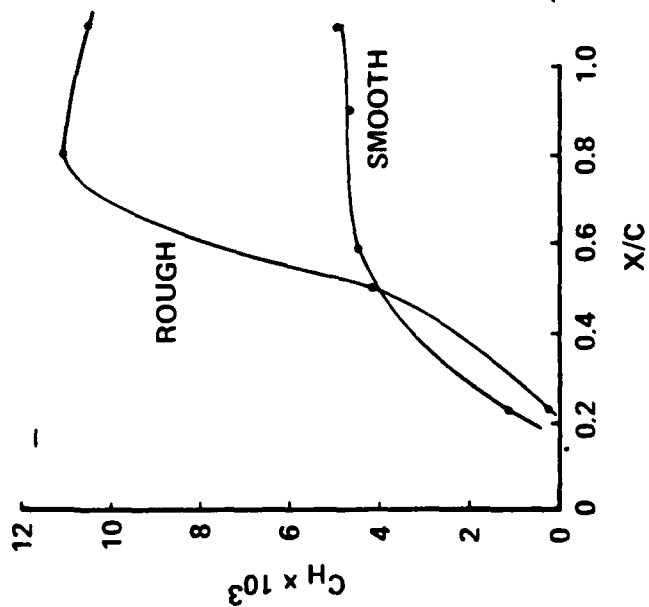
Figure 2   EFFECT OF SURFACE ROUGHNESS ON FLAP FORCES' HEATING AND PRESSURE

5

generated by the control surfaces. While increasing the angle of attack can significantly improve control-surface effectiveness in the windward plane by sweeping the entropy layer to the leeside of the vehicle, the effectiveness of a flare surface on the leeside of the vehicle can be significantly reduced.

To develop prediction schemes that will accurately describe the effects of combined roughness, blowing and the entropy layer on the aerothermal performance of small MRVs and highly ablating decoys, we must conduct experimental studies under hypersonic, high-Reynolds-number, and cooled-wall conditions. The models used represent typical bluntness characteristics of the vehicles of interest and should be constructed with well-defined roughness and blowing characteristics. The correlations of the measurements from these studies should then be used to directly evaluate the accuracy of aerothermal models currently in use in "shape change" codes while individual sets of measurements should be compared with more detailed calculations of combined roughness and blowing on sharp and blunt configurations.

Section 2

THE DEVELOPMENT AND USE OF ELECTRON BEAM AND HOLOGRAPHIC INTERFEROMETER TECHNIQUES FOR SHOCK TUNNEL STUDIES

2.1 INTRODUCTION

The rapid developments in the numerical solution of the Navier Stokes equations has brought into sharp focus the inadequency of currently available turbulence models for flows with strong pressure gradients, particularly those generated in regions of shock wave/boundary layer interaction in hypersonic flow. While surface measurements such as skin friction and heat transfer may aid indirectly in the discrimination of turbulence models which do or do not work, only by obtaining mean and fluctuating flow field quantities is it possible to directly contribute in the formulation and evaluation of turbulence models. This viewpoint led us four years ago to begin a review and an evaluation of the intrusive and non-intrusive measurement techniques which could be used to define the mean and fluctuating flow field in the high dynamic pressure and temperature environment developed in regions of shock wave/boundary layer interaction in high Reynolds number hypersonic flows. We selected and developed total temperature and pressure with sufficiently small size, robustness and accuracy to provide important flowfield measurements. We began the development of laser holography to provide flow field visualization and quantative density and temperature measurements. Finally after examining laser velocimetry, laser-induced floresence, hot wire and hot film methods and the electron beam technique, we selected the hot film and electron beam techniques to develop for use in the shock tunnel. The hot film technique appears to hold promise for intrusive fluctuation measurements and is currently being developed in a program supported by the NASA/DOD hypersonics training program. The development of the electron beam technique for high Reynolds number flows by Harvey and Lin provide the starting point for our development of this technique as described below. We follow this description with our most recent research with holographic interferometry and in particular its use in the blowing and roughness studies.

2.2 ELECTRON BEAM FLUORESCENCE TECHNIQUE TO STUDY HYPERSONIC FLOWS

2.2.1 Introduction

The electron beam fluorescence technique (EBFT) is a well-established method for investigating rarified hypersonic flow fields (Figure 3). The non-intensive character of this optical measuring technique makes its application to higher density flow especially attractive. Of equal importance to the non-intensive nature is the inherent high frequency response, typically greater than 1 MHz, compared with that of hot wire anemometry, which is usually limited to about 250 kHz. Many earlier studies in which EBFT has been applied to less rarified and, in several cases, turbulent flows provide a wealth of useful information on the application of the technique to aerodynamic problems.

Figure 4 shows a schematic of the equipment used to apply the EBFT in a wind tunnel experiment. Briefly, the technique involves firing a highly collimated beam of high energy electrons into the test gas flow; the interaction of the electrons with the gas molecules gives rise to optical-band radiation that can be analyzed spectroscopically to obtain estimates of rotational temperature, vibrational temperature or the molecular number density of the excited species. The illustration shows the beam emerging through a small hole in the model's surface into the region to be measured. When the beam impacts into the model surface, a cloud of secondary electrons is likely to be emitted near the surface, influencing the fluorescence in that region and degrading the accuracy of the measurements. Constructing the model onto a graphite surface minimizes the secondary electron emission.

If the beam does not strike the model, it is usually terminated some distance away from the test region in a graphite "Faraday Cup." This is an insulated target grounded through a resistor. The beam current can thus be measured by noting the potential of the cup. The cup also serves to arrest the beam safely since it can be a potent source of X-rays if it strikes a dense metallic object, or it can cause thermal damage.

The density determination is based on the observed relationship between the fluorescent intensity of the band system and the molecular number density. This

8

FLOW

ELECTRON GUN

LENS

SLIT

FILTER

OR SPECTROGRAPH

PHOTOMULTIPLIER
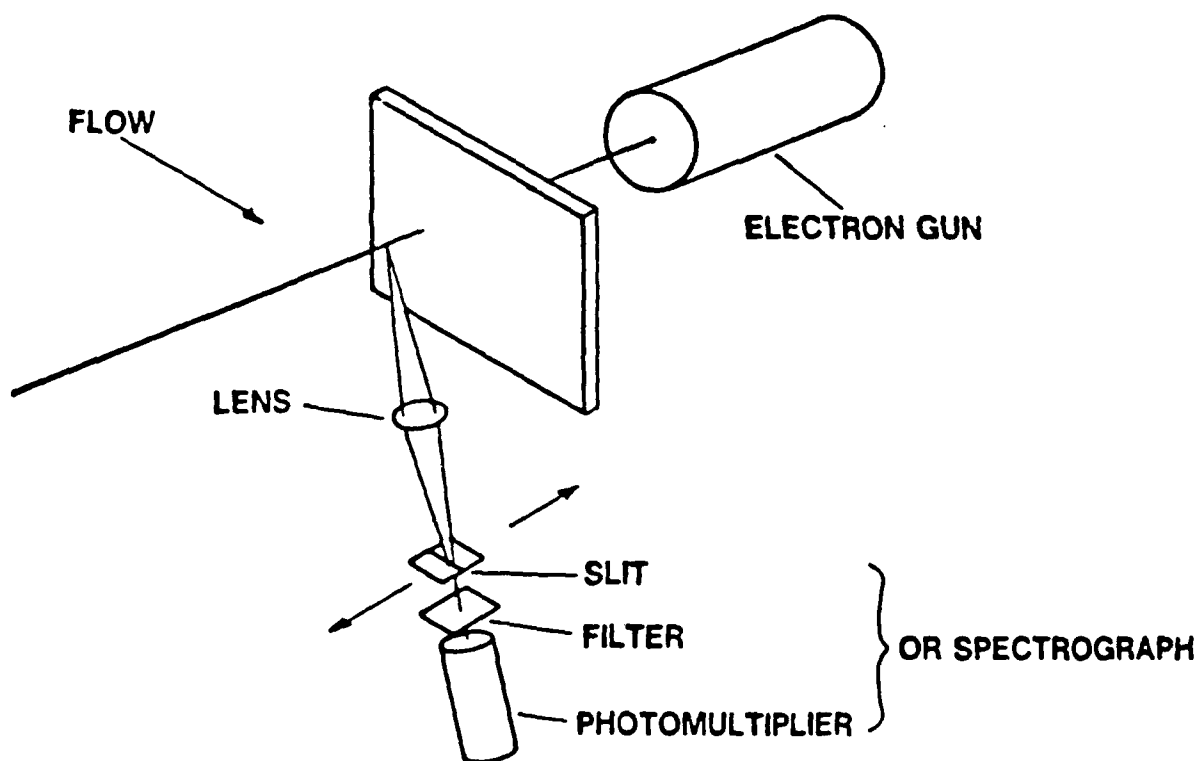
Figure 3   ELECTRON BEAM FLUORESCENCE TECHNIQUE

9
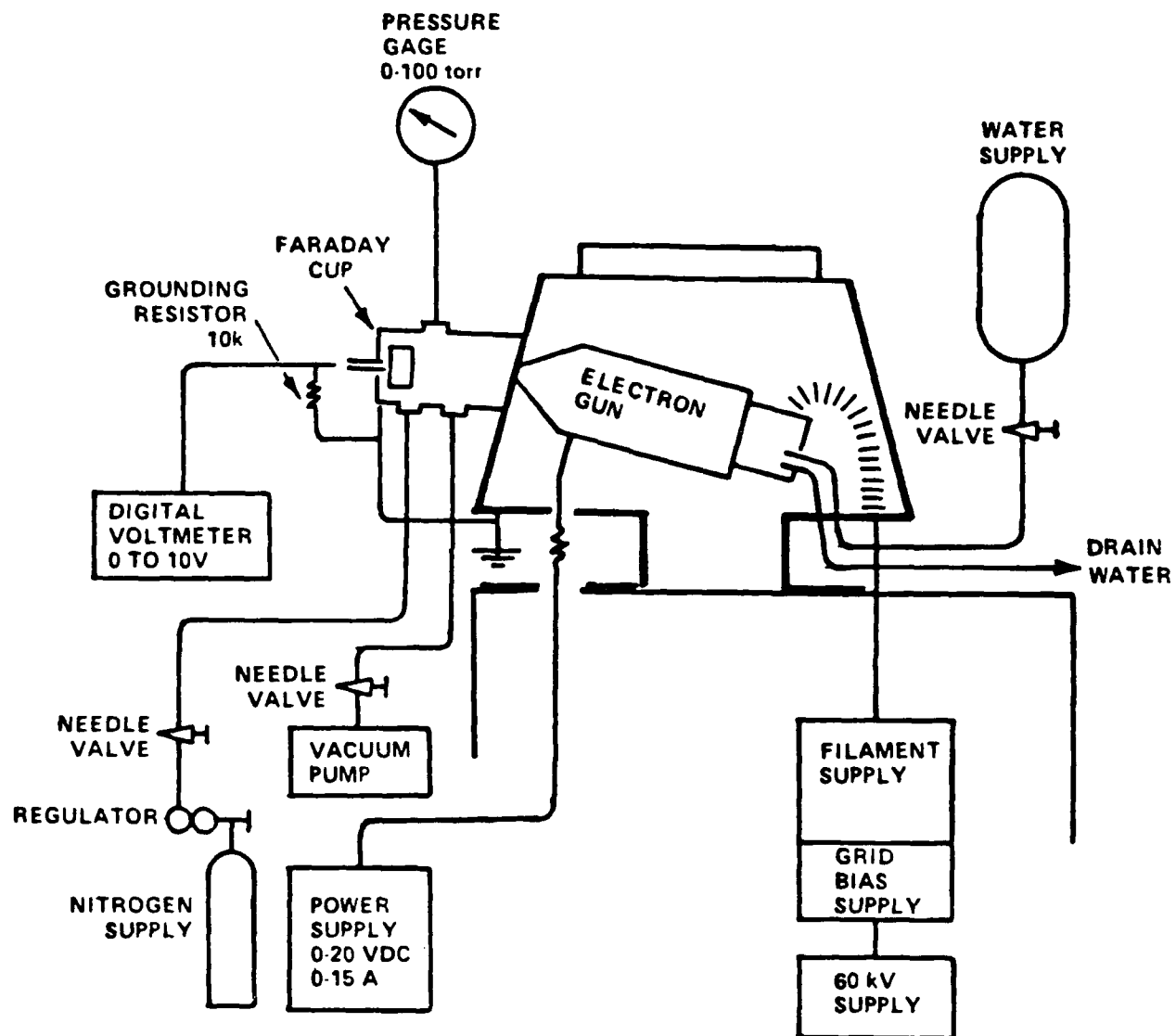
Figure 4   SCHEMATIC OF PRELIMINARY TEST EQUIPMENT

10

relationship is often obtained by calibration using the same optical arrangement over a comparable range of gas number densities and temperatures. Although theoretical calibration schemes also exist, there remain constants due to both the optical geometry and the beam accelerating voltage that have to be determined experimentally. The part of the spectrum of the emitted light selected for the measurement is chosen on the basis of:

o being sufficiently bright so that it can be easily detected, and

o giving a monotonic relationship between fluorescence intensity and density. In most instances, a nearly linear relationship can be achieved for a practical range of densities by using an appropriate filter.

Rotational and vibrational temperatures are determined by measuring the relative intensities of the rotational lines and vibrational bands of the emitted light. To do the former with any degree of precision, a high dispersion spectrograph is needed which replaces the filter and photomultiplier shown in Figure 4. Vibrational temperatures can be measured by splitting the light from the observed part of the beam between two or more photomultipliers, each with appropriate narrowband filters that select different vibrational bands in the spectrum.

An electron gun has been designed, built and tested at CUBRC. This gun provides a high quality electron beam, and it has been demonstrated to work at 50 kV with external pressures up to 100 torr. The technique of isolating the gun from the external environment with a thin graphite diaphragm through which the beam burns a hole has been shown to work well. Beam currents of just under 0.4 mA with the diaphragm in place have been recorded with low filament currents. Higher beam currents should be readily obtained with a hotter filament.

An optical system with one photomultiplier was also constructed and a three-photomultiplier system designed.

2.2.2   Electron Gun

The electron gun is similar to one used by Lin and Harvey.[4] However, this gun differs in two important respects: (1) it is compact so that it will fit in a wind tunnel and (2) it uses a novel approach to isolate the gun's interior vacuum from the test environment.

The first section is a conventional three-electrode design, namely, a directly heated tungsten cathode, a grid and a grounded anode. The cathode and grid operate at a high negative potential of up to -50 kV and are supported by a ceramic insulator. Shielded cables connect the cathode and grid to a remote power supply; additional circuitry provides a regulated grid bias voltage of -160 V to -1450 V and 3 VDC (2.8 A) filament voltage. This section of the gun is continuously evacuated using a diffusion vacuum pump. The electron beam forms at the tip of the cathode and is focused electrostatically by the shaped grid and the strong electrostatic field induced by the flat anode. The spacing between the grid and the anode is typically 6.6 mm (0.26 in.) for 30 kV and 11 mm (0.433 in.) for 50 kV. Except for the filament, the gun is totally axisymmetric. The center of the anode has a hole through which the beam passes and continues on to the focusing electromagnet.

The gun is constructed so that a minimum number of physical adjustments is required. All the parts are precisely made and can be relocated accurately with respect to each other when reassembled. The physical adjustments are made entirely by measurements during gun assembly and cannot be altered when it is running.

The beam is required to make its own hole by burning through the thin diaphragm. A fresh insert is used each time a major change is made to the gun. The precision of the gun permits grid spacing changes and gun reassembly without having to replace the diaphragm. Except for the magnetic pole pieces, nonmagnetic materials are used for all gun components.

A commercial electron microscope filament assembly was chosen because it is supplied on a mount with convenient centering screws. Pre-heating the vacuum (10^{15} torr) to its operating temperature is advised before centering because the filament distorts when it is first used. This is conveniently done using a microscope fitted with a graticule. The setting of dimension (H) with a microscope is also recommended.

12

2.2.3   Optical System

An optical system comprising a lens, a mirror, an interference filter, a slit assembly, and photomultipliers was designed and built to measure wind tunnel fluctuating density. The lens focuses on the beam with the optical axis perpendicular to both the beam axis and the mean flow direction. Light from the lens is reflected into the stream direction by an inclined mirror and forms an X4 image at the slit plane after passing through the interference filter. The single photomultiplier is placed on the optical axis beyond this variable aperture slit. In the three-detector system, three fixed slits are machined into a mask and a system of small mirrors transmits light from the outer two mirrors to two of the photomultipliers. The optical system was designed to maximize the light-gathering capability to combat the signal-to-noise problem that is associated with resolving the highest frequency components of the fluctuating density.

2.2.4   Testing Electron Gun

The electron gun was first tested in a small stainless steel test chamber that was attached and sealed to the electron gun model covering the graphite region. A schematic of the experimental setup is shown in Figure 4. The electron gun, minus the diaphragm, was operated with a filament/grid setting of L = 10 mm and H = 2.1 mm and between 25 and 30 kV. A very fine beam of up to 0.56 mA was produced with 2.5 A filament current. A diaphragm was then inserted and a hole burned. To focus the beam sharply on the graphite, a current of 7.5 A was required. The hole was burned quickly (1 minute); even so, subsequent pressure tests demonstrated that a small hole had been produced. (Slow, careful burning is recommended if minimum size holes are required for the best isolation of the gun from the external environment.) For a range of external pressures up to 82 torr, ratios in the order of 10^6 were recorded between the external and pumping manifold pressures. For example, 7.4×10^{-5} torr was measured for the highest pressure that is an acceptable level for reasonable filament life. A vacuum of better than 10^{-4} torr (and preferably better than 10^{-5} torr) is required.

A second diaphragm was installed and pierced and a series of photographs taken. The gun operated successfully at pressures up to 100 torr. After a number of runs, beam flickering signaled filament failure; thus, a new filament was installed with settings of L = 6.6 mm and H = 1.9 mm, which are appropriate for a 30 kV "hole

13

burning" operation. A hole was produced, the gun dismantled, and the filament reset for 50 kV operation with L = 11 mm and H = 2.1 mm. When the gun was restarted, a beam of 0.2 mA at 50 kV formed, passing through the previously cut hole in the diaphragm. No attempt was made to increase the beam current by raising the filament current above 2.4 A. This demonstrated that the gun could be dismantled, the grid adjusted, and the gun could be reassembled without replacing the diaphragm. For the beam to pass through the hole, it has to stay aligned to within 0.001 inch.

The electron beam system is statically calibrated in the test section of the tunnel (or in a test chamber) by evacuating the vessel to remove the oxygen and then filling the chamber to a pressure giving the required density. The photomultiplier output is recorded for a series of density levels providing a calibration similar to that shown in Figure 5. By using multiple optical systems (we use three) to view the beam, simultaneous measurements can be obtained across the boundary layer and spatial correlations can be obtained to provide information on turbulent scale size. A photograph of electron beam mounted together with a 6° cone model is shown in Figure 6a. Also shown with the photograph are the total temperature and pressure rakes used for the boundary layer survyes. Figure 6b shows the electron beam in operation. The frequency response of our system is close to 700 kHz and typical spectral density measurements are shown in Figure 7.

2.3 STUDY OF HYPERSONIC BOUNDARY LAYER INTERACTIONS USING HOLOGRAPHIC INTERFEROMETRY

2.3.1 Introduction

CUBRC has investigated the use of holographic interferometry to study regions of shock wave/boundary layer interaction in hypersonic shock tunnels. The interferograms of the complex flow fields provide a good qualitative basis for evaluating some of the important phenomena that control the characteristics of these flows. However, the quantitative evaluations of the interferograms are made difficult by edge effects and three-dimensional flow effects on two-dimensional models and by refraction effects in regions of high density gradients close to the wall. The disagreement between density measurements and simple prediction techniques for turbulent flat plate boundary layers indicates that further analyses and experiments are required to develop an understanding of both the refraction and three-dimensional effects.
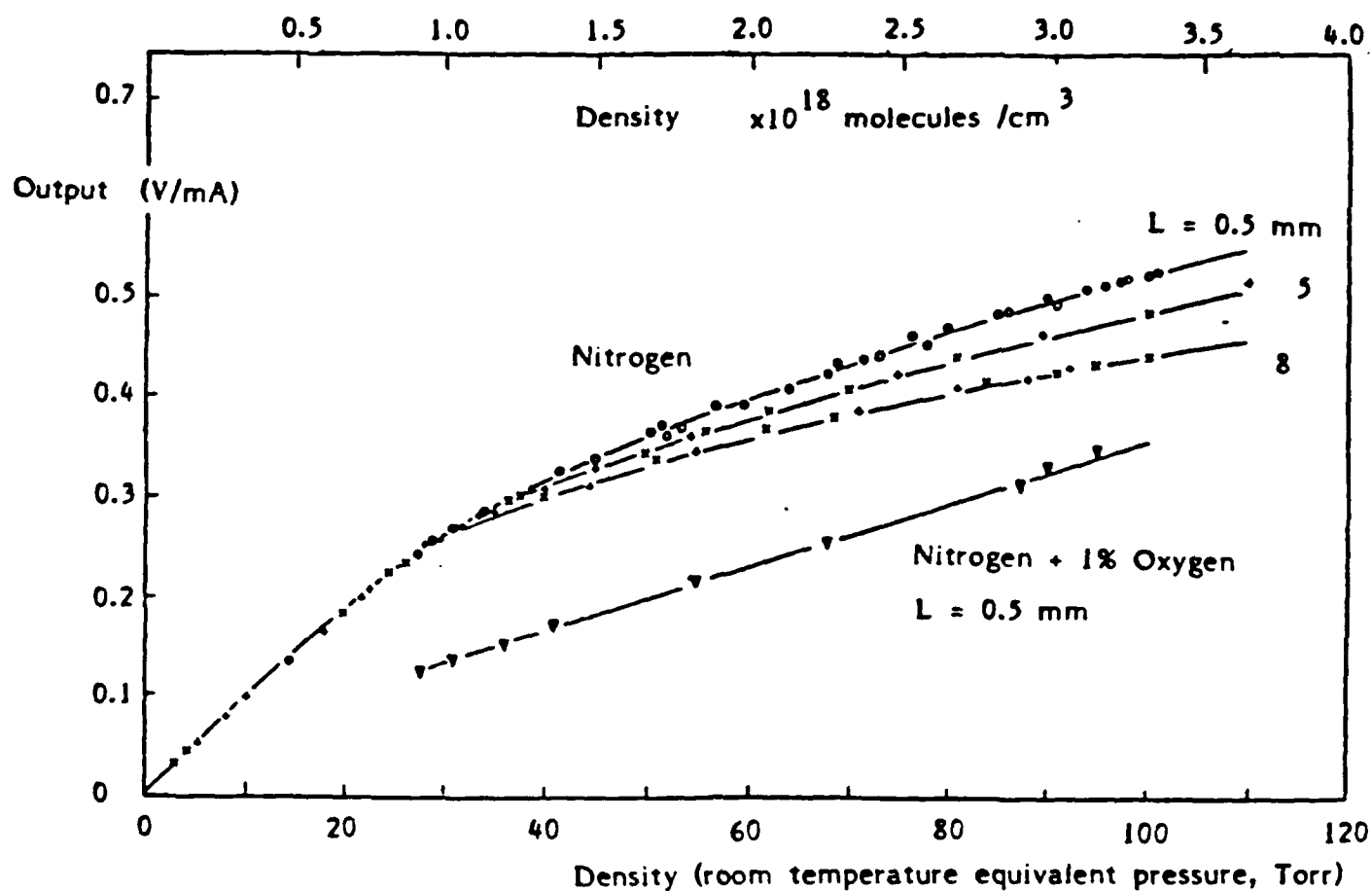
Figure 5   CALIBRATION OF THE ELECTRON BEAM - PHOTOMULTIPLIER
OUTPUT AGAINST GAS DENSITY

Figure 6(a) ELECTRON BEAM AND TOTAL TEMPERATURE AND PITOT PRESSURE
RAKES ON 6° CONE INSTALLED IN CALSPAN'S 96'' SHOCK TUNNEL
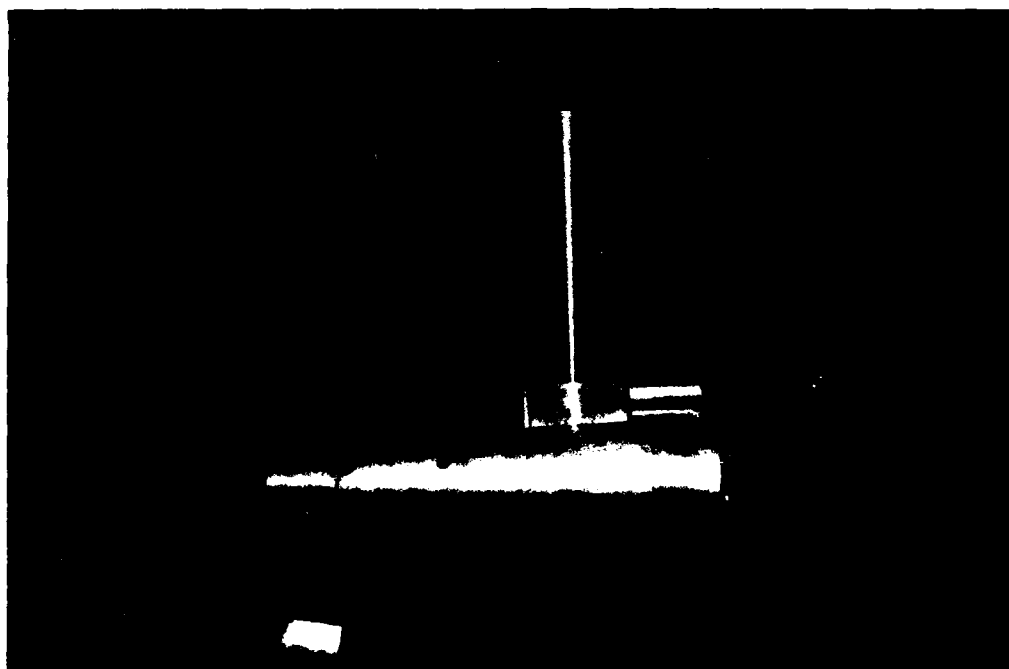
Figure 6(b) ELECTRON BEAM IN OPERATION ON 6° CONE MODEL
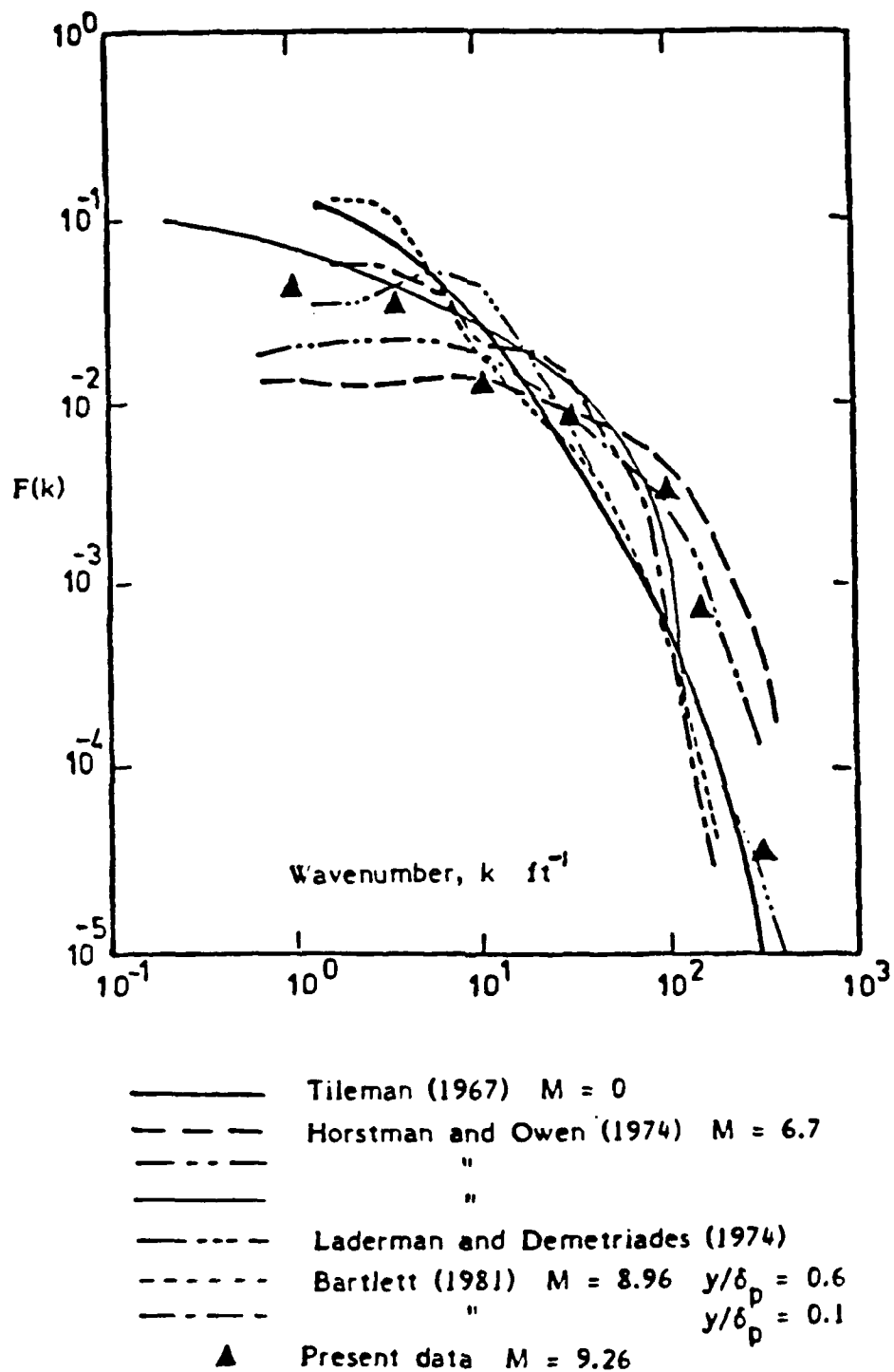
Figure 7 AVERAGED SPECTRAL DENSITY PROFILES COMPARED WITH
AVAILABLE DATA

17

The holographic recording system used in the holographic studies was loaned to CUBRC by the Air Force Flight Dynamics Laboratory (AFFDL), Wright-Patterson Air Force Base, Ohio. Subsequently, an improved system was constructed by CUBRC for use with its fundamental research programs.

2.3.2   Basic System

Holograms were made using a pulsed ruby laser that was Q-switched passively with a dye cell to produce single 25-nanosecond (nominal) light pulses. Both single plate and dual plate techniques are required to record holograms, which are subsequently used in the playback step to obtain shadowgrams, schlieren photographs and interferograms of the shock tunnel tests. The optical reference conditions are taken for both atmospheric and tunnel "pump down" conditions; the latter condition is needed to assess the optical effect of loading the test chamber windows. During the actual recording of the holograms, the shock tunnel test section was nearly at vacuum causing window stress by atmospheric pressure.

2.3.3   Shock Tunnel Installation

The holographic system was positioned and aligned with the Toepler schlieren system of the shock tunnel facility as shown in Figure 8. A 20-power microscope objective was used to expand the laser beam to fill a 15-inch-diameter parabolic mirror. A collimated beam reflected from the parabolic mirror was directed through the windows of the shock tunnel, captured by a second parabolic reflector on the opposite side of the tunnel, and directed toward the hologram recording plane. Thirty percent of the incident radiation was reflected from the front surface of the beam splitter; this light was used to establish the scene beam, and the remaining 70 percent was directed over the shock tunnel by specially built beam elevation towers. Natural divergence of the ruby laser beam caused an approximate 50 percent reduction in the intensity of the light entering the collimator, so the net intensities of the scene and reference beams in the hologram plane were nearly equal.

The ruby laser in the recording system is a Korad, single-oscillator system that is passively Q-switched with a Kryptocine dye cell. A 15-milliwatt, continuous-wave (CW), helium neon laser is mounted behind the rear reflector of the ruby laser cavity and is aligned so that both laser beams are coaxial. The CW laser is used to

18
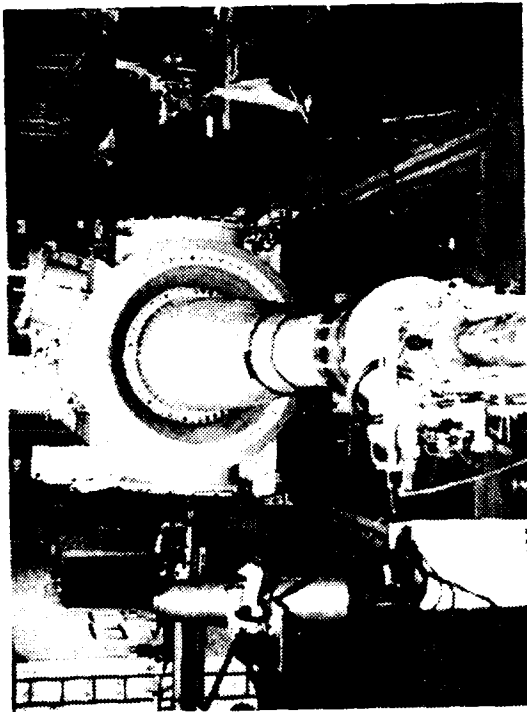
96- INCH HYPERSONIC SHOCK TUNNEL WITH LASER HOLOGRAPHIC SYSTEM INSTALLED
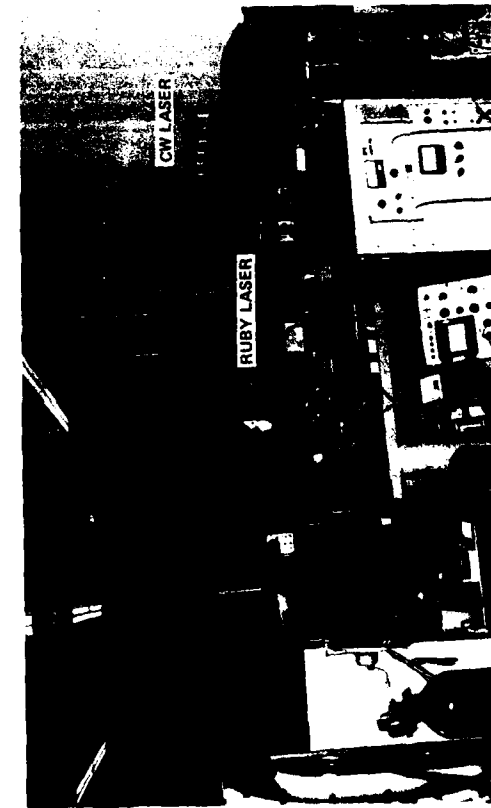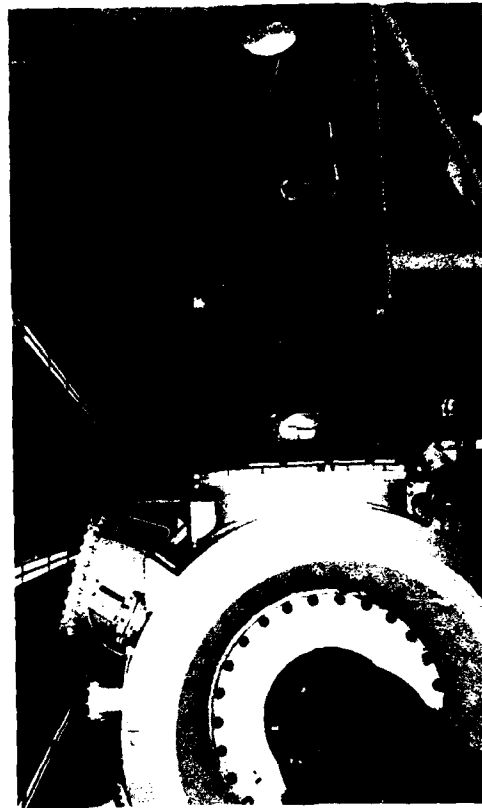
RECEIVING OPTICS

SENDING OPTICS

Figure 8 LASER HOLOGRAPHIC SYSTEM

19

align all the components in the recording system, and to preview the holograms _in situ_ prior to analyzing them in detail using a separate playback system.

Figure 9 shows the hologram playback system. A duplication of the holographic reference beam is established by directing the output of an argon ion, CW laser into a beam expander-collimator similar to the one used in the recording system. The same dual hologram holder is used to position the holograms, and a positive, f/8 lens is used to image the reconstructed object light waves directly into the field of a 20X telescope. The 20X telescope is the imaging component of an x-y microcomparator. This system is used to measure the interferometric fringe shifts for both single plate and dual plate applications, as well as to obtain photographic enlargements of selected apertures for the flow fields. This latter feature is especially valuable because it allows details of the flow, which are otherwise invisible, to be observed and studied. Alternatively, a Graflex camera with a 4 x 5 Polaroid film holder is used in place of the microcomparator to photograph the full-aperture views of the flow fields. During hologram playback, the reconstructed light waves converge from the holograms to form a duplication of the true focus of the second parabolic reflector in the recording system permitting schlieren studies to be accomplished at leisure.

With the exception of one test for the 2-D compression ramp configuration, dual hologram interferometry was the primary optical process used. Interferograms of the flows were obtained by interfering light waves produced simultaneously from a test hologram and a reference state hologram; shadowgrams and schlieren results were obtained directly from the test holograms. A test hologram was a recording of a specific shock tunnel test, while a reference state hologram was a recording of a no-flow, model-out condition in the test section for either atmospheric or pump-down states. The test section of the shock tunnel was pumped to near vacuum levels for each test, and the pump-down reference state hologram was used to negate the effects of stress in the test section windows. The reference state holograms were the lead holograms in the dual plate alignment so that during the hologram playback step, the reconstructed reference waves were generated first and passed through the test hologram.

The models, instrumentation and test conditions were selected on the basis of the knowledge accumulated from a large number of studies over the past 15 years. The flow fields over the configurations selected are known to exhibit definitive features in the separation and reattachment regions as well as definitively formed separated

20

regions. Studies of the characteristics of incident shock-induced turbulent boundary layer separation were made at Mach numbers from 6 to 13 with the model shown in Figure 10. The strength of the interaction was controlled by the angle of the shock generator and was varied by changing the length of the flat plate. The flat plate was extensively instrumented with heat transfer and pressure gages along the centerline and also along selected spanwise rays. A shock generator angle of 15 degrees and a flat plate length of 38 inches ahead of the interaction provided a well-separated region and well-defined heat transfer and pressure distributions.

Studies of flow over the compression surface were conducted using the flat plate/wedge model (Figure 11). A wedge angle of 36 degrees was selected for the current measurements, again to obtain a well-separated flow. The large cone flare model was used for measurements over an axisymmetric configuration for which the transverse curvature effects are small. A 9-foot long, 6 degree half-angle cone with a 36 degree flare was used so that flow field surveys made through the boundary layer and separated region just ahead of the flare could be compared with the results in a complementary study.

2.3.4 Comparison to Flat Plate Theory

Interferograms were used to evaluate the accuracy of deducing density. Detailed fringe shift measurements were made for the turbulent boundary layer approximately 4 inches upstream of the corner interaction (Figure 12). These results were compared with simple prediction methods for hypersonic turbulent boundary layers over a flat plate with a sharp leading edge. To maintain the greatest accuracy, the measurements were made by directly viewing the holographically reconstructed image with an x-y microcomparator. These measurements were compared with predictions based on the Van Driest compressibility transformation of the Clauser/Cole incompressible velocity profiles and a modified Crocco relationship as shown in Figures 13 and 14.

2.3.5 Discussion of Qualitative Features

A typical single plate holographic interferogram was made by double-exposing a single plate, first with the reference beam just before the test, and then approximately 15 minutes later with the scene beam of the test. Here, the interferogram

SHOCK GENERATOR

FLAT PLATE

Figure 10   2-D SHOCK GENERATOR MODEL

MICROCOMPARATOR

HOLOGRAM
HOLDER

BEAM
EXPANDER

CW LASER

Figure 9   HOLOGRAPHIC PLAYBACK SYSTEM

Figure 11   2-D COMPRESSION-RAMP MODEL

22

Figure 12   FLOW STRUCTURE IN A TWO DIMENSIONAL CORNER FLOW (M=11 R_{e_L} = 30 x 10^6)
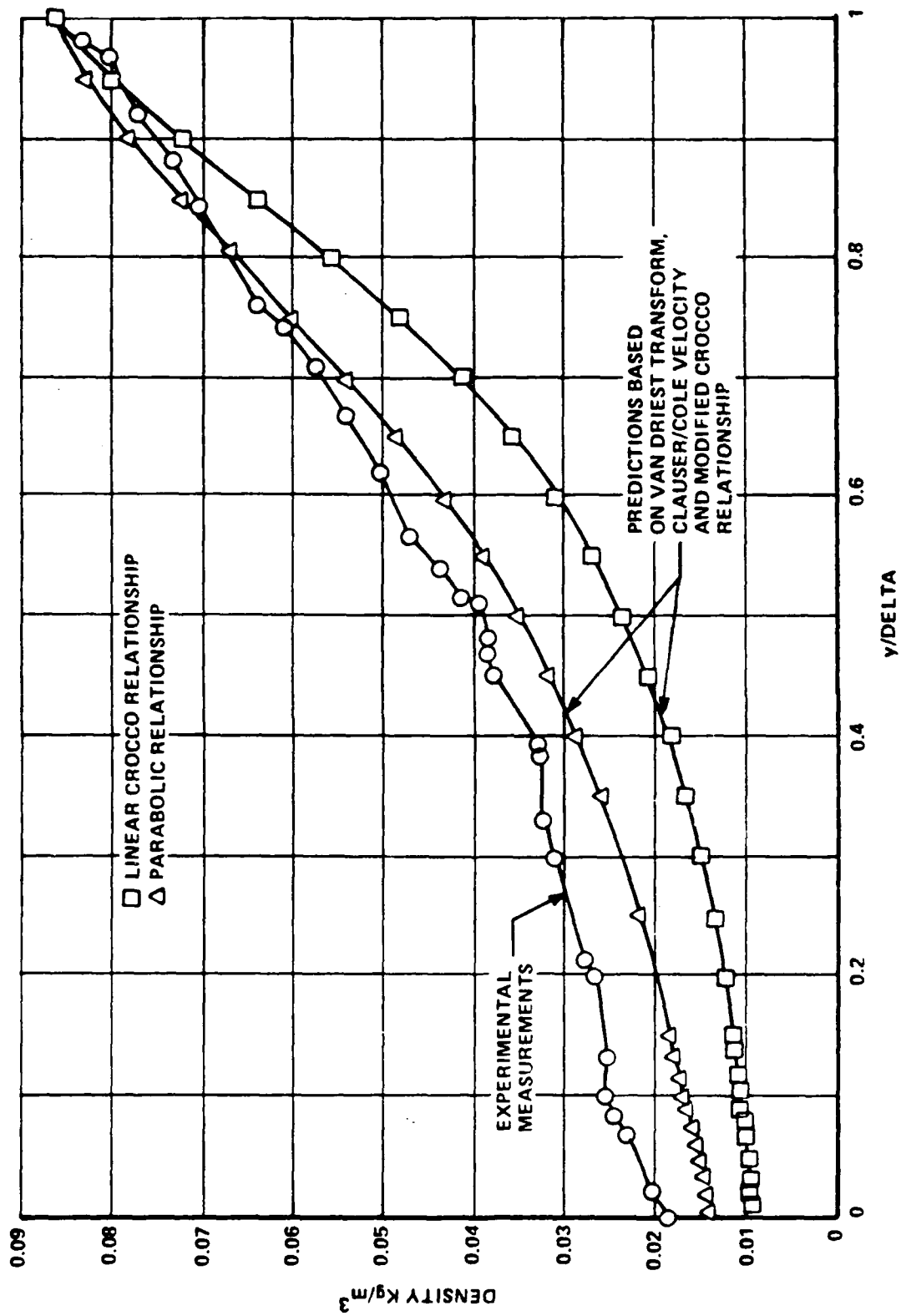
Figure 13   COMPARISON BETWEEN MEASUREMENTS OF THE DENSITY DISTRIBUTION ACROSS TURBULENT FLAT PLATE BOUNDARY LAYER AND SIMPLE PREDICTION
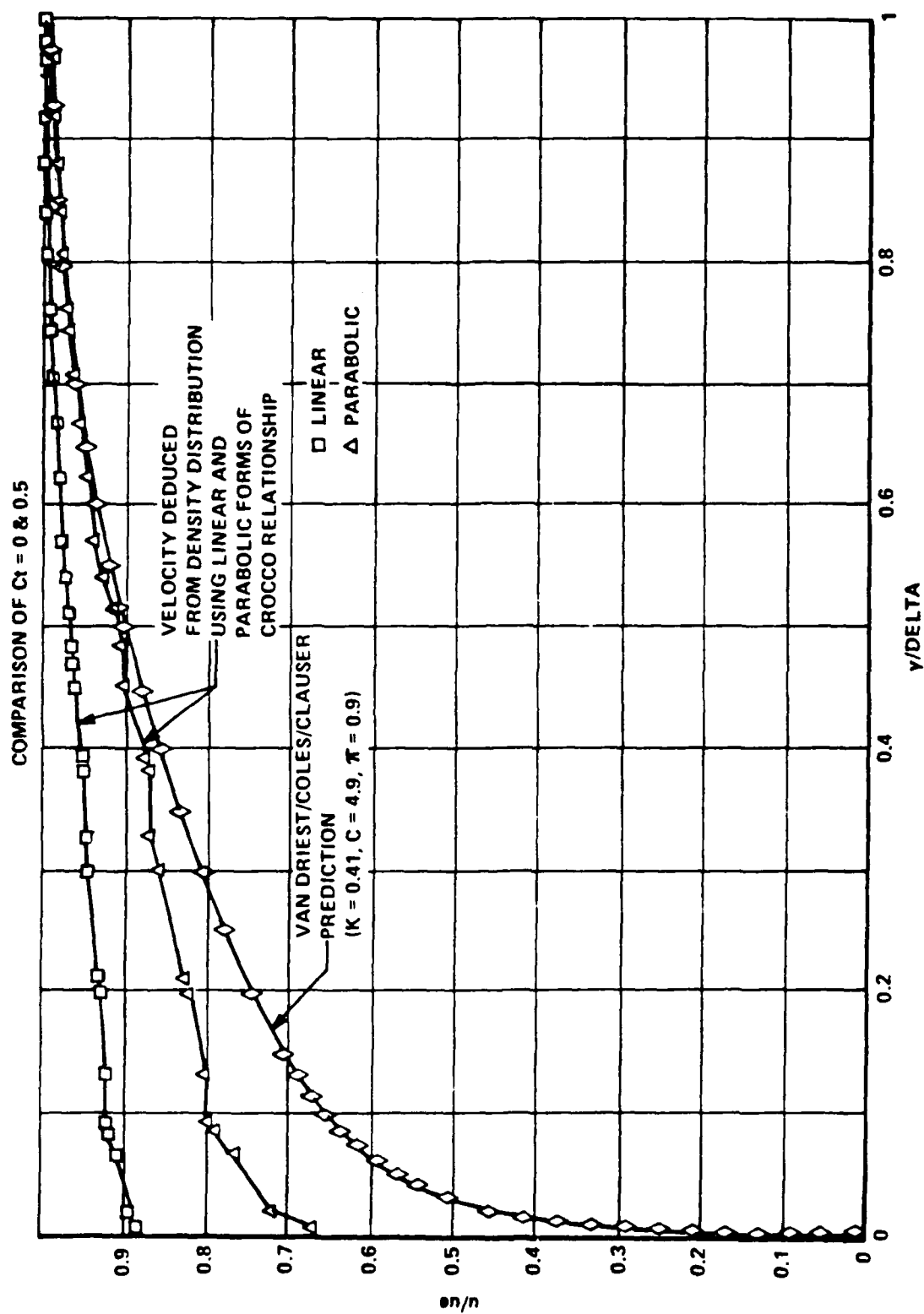
Figure 14 COMPARISON BETWEEN PREDICTED VELOCITY DISTRIBUTION AND VALUES DEDUCED FROM DENSITY MEASUREMENT

25

was fixed in the hologram. In this interferogram, the model wall appears as a solid black surface, while in the interferogram reconstructed using the dual plate technique, the model appears as a gray silhouette. The photographs show enlargements of 35 mm photographs of the reconstructed object waves as viewed through the eyepiece of a 20X telescope. Because this direct viewing approach was used, details in the hologram can be magnified to achieve pictures of greater clarity than would otherwise be obtained. Restating that all optical data shown result from the integrated effects of density changes from the beam splitter to the recording plane, these photographs must be interpreted with care especially in and close to regions of separated flow.

2.3.6   Turbulent Separation in a Two-Dimensional Compression Corner

Turbulent separation takes place in the sublayer where strong separation shock traverses the boundary resulting in strong normal pressure gradients. Such flows cannot be described by boundary layer theory and possibly not by the mass averaged Navier-Stokes equations. Holographic interferograms, schlieren photographs and shadowgraphs of separated flow over the flat plate/wedge are shown in Figures 15 and 16. The heat transfer and pressure distributions clearly indicate that the separation region occupies a fraction of a boundary layer thickness. The separation shocks that are created in this region are seen clearly in the shadowgraph and schlieren photographs, and they appear as rapid distortions of the fringe pattern in the interferogram. These shocks are highly distorted as they traverse the major part of the boundary layer. A matter of continuing debate is whether these distortions are responses to the unsteady movement of the separation point or to responses in the incoming turbulent flow. However, it is clear that significant pressure, temperature, and, hence, density fluctuations are generated by the inflections of the separation shock in this region. The multiple shocks that are typically observed in the separation region reflect the time-dependent position of separation (since they are also observed on axisymmetric models) and the three-dimensional nature of the flow at the edges of the model.

A prominent feature of the interferogram is a relatively uniform high temperature structure of the constant pressure recirculation region. The straight shear layer can be seen to be lifted above the recirculating flow, which appears to be constructed from a single vortex sheet with some smaller cells imbedded close to the reattachment region. This feature is significant from the viewpoint of the turbulence modeling of these flows. The rapid recompression that is always observed in

26

SEPARATION REGION

INTERFEROGRAM

FLOW DIRECTION →

REATTACHMENT REGION

GRID SIZE
38.1 x 38.1 mm

ENLARGEMENT

2-D FLAT PLATE	
COMPRESSION RAMP	36°
MACH NO.	11.34
REYNOLDS NO.	35.4×10^6
TEMPERATURE (T_o)	1555^oK
PRESSURES (P_o)	102.5 MPa
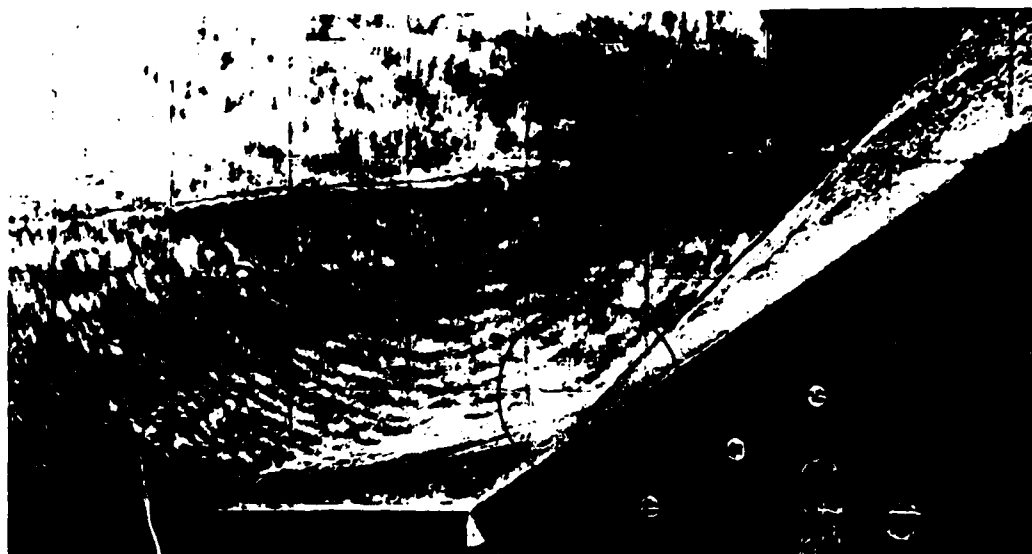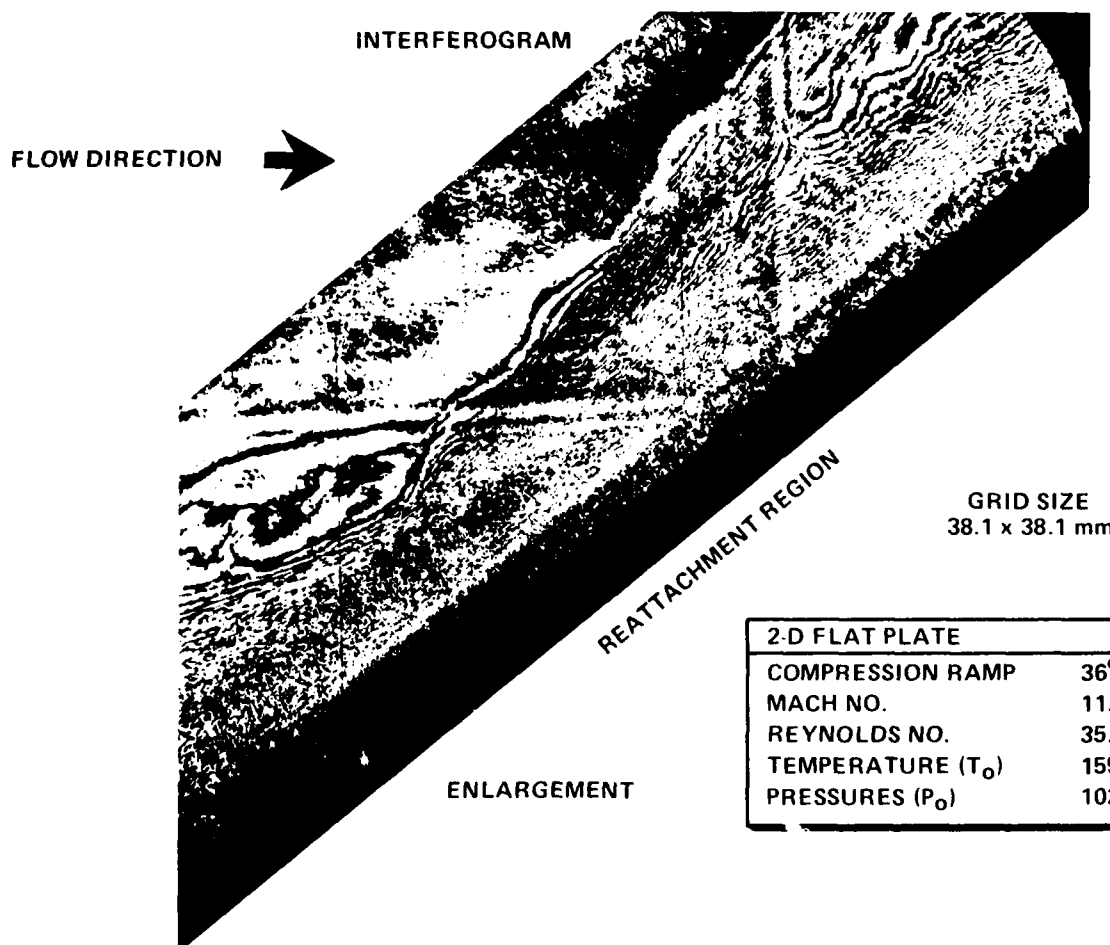
Figure 15   HOLOGRAPHIC INTERFEROGRAM OF COMPRESSION-RAMP INDUCED
BOUNDARY LAYER SEPARATION FOR 2-D FLAT PLATE IN HYPERSONIC
FLOW

SHADOWGRAM

FLOW DIRECTION →

REATTACHMENT REGION

GRID SIZE
38.1 x 38.1 mm

2-D FLAT PLATE	
COMPRESSION RAMP	36°
MACH NO.	11.34
REYNOLDS NO.	35.1×10^6
TEMPERATURE (T_o)	1563^oK
PRESSURE (P_o)	102.4 MPa

ENLARGEMENT
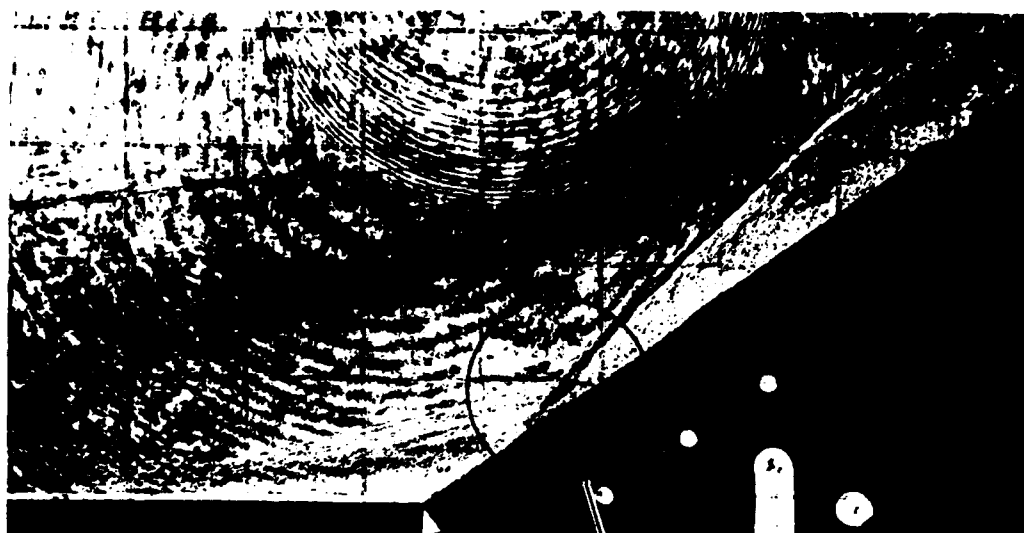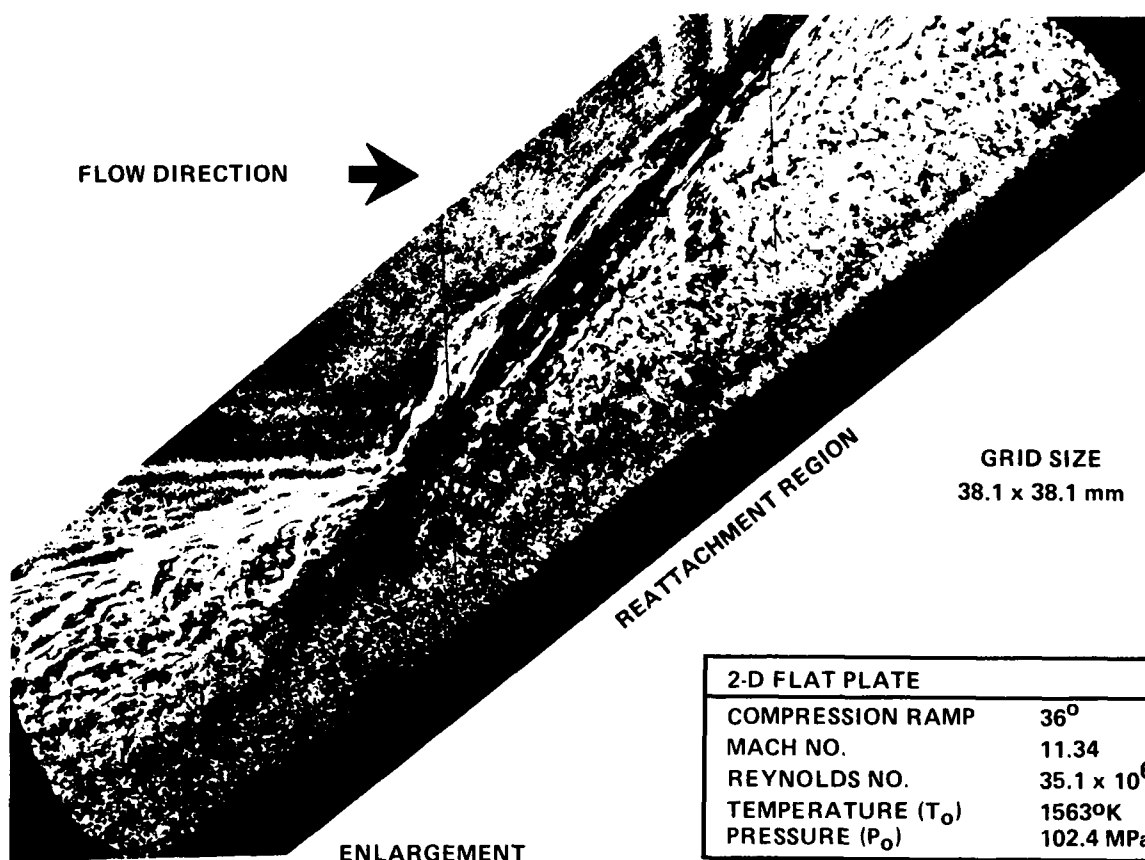
Figure 16   HOLOGRAPHIC SHADOWGRAMS OF COMPRESSION-RAMP-INDUCED
BOUNDARY LAYER SEPARATION FOR 2-D FLAT PLATE IN HYPERSONIC
FLOW (REFERENCE 2-22)

reattachment regions is accompanied by the formation of a reattachment shock. This shock relaxes to the wedge shock as the influence of the more efficient compression process close to the separated region disappears. Meaningful interpretation of the interferometer data obtained is difficult, if not impossible, because significant refraction effects are clearly observed in the interferogram. Schlieren photographs reveal an almost sinusoidal shock structure in the reattachment region, possibly reflecting a movement of the reattachment point. Such a movement indicates changes in the flow reversal in the separated region. This aspect of flow unsteadiness could significantly influence the size of the separated region, and clearly complicates a numerical description of this flow. The development of turbulence through the large pressure gradients in the reattachment region and the subsequent relaxation in the constant pressure region downstream of reattachment are important features of this flow. If refraction and edge effects can be eliminated from the fringe shift measurement, holographic interferometry will provide extremely valuable quantitative measurements of this separated flow field.

The reattachment region presents additional difficulties, because the strong flow curvature and rapid thinning of the boundary layer here may be generating three-dimensional flow structures (Goertler vortices) that clearly prevent a meaningful interpretation of these interferograms. Such three-dimensional effects also may be induced in the strong flow curvature close to the separation point. Basically, the unsteady and three-dimensional characteristics of these flows must be understood to develop accurate numerical descriptions of these flows, but an understanding of the unsteady and three-dimensional effects is also needed to help interpret the optical measurements. This point further suggests a need to study less complicated flows first (e.g., axisymmetric laminar cases previously mentioned).

2.3.7   Incident Shock Wave/Turbulent Boundary Layer Interaction

As in the flow over the flat plate/wedge compression corner, the size and flow structure in a region of incident shock impingement is controlled by the mutual interaction between the viscous and inviscid flow. However, the disturbances are generated outside the boundary layer, and the incident shock strength is modified by its interaction with the separation shock. The measurements of heat transfer and pressure on this configuration are shown in Figure 17, together with schlieren photographs made in earlier studies. The structure of the upstream disturbance generated by the

29
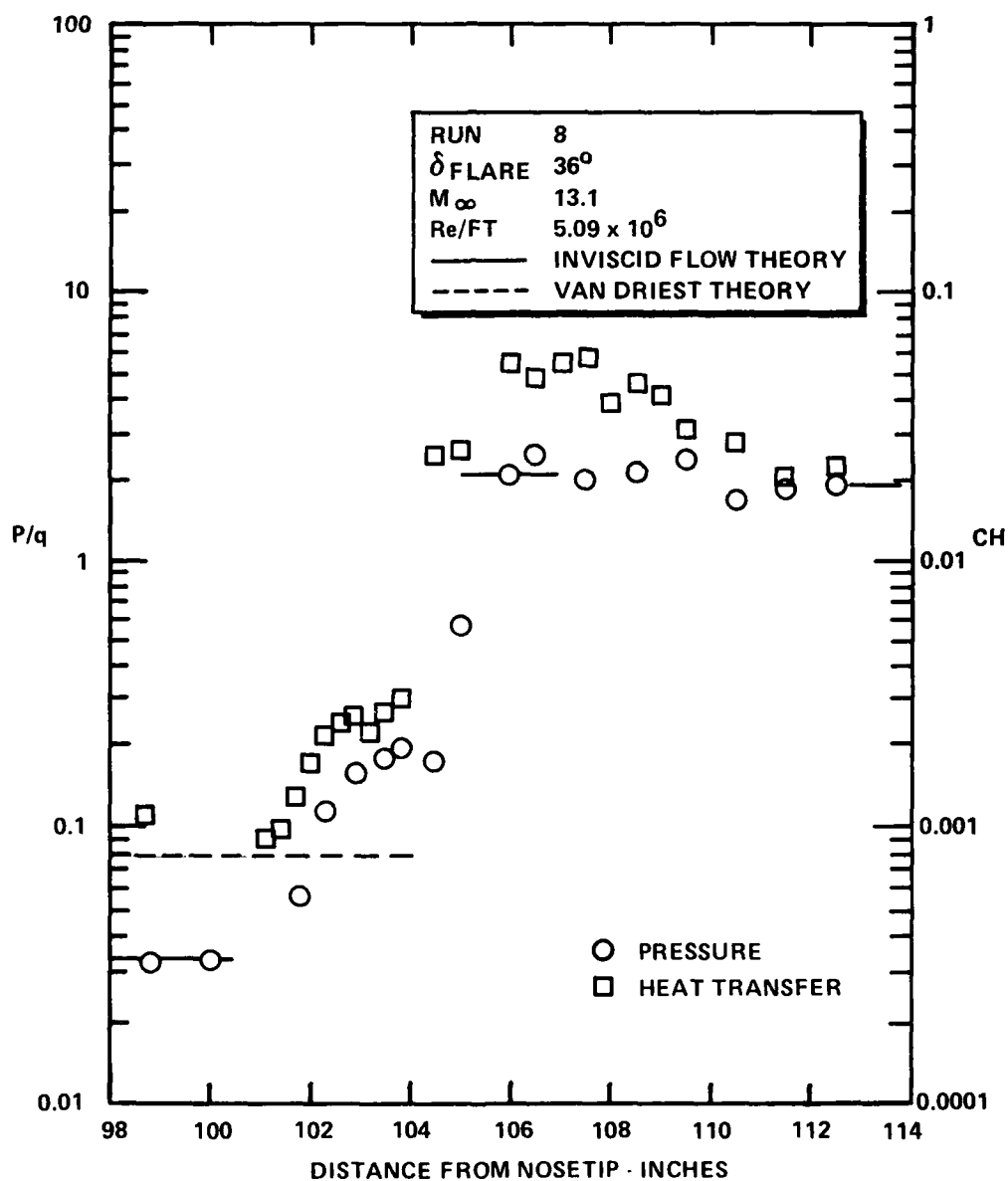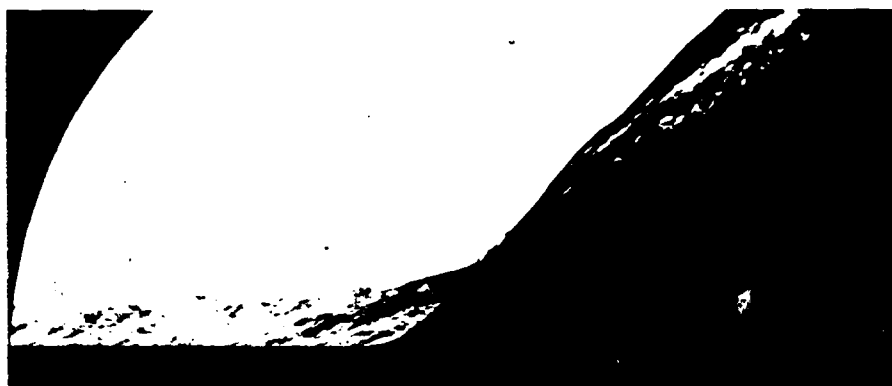
Figure 17 DISTRIBUTION OF PRESSURE AND HEAT TRANSFER IN SEPARATED FLOW OVER THE LARGE 6° CONE/36° FLARE CONFIGURATION

30

incident shock is very similar to that generated over the flat plate/wedge model. The basic viscous/inviscid interaction resulting in flow separation takes place at the base of the boundary layer. Separation shock(s) traverse through a major segment of the boundary layer, interact with the incident shock, and are then turned almost parallel to the plate surface; an expansion fan is generated as the incident shock interacts with the constant pressure free shear layer. The boundary layer flow is again turned parallel to the flat plate by the formation of the reattachment shock. Similar to the reattachment region developed on the compression ramps, the strong flow curvature would likely cause the formation of three-dimensional disturbances (Goertler vortices) in this region downstream of the incident shock. Again, the highly curved inflective shocks in the separation and reattachment regions are indicative of an unsteadiness which needs to be investigated with high frequency flow measurements to gain an understanding of these unsteady effects.

2.3.8 Separated Flows at the Cone/Flare Junction

Measurements of the distribution of heat transfer and pressure over this configuration made in previous studies are shown in Figure 17 along with a conventional schlieren photograph. The 36° flare angle generates a large separated region which extends 2 inches ahead of the cone-flare junction. As expected, the flow in the separated region is very similar to the corresponding regions on the compression ramp and incident shock configurations. However, interpretation of the phenomena causing the shock waves in the neighborhood of the constant pressure separated region is not understood. This multiplicity of shocks is also clearly discernible in the reattachment region of the flow, again leading to speculation on the intrinsic unsteady or three-dimensional character of the flow in this region. Even though the optical path lengths of these reattachment regions are significantly shorter than those of the two-dimensional models, strong refraction appears to distort these interferograms as well. Finding the best way to reduce the interferometer measurements of these axisymmetric separated regions remains an important task. However, resolving this problem may be easier and more productive than attempting to evaluate edge effects of the two-dimensional models.

2.3.9 Inteferometer Studies With Blowing and Roughness Model

During the blowing and roughness studies (discussed in detail in the following section) a significant effort was devoted to flow visualization and measurements with

31

holographic interferometry. Both infinite and semi-infinite fringe techniques were used, the first principally for flow visualization, and the second for quantitative flow field measurements. During the course of these studies, measurements were made for a range of compression angles and blowing rates for a rough surface configuration. Both nitrogen and nitrogen/helium mixtures were used as injectant, and clearly, only the interferograms made with the nittrogen can be the subject of quantitative interpretation.

A typical example of an infinite fringe for a small blowing rate and a compression surface angle of 25 degrees is shown in Figure 18. In this photograph, the shock layer and the boundary layer over the cone ahead of the expansion corner are well-defined as is the expansion of the boundary layer around this expansion corner. Boundary layer separation takes place halfway along the flat surfaces ahead of the compression ramp resulting in a well-defined separated region approximately three boundary layer thicknesses in length. The recirculation region is well-defined with holographic interferometry, and in this case there appears to be multiple bubbles. The separation shock, which is clearly visible when it emerges from the boundary layer, indicates by its changes in curvature that the separation region is unsteady, a feature also observed on smooth non-blowing surfaces. Shown for comparison in Figure 19 is the equivalent non-blowing configuration. Here there is little or no separation and the corner shock is relatively steady. Decreasing the flap angle, again with no blowing, results in a completely attached flow over the model as shown in Figure 20. Increasing the blowing to a level above that used for run 34 we see in Figure 21 that the separation is further extended until the separation for blowing rates of $B' = 3$ has moved forward to the cone/flat junction as shown in Figure 22. Finally for blowing rates boundary layer blow off occurs on the cone and the flow over the entire model is separated as shown in Figure 23. The finite fringe operating mode is the one from which the most accurate measurements of the distribution of density through the boundary layer and shock layer can be obtained. To obtain a quantitative determination of the density, the assumption must of course be made that the flow is either two dimensional or completely axisymmetric and the latter assumption is potentially true only on the conical section of the model. In Figure 24 we show a finite fringe hologram for a flow with very small blowing in which the cone boundary layer shows no visible evidence of injection at its base. The boundary layer appears to remain attached in the compression corner. Tripling the blowing rate results in a definitive change in the structure at the base of the boundary layer on the cone and the formation of a definitive separated region at the flat/compression surface junction, as shown in Figure 25. For

32
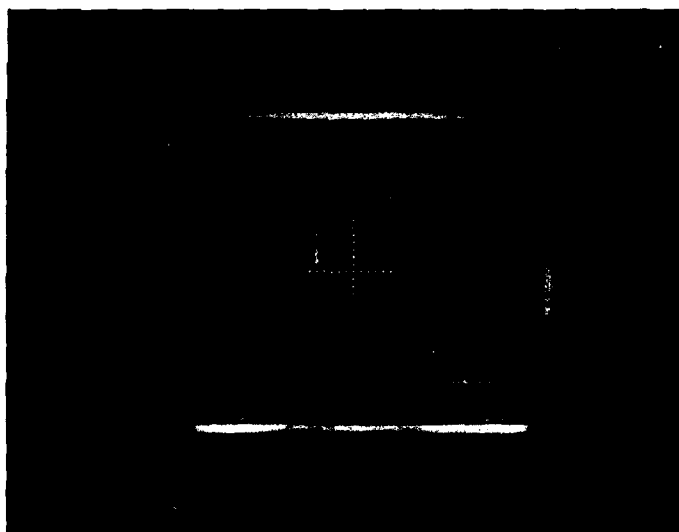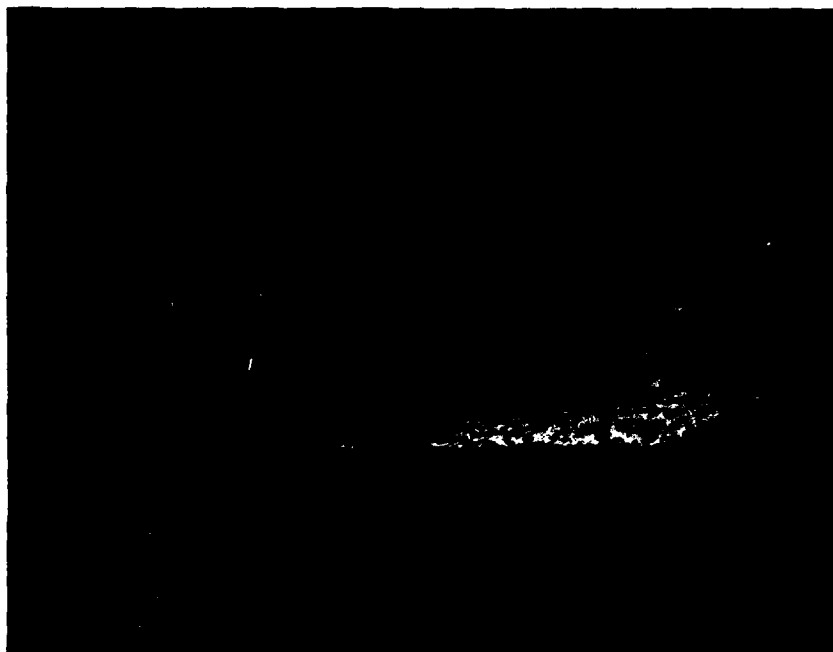
1 v/cm   5 nsec/cm

Run No. 34   Date: 17 February 1988

DRIVER PRESS:	28,000 psig	DRIVER GAS:	75% He in N_2
DRIVEN PRESS:	318 psia	DRIVEN GAS:	Air
BLOWING PRESS:	35 psig	BLOWING GAS:	N_2
FLAP ANGLE:	25°	ANGLE OF ATTACK:	0°

Figure 18

33
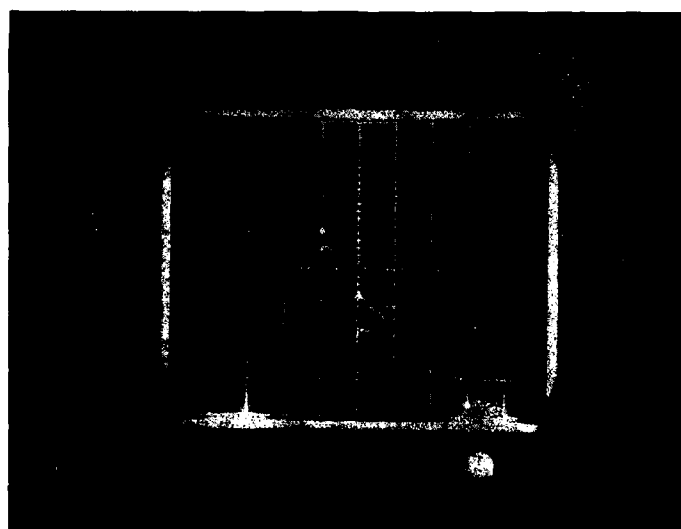
1 v/cm   5 nsec/cm

Run No. 31   Date: 16 February 1988

DRIVER PRESS:	12,000 psig	DRIVER GAS:	75% He in N_2
DRIVEN PRESS:	123 psia	DRIVEN GAS:	Air
BLOWING PRESS:		BLOWING GAS:	N_2
FLAP ANGLE:	25°	ANGLE OF ATTACK:	0°
FRINGE:	Infinite		
COMMENTS:	Blowing did not occur during this run.		

Figure 19

34
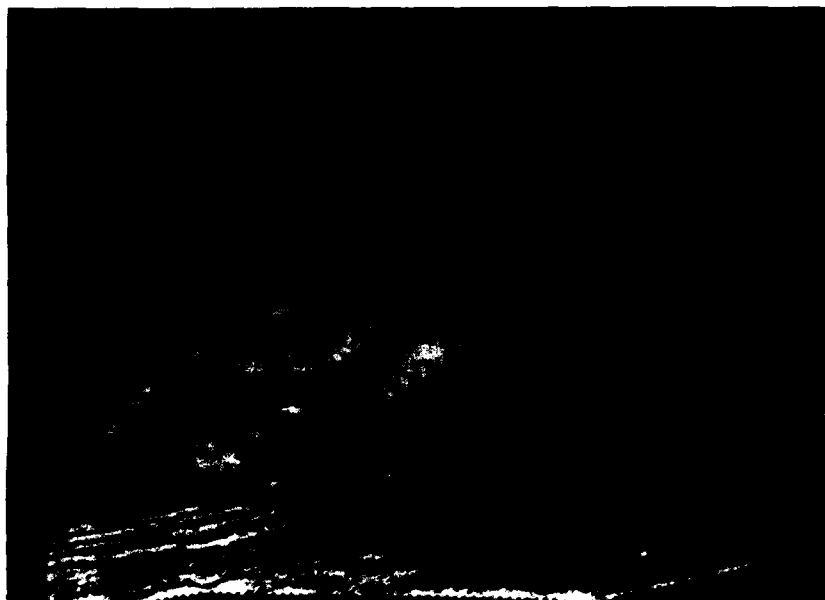
Run No. 2   Date: 22 January 1988

DRIVER PRESS:	28,000 psig	DRIVER GAS:	83% He in N$_2$
DRIVEN PRESS:	220 psia	DRIVEN GAS:	Air
BLOWING PRESS:	0	BLOWING GAS:	—
FLAP ANGLE:	15°	ANGLE OF ATTACK:	0°
FRINGE:	Infinite		
COMMENTS:			

Figure 20
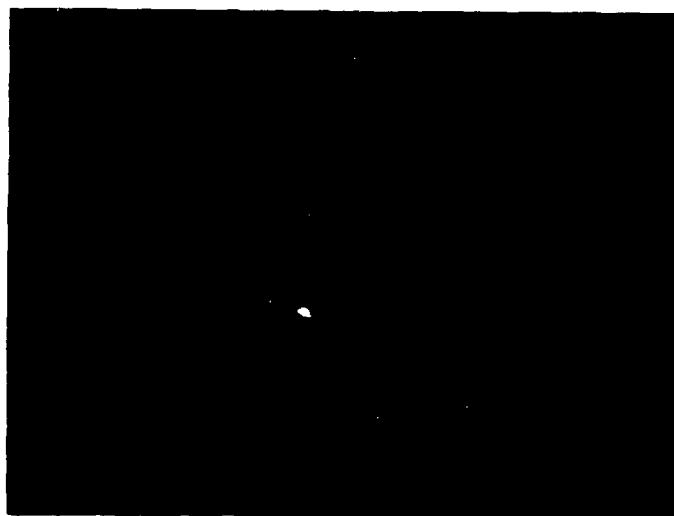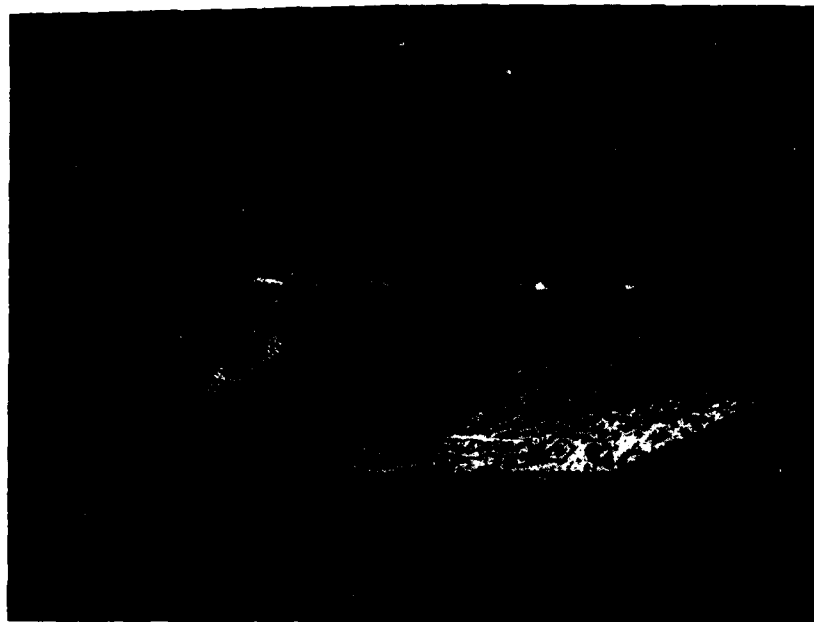
1 v/cm	5 nsec/cm

Run No. 33   Date: 17 February 1988

DRIVER PRESS:	28,000 psig	DRIVER GAS:	75% He in N_2
DRIVEN PRESS:	318 psia	DRIVEN GAS:	Air
BLOWING PRESS:	120 psig	BLOWING GAS:	N_2
FLAP ANGLE:	25°	ANGLE OF ATTACK:	0°
FRINGE:	Infinite		
COMMENTS:	Diode pulse was not present, so plate has multiple reference pulses. Scene beam is very light		

Figure 21

36
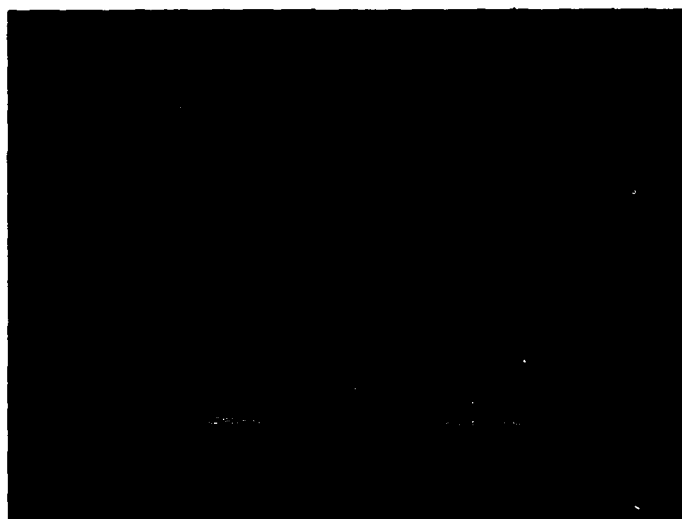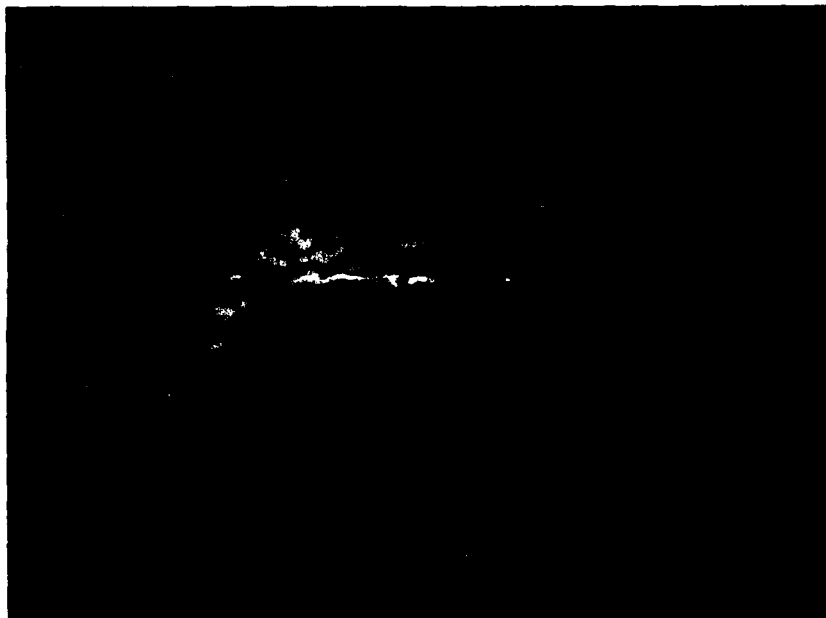
Run No. 32   Date: 17 February 1988

DRIVER PRESS:	28,000 psig	DRIVER GAS:	75% He in N_2
DRIVEN PRESS:	318 psia	DRIVEN GAS:	Air
BLOWING PRESS:	300 psig	BLOWING GAS:	N_2
FLAP ANGLE:	25°	ANGLE OF ATTACK:	0°
FRINGE:	Infinite		
COMMENTS:			

Figure 22
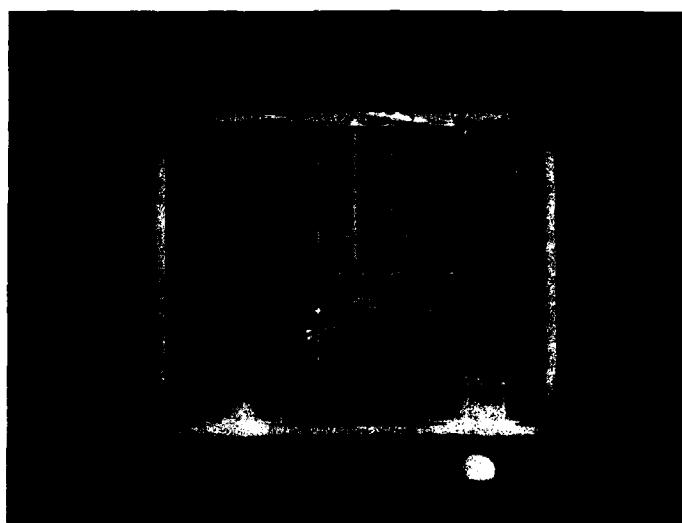
Run No. 35   Date: 17 February 1988

DRIVER PRESS:	28,000 psig	DRIVER GAS:	75% He in N_2
DRIVEN PRESS:	318 psia	DRIVEN GAS:	Air
BLOWING PRESS:	700 psig	BLOWING GAS:	N_2
FLAP ANGLE:	25°	ANGLE OF ATTACK:	0°
FRINGE:	Infinite		
COMMENTS:			

Figure 23
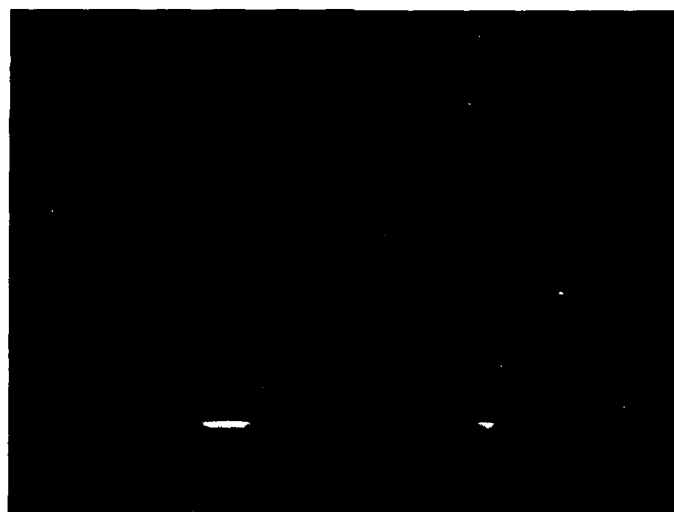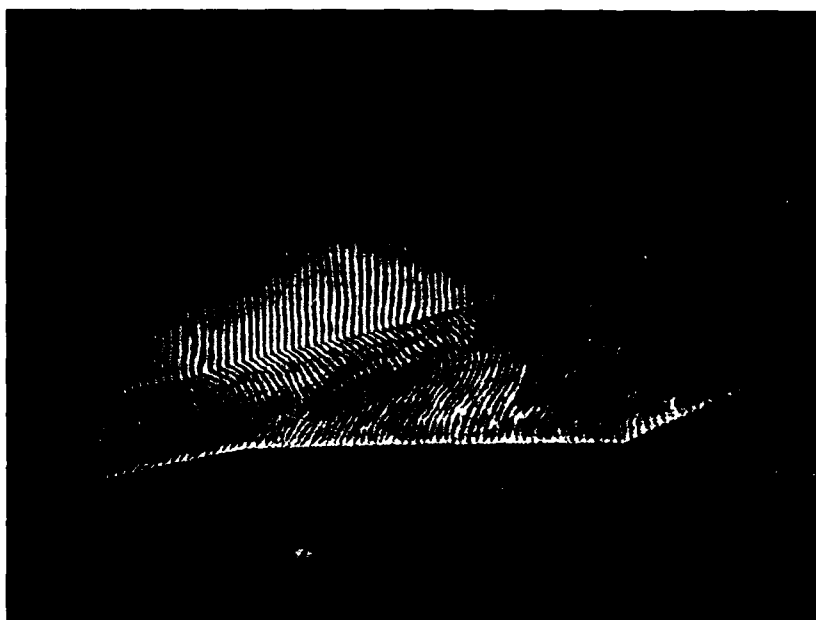
1 v/cm		5 nsec/cm	

Run No. 14   Date: 5 February 1988

DRIVER PRESS:	28,000 psig	DRIVER GAS:	83% He In N_2
DRIVEN PRESS:	220 psia	DRIVEN GAS:	Air
BLOWING PRESS:	10 psig	BLOWING GAS:	N_2
FLAP ANGLE:	25°	ANGLE OF ATTACK:	0°
FRINGE:	Finite, position 2		
COMMENTS:	One valcor valve fired during pressurization.		

Figure 24
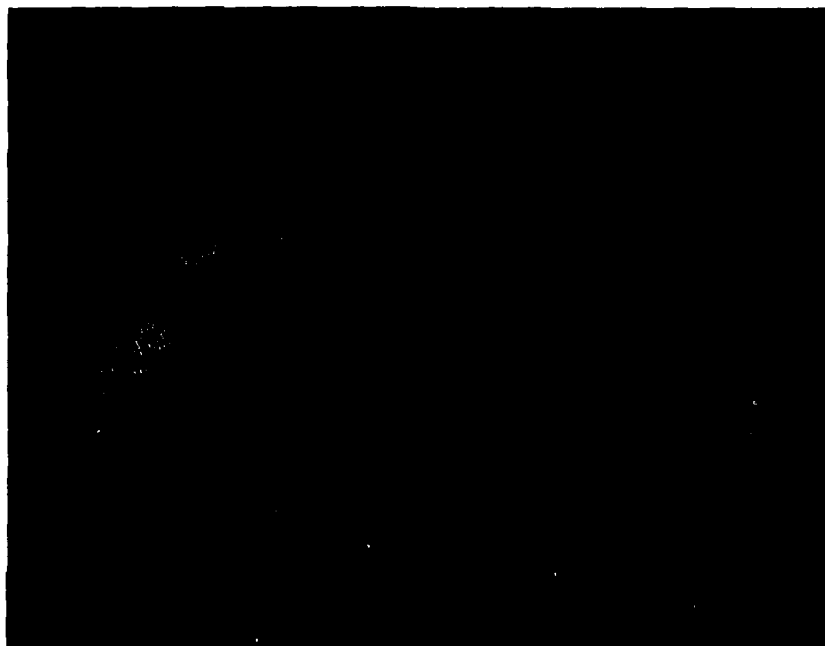
Run No. 29   Date: 16 February 1988

DRIVER PRESS:	12,000 psig	DRIVER GAS:	75% He in N_2
DRIVEN PRESS:	123 psia	DRIVEN GAS:	Air
BLOWING PRESS:	35 psig	BLOWING GAS:	N_2
FLAP ANGLE:	25°	ANGLE OF ATTACK:	0°
FRINGE:	Finite, position 2		
COMMENTS:	Sharp nose, cleaned M6 which was dirty. This provided a more uniform reference beam.		

Figure 25

large blowing rates, the stucture shock layer is completely distorted by blowing with the density increasing from the bow shock to the top of the shear layer before dropping rapidly to a relatively constant density region close to the wall (as shown in Figure 26). Here flow separation has moved forward to almost the cone/flat junction and a large portion of the flap is covered with a separated region. Increasing the blowing further begins to move the bow shock away from the body and the stucture of the complete shock layer is controlled by surface blowing as shown in Figures 27 and 28. Also shown in Figures 29 and 30 are the holograms with a helium/nitrogen mixture for the blowing gas at low and high injection rates respectively. While only qualitative results can be deduced from these photographs, it is clear that blowing with a gas of low molecular weight has a significantly greater effect on the structure of the flow over the cone and compression surface.
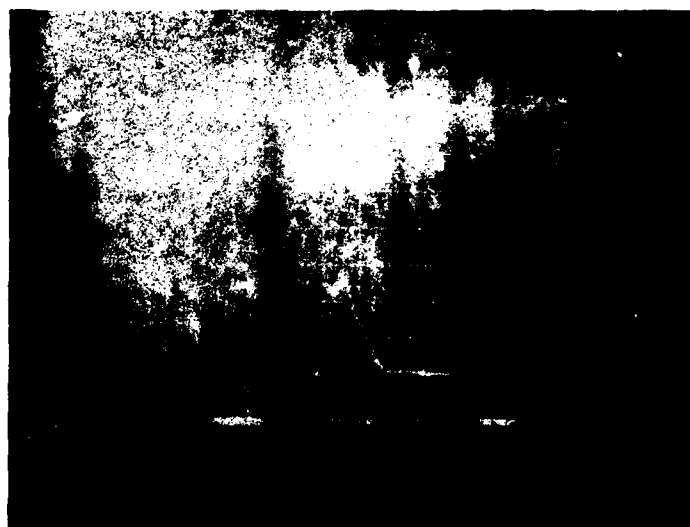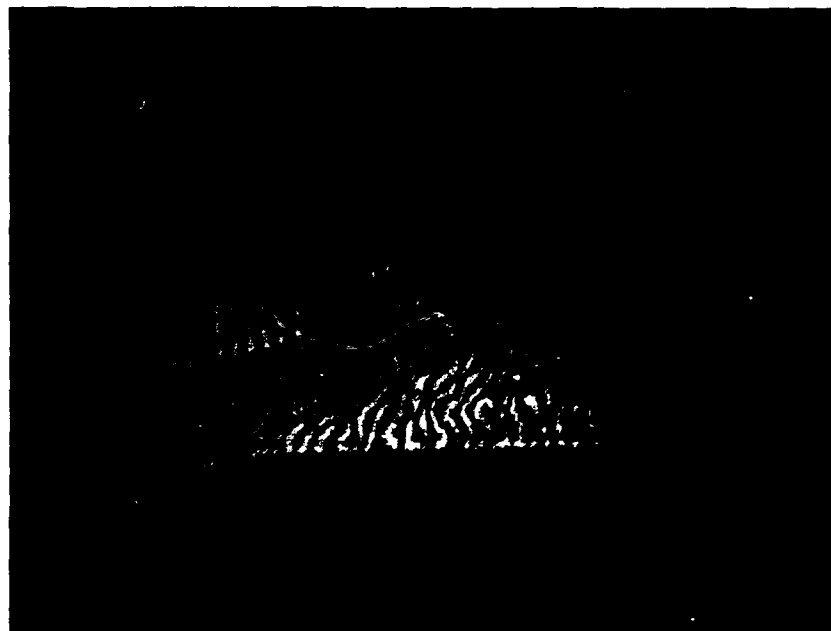
Run No. 10   Date: 3 February 1988

DRIVER PRESS:	28,000 psig	DRIVER GAS:	83% He in N_2
DRIVEN PRESS:	220 psia	DRIVEN GAS:	Air
BLOWING PRESS:	200 psig	BLOWING GAS:	N_2
FLAP ANGLE:	25°	ANGLE OF ATTACK:	0°
FRINGE:	Finite, position 3		
COMMENTS:			

Figure 26
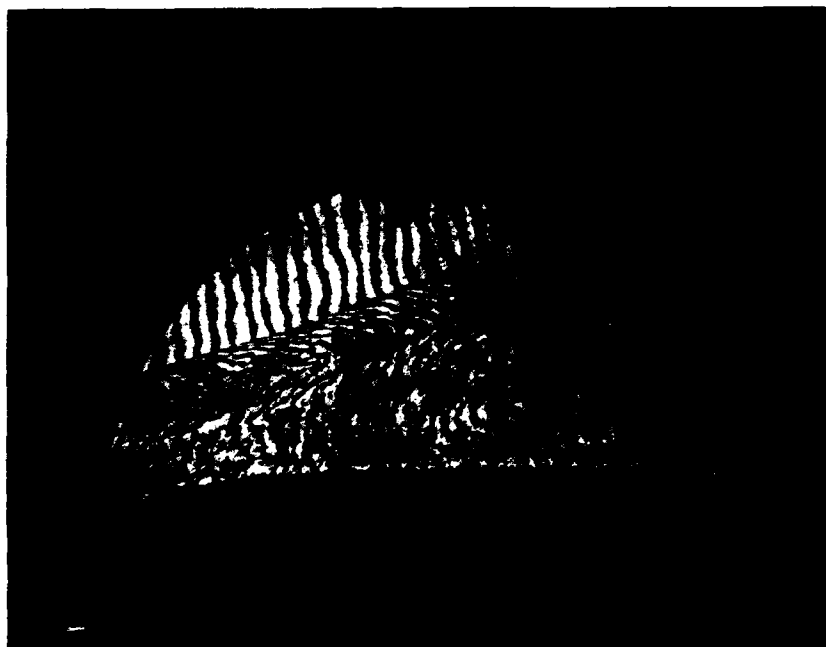
1 v/cm		5 nsec/cm	
Run No. 11		Date: 3 February 1988	
DRIVER PRESS:	28,000 psig	DRIVER GAS:	83% He in N_2
DRIVEN PRESS:	220 psia	DRIVEN GAS:	Air
BLOWING PRESS:	500 psig	BLOWING GAS:	N_2
FLAP ANGLE:	25°	ANGLE OF ATTACK:	0°
FRINGE:	Finite, position 3		
COMMENTS:			

Figure 27

43

1 v/cm   5 nsec/cm
Run No. 15   Date: 3 February 1988

DRIVER PRESS:	28,000 psig	DRIVER GAS:	83% He in N_2
DRIVEN PRESS:	220 psia	DRIVEN GAS:	Air
BLOWING PRESS:	350 psig	BLOWING GAS:	N_2
FLAP ANGLE:	25°	ANGLE OF ATTACK:	0°
FRINGE:	Finite, position 2		
COMMENTS:			

Figure 28

1 v/cm   5 nsec/cm
Run No. 17   Date: 2 February 1988

DRIVER PRESS:	28,000 psig	DRIVER GAS:	83% He in N_2
DRIVEN PRESS:	220 psia	DRIVEN GAS:	Air
BLOWING PRESS:	350 psig	BLOWING GAS:	62.5% He in N_2
FLAP ANGLE:	25°	ANGLE OF ATTACK:	0°
FRINGE:	Finite, position 2		
COMMENTS:	Control on fringe angle still poor, fringes at slight aft angle.		

Figure 29

1 v/cm   5 nsec/cm
Run No. 18   Date: 8 February 1988

DRIVER PRESS:	28,000 psig	DRIVER GAS:	83% He in N_2
DRIVEN PRESS:	220 psia	DRIVEN GAS:	Air
BLOWING PRESS:	250 psig	BLOWING GAS:	62.5% He in N_2
FLAP ANGLE:	25°	ANGLE OF ATTACK:	0°
FRINGE:	Finite, position 2		
COMMENTS:	Less total fringes than run 16 or 17, but fringes are vertical. Appears added pressure causes an additional vertical shift.		

Figure 30

Section 3

STUDIES OF THE EFFECTS OF COMBINED BLOWING AND ROUGHNESS ON THE AEROTHERMAL CHARACTERISTICS OF SLENDER CONICAL VEHICLES AND FLAP CONTROL SURFACES

3.1   BACKGROUND

Large surface ablation resulting from heat transfer rates generated on the windward ray of the heat shield close to the nosetip and on the control surfaces of MRVs flying at high angles of attack will be of critical concern to the designer of missiles that maneuver during re-entry. Unike conventional ballistic missiles, where the blowing from the heat shield is relatively small, the development of small MRVs with biconic frustum configuration, coupled with the requirements to fly at large angles of attack and use highly deflected control surfaces, has made an understanding of the aerothermodynamics of rough, highly ablating thermal protection and control systems of considerable importance. The deployment of highly ablating decoys has raised similar problems. To develop an accurate predictive capability to describe the ablation rates of the nosetip, heat shield, and control surfaces, it is necessary to understand and model the separate and combined effects of surface blowing and surface roughness. Our recent studies of roughness shape and spacing effects on ablating and non-ablating MRV configurations suggest not only that the subsonic studies are inapplicable to the heating of heat shields in hypersonic flow, but also that the basic modeling of the roughness drag and mechanisms of heating in the theoretical models is highly questionable.

The measurements made in earlier studies of transpiration cooling conducted at Calspan with transpiration cooled nosetips[1] were designed principally to determine whether blockage effects of mass injection are as large as predicted by the current codes. The measurements on the model with zero blowing, presented in Figure 32, clearly show that the intrinsic roughness of the surface causes heating enhancement factors of over 1.7. In fact, it can be seen by comparing Figures 31 and 32 that the heat transfer measurements on the conically rough hemisphere are in good agreement with those obtained on the non-blowing transpiration-cooled nosetip, with the exception of the region close to the stagnation point. In this region, the gages

47
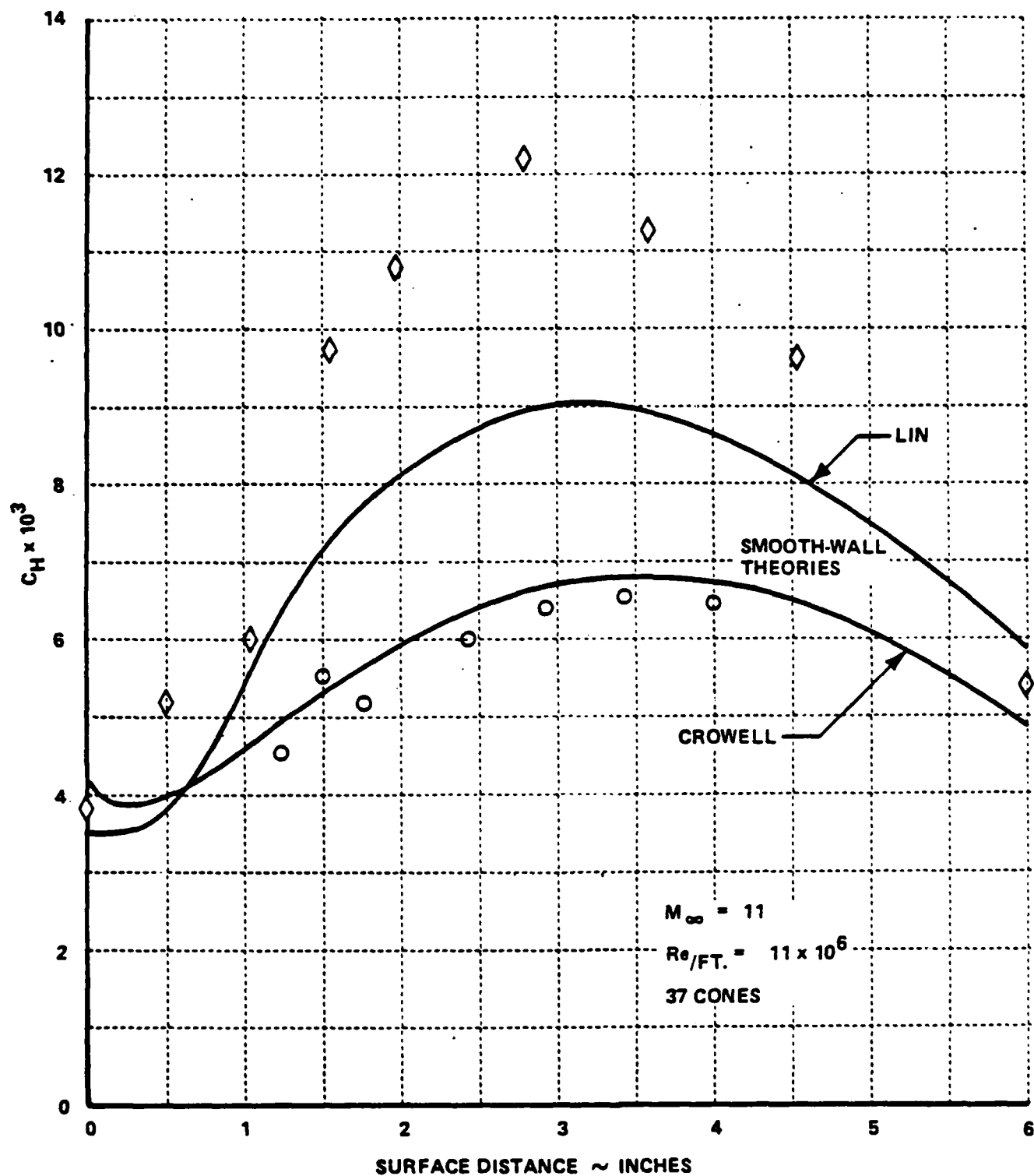
Figure 31 COMPARISON BETWEEN THE TURBULENT THEORIES OF LIN & CROWELL
FOR SMOOTH-WALL AND ROUGH-WALL MEASUREMENTS OF HOLDEN ON
12" DIAMETER HEMISPHERE (M = 11.2, Re_D = 11 x 10^6, K = 12.5)
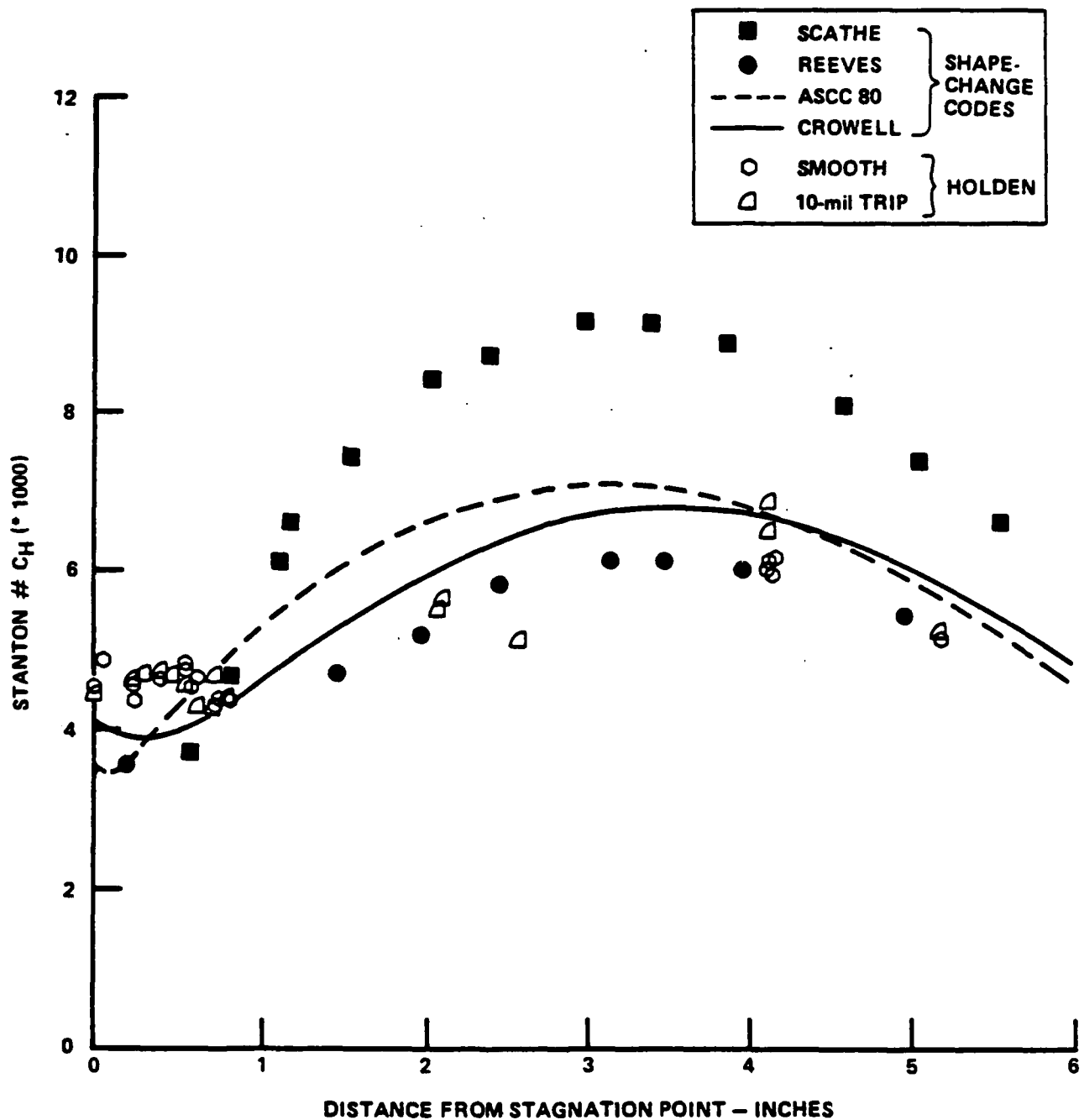
Figure 32   COMPARISON BETWEEN PREDICTING FROM FOUR OF THE SHAPE-CHANGE
CODES CURRENTLY IN USE AND SMOOTH-WALL HEAT TRANSFER
MEASUREMENTS ON HEMISPHERICAL NOSETIP

were mounted on the transpiration-cooled model such that they would be biased toward the larger heating level over the roughness. However, when a small amount of blowing $(\dot{m}/\rho U C_H = 0.032)$ was introduced, the heating rates over a major part of the transpiration-cooled model dropped to levels close to those recorded on the smooth model, as shown in Figures 32 and 34. It could be postulated on the basis of these measurements that the initial effect of mass addition from a rough ablating nosetip is to modify the flow around the roughness elements by eliminating the cavity flows in such a way that the momentum defect introduced by the roughness is small.

If the effect of mass addition is to remove surface roughness as an important characteristic parameter, a series of questions are posed for the correlation of flight measurements in terms of an effective surface roughness and the computational procedures in which the ablation rate is determined from heating levels enhanced by surface-roughness effects. Although experimental studies of the combined effects of mass addition and surface roughness are not easily constructed, the total lack of cold-wall measurements to validate the prediction methods in this area must be redressed.

The introduction of mass at the base of the boundary layer results in a reduction in momentum in the wall layer, which, like roughness, will make the boundary more susceptible to separation and ultimately result in a reduction in flap force, as shown in Figures 35 and 35a. However, injecting mass into the boundary layer will also severely distort the temperature and velocity distribution at the base of the boundary layer, which has the potential to cause a reduction in heat transfer and skin friction to the wall. Because momentum reduction on rough walls at the base of the boundary layer results principally from the form drag of the roughness elements, the introduction of mass at the rough wall could significantly change the basic mechanisms that control momentum and energy exchange. Our experience with transpiration-cooled nosetips[5] as well as those of Voisinet on wind tunnel walls, suggests that calculating the combined effects of mass addition and surface roughness (as is done in most prediction techniques) by using the product of the 'influence factors' (based on measurements of the separate effects of roughness and blowing) is invalid.

As demonstrated in studies by Holden[5] the entropy layer (a region of low momentum gas generated by the air processed by the highly curved section of the shock generated by a blunt nosetip) can cause a dramatic reduction in the forces generated by the control surfaces. While increasing the angle of attack can significantly
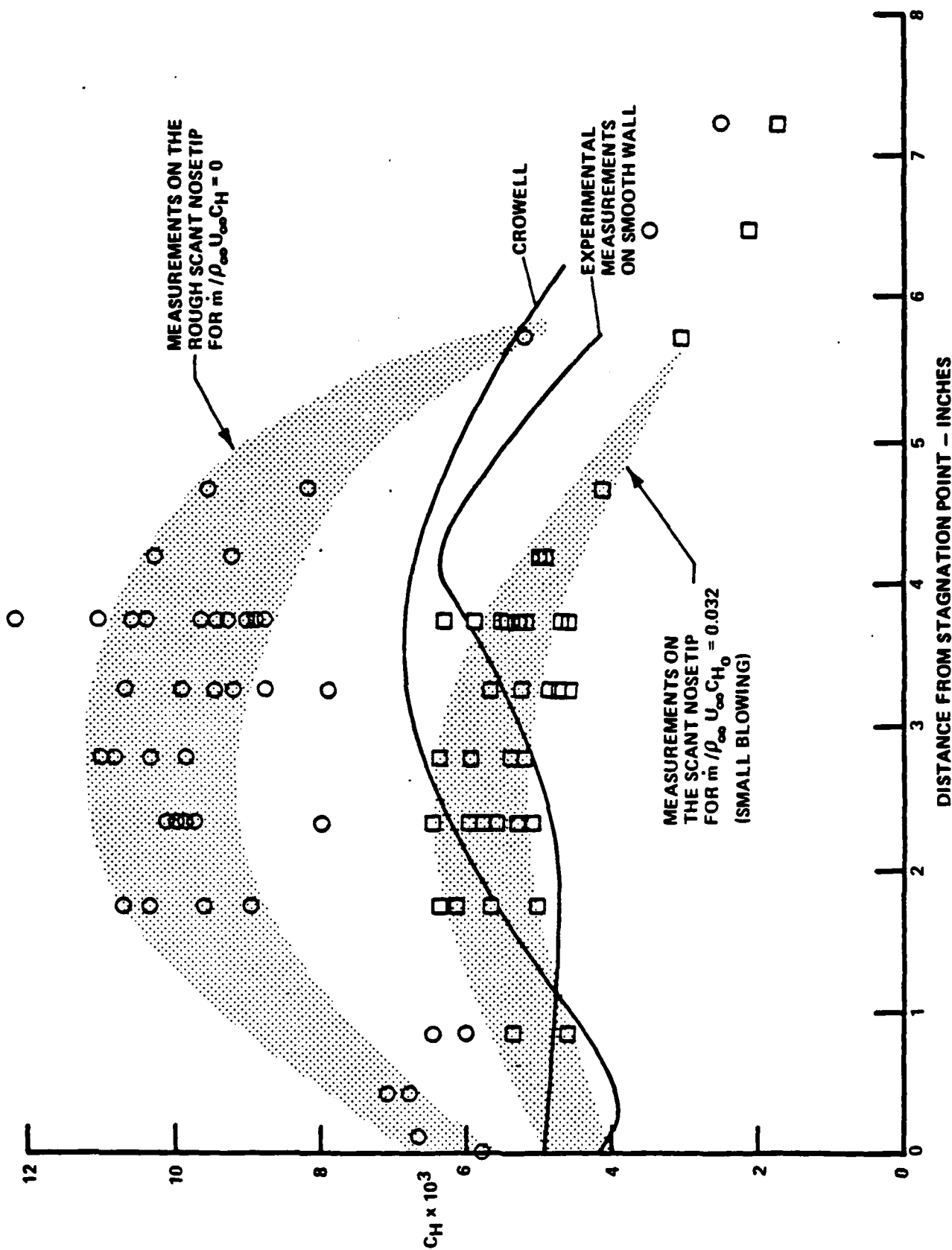
Figure 33 HEAT TRANSFER MEASUREMENTS ON SCANT AND SMOOTH HEMISPHERICAL NOSETIP SHOWING HOW SMALL BLOWING BRINGS DOWN HEATING LEVELS TO SMOOTH-WALL VALUES
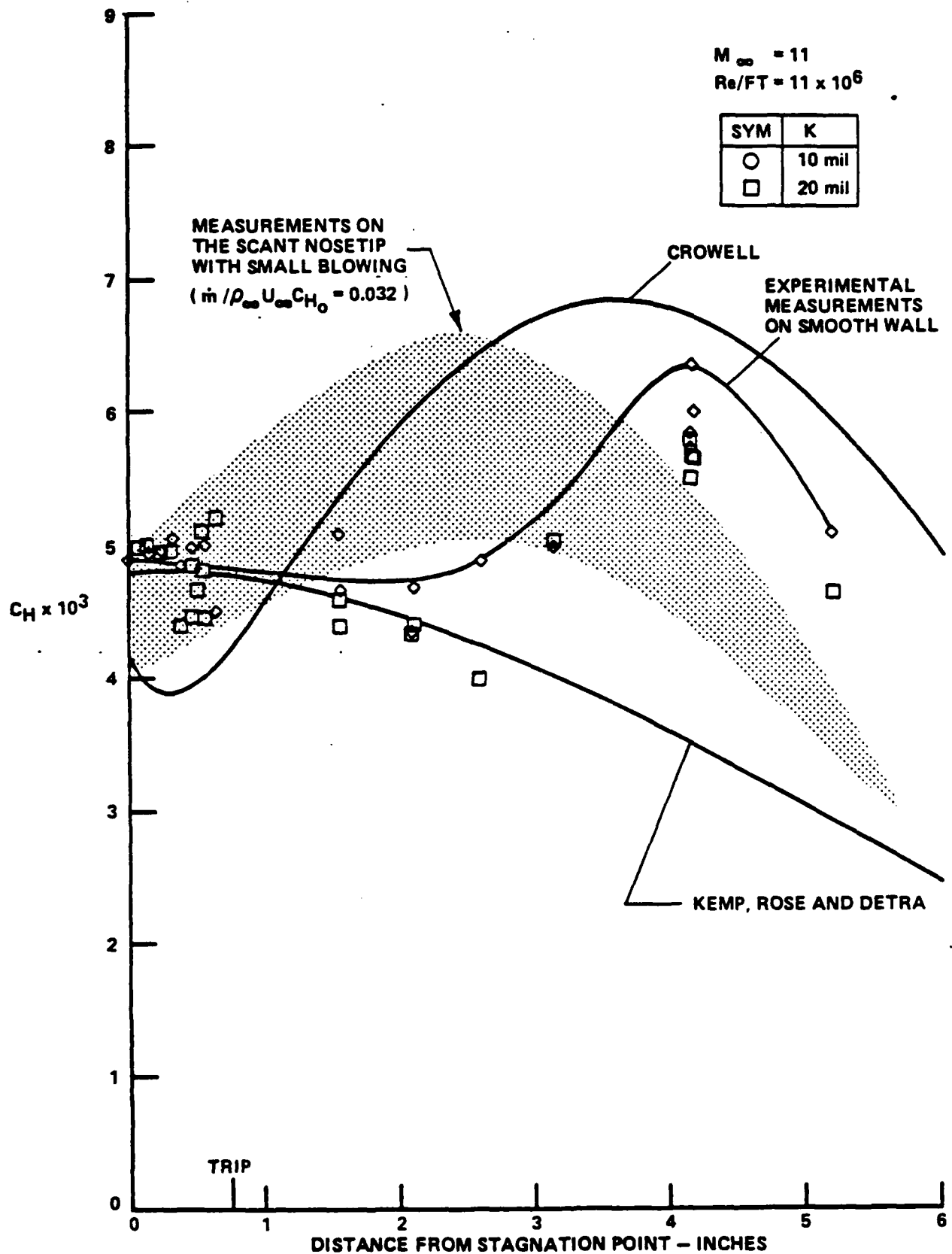
Figure 34 HEAT TRANSFER MEASUREMENTS INDICATING THAT SMALL BLOWING
ON ROUGH NOSETIP INITIALLY ACTS TO BRING DOWN HEATING LEVELS TO
SMOOTH-WALL VALUES

(a) UNSEPARATED

(b) SEPARATED

Figure 35   FLOW OVER THE ROUGH MRV CONFIGURATION WITH A 30° FLAP DEFLECTION

53

improve control-surface effectiveness in the windward plane by sweeping the entropy layer to the leeside of the vehicle, the effectiveness of a flare surface on the leeside of the vehicle can be significantly reduced.

To develop prediction schemes that will accurately describe the effects of combined roughness, blowing and entropy layer on the aerothermal performance of small MRVs and highly ablating decoys, we must conduct experimental studies under hypersonic, high-Reynolds-number, and cooled-wall conditions. The models used represent typical bluntness characteristics of the vehicles of interest and should be constructed with well-defined roughness and blowing characteristics. The correlations of the measurements from these studies should then be used to directly evaluate the accuracy of aerothermal models currently in use in "shape change" codes, while individual sets of measurements should be compared with more detailed calculations of combined roughness and blowing on sharp and blunt configurations.

3.2 REVIEW OF RELATED STUDIES

3.2.1 Studies of Surface Roughness Effects in Hypersonic Flows

Because most predictive techniques employ an effective sand-grain roughness as the single length scale characterizing roughness size, there continues to remain a key problem in relating the topography of a given surface to a sand-grain height. The experimental studies of Nikuradase[6] and Schlichting[7], both hydraulic pipe flow studies, were principally responsible for the selection of sand-grain roughness as the standard against which to measure relative effects of other types of roughness. Although this standard has been frequently employed, the topographical characteristics of a sand-grain surface have yet to be defined. In fact, because of the experimental difficulties involved in the preparation and inspection of rough surfaces inside a small-diameter pipe, it is surprising that Nikuradase's results are as consistent as reported. For fully developed pipe flows, Nikuradase established that the parameter controlling the similitude of the flows is the roughness Reynolds number ($U_\tau k/\nu_w$). This parameter ($\widetilde{Re}_k$) was selected in many subsequent studies to characterize boundary layer flows where other non-dimensional groupings (such as k_s/δ^*, k_s/θ, etc.) might have been considered more valid. The Schlichting studies, conducted with roughness of well-defined geometric shapes, provided the first set of measurements which could be reproduced in both experimental and theoretical studies. The results from these studies,

54

together with those from a number of subsequent investigations in subsonic adiabatic flows, were correlated by researchers to yield relationship between an "effective sand-grain height" and parameters which describe the geometric features of the surface--a step which further perpetuated the use of sand-grain roughness as a standard. The Dirling correlation, which is shown in Figure 36, is one such plot, from which an effective sand-grain roughness height can be determined from knowledge of peak-to-valley roughness height together with the shape and spacing of the roughness elements. While there is little direct supporting experimental evidence, the "lambda" form of the correlating curve is assumed to reflect a sudden change in flow structure from an "open" to a "closed" cavity flow around (between) the roughness elements as the spacing between the roughness elements is varied. Do open and closed cavity flows really exist on rough surfaces constructed from three-dimensional roughness elements? Is not the structure of the flow around the elements also dependent upon the local Reynolds number, a parameter not taken into account in any such correlations? If an effective roughness height can be accurately determined from a 'bump curve', this dimension must be combined with key fluid dynamic properties to yield a non-dimensional parameter or groups of parameters with which to characterize the flow. The roughness Reynolds number $\widetilde{R}_{e_K}\left(=\frac{U_\tau R}{\nu_w}\right)$ originally used by Nikuradase, and the non-dimensional roughness heights K/δ^*, K/θ_m and K/θ_t (where δ^*, θ_m, and θ_t are the displacement, momentum, and thermal energy thickness respectively), have all been used to correlate the aerothermal effects associated with boundary layers over rough re-entry vehicles. To date, however, no single parameter or combinations of parameters (e.g., $\widetilde{R}_{e_K}, \frac{K}{\theta_m}$) has been used with any great success to describe the general similitude of turbulent boundary layers in supersonic and hypersonic flows over rough, highly cooled walls.

The studies of Dvorak[8], Bettermann[9], Lewis[10], Simpson[11] and more recently Lin[12] and Finson[13] have provided further insight into the basic effects of roughness shape and spacing on the characteristics of the rough wall boundary layer and skin friction and heating to a rough surface. Dvorak combined the effects of roughness shape and spacing into a single parameter λ (the roughness density), defined as shown in Figure 37. He linked the downward shift in the velocity profile $\Delta U / U_\tau$ to a combination of roughness Reynolds number $Re_K\left(= U_\tau K/\nu_w\right)$ and λ through the relationship

$$\frac{U}{U_\tau} = \frac{1}{K} \ln\left(\frac{\varphi U \tau}{\gamma}\right) + A - \frac{\Delta U}{U_\tau}\left(\frac{K U \tau}{\gamma}, \lambda\right) \qquad \cdots 1$$

54a

In incompressible flows the smooth regime, where the surface shear is entirely due to viscous shear is defined by $\tilde{R}_{ek} <$ 5. At larger $\tilde{R}_{ek}$'s $\simeq 50$), the surface shear is composed of form drag on the roughness elements combined with viscous shear. For $\tilde{R}_{ek} > 70$, the surface shear results principally from drag, and viscosity is no longer a factor in controlling the velocity profile. For fully rough flows, Equation 1 can be rewritten

$$\frac{U}{U_{\tau}} = \frac{1}{\mathcal{K}} \ln \left(\frac{y}{K} \right) + A - \left[\frac{\Delta U}{U_{\tau}} - \frac{1}{\mathcal{K}} \ln \left(\frac{U_{\tau} K}{\nu} \right) \right] \qquad \ldots 2$$

where

$$\frac{\Delta U}{U_{\tau}} - \frac{1}{\mathcal{K}} \ln \left(\frac{K U_{\tau}}{\nu} \right) = f(\lambda)$$

which is a function of the roughness density. Here it should be noted that $f(\lambda) = A - U_R^*$ where U_R^* is the velocity close to the top of the roughness elements and $A(= 5)$ is the smooth wall constant. Now the definition Nikuradse's of sand-grain roughness is basically

$$\frac{U}{U_{\tau}} = \frac{1}{\mathcal{K}} \ln \left(\frac{y}{K_s} \right) + 8.5 \qquad \ldots 3$$

Hence, combining equations 2 and 3 we obtain

$$f(\lambda) = - \left[3 + \frac{1}{\mathcal{K}} \ln \left(\frac{K}{K_s} \right) \right]$$

Betterman and Dvorak suggest that the subsonic measurements should be correlated by two relationships:

For $1 < \lambda < 4.68$, $f(\lambda) = 17.35 (1.625 \log_{10} \lambda - 1)$

And for $\lambda > 4.68$, $f(\lambda) = -5.95 (1.103 \log_{10} \lambda - 1)$

The existence of two regions has been rationalized on physical grounds, supported by experimental studies in two-dimensional flows. There is serious debate about whether a significant change in flow structure occurs as three-dimensional roughness elements are drawn together. Certainly the measurements with stone roughness do not exhibit such a trend. This is particularly unfortunate, since Nikuradse's data falls on the line constructed principally from data obtained on roughness constructed by two-dimensional machined grooves.

Finson's engineering model based on the early concepts of Liepmann and Goddard[14] and his (Finson's) detailed numerical calculations provides a good basis for

interpreting the physical phenomena of key importance in rough wall heating, as well as a relatively simple prediction technique. The shear on a rough wall can be expressed as the sum of the viscous and form drag of the rough surface:

$$c_f = c_{f_{base}} + \int_B^T \frac{\rho u^2}{\rho_e u_e^2} \cdot c_D \cdot B(y) \cdot \frac{d^2 y}{D^2} \, dy$$

where $B(y)$ is the blockage factor, and $d(y)$ and D are the diameter of the roughness element and the spacing between elements, respectively. From his detailed numerical solutions, Finson showed that ρ and u were relatively constant between the base and top of the roughness element at values ρ_R, u_R close to the top of the roughness. Equation (7) becomes

$$c_f = c_{f_{base}} + \frac{\rho_R u_R^2}{\rho_e u_e^2} \cdot c_D \cdot B\left(\frac{K}{2}\right) \frac{A_p}{A_s}$$

where A_p/A_s is the ratio of projected area of the roughness element in the direction of the flow to total area of the flow on which they stand, and $B\left(\frac{K}{2}\right)$ is the average value of $B(y)$.

For compressible flows Finson found that

$$U_R / U_e = 0.247 + .234 \log\left(\frac{\rho_R}{\rho_e} \frac{A_s}{A_p}\right)$$

where

$$\frac{\rho_R}{\rho_e} = \left[\frac{T_w}{T_e} + \left(1 + \frac{\gamma-1}{2} M_e^2 - \frac{T_w}{T_e}\right) \cdot \left(\frac{U_R}{U_e}\right) - \left(\frac{\gamma-1}{2}\right) M_e^2 \frac{U_R^2}{U_e^2}\right] \quad \cdots \cdots$$

Therefore, assuming c_{f_D} is the smooth wall heating level, it is possible to relate the rough wall skin friction to the smooth wall value in the generalized form

$$\frac{c_{f_{ROUGH}}}{c_{f_{SMOOTH}}} = 1 + f_1\left(M_e, \frac{T_w}{T_e}, \frac{K}{\theta}\right) \cdot f_2\left(\lambda, B, \left(\frac{K}{D}\right), c_D\right)$$

The relationship for heat transfer is assumed of the same form

$$\frac{c_{H_{ROUGH}}}{c_{H_{SMOOTH}}} = f_1'\left(M_e, \frac{T_w}{T_e}, \frac{K}{\theta}\right) \cdot f_2'\left(\lambda, B, \frac{K}{D}, c_D\right)$$

If we assume that the product of the blockage factor and ___ are invariant with rough shape and space, then for constant local free stream condition, we get the Dvorak-Simpson Parameter:

$$\frac{C_H \, ROUGH}{C_H \, SMOOTH} = f\left(\frac{A_p}{A_s}\right)$$

A slightly different form can be obtained by the subsonic blunt body approximation

$$C_D = C_{D \, REF}\left(A_p / A_{ws}\right)$$

and using D/K rather than A_s/A_p to obtain the correleation in terms of the Dirling[15] parameter,

$$\frac{C_H \, ROUGH}{C_H \, SMOOTH} = f\left(\frac{D}{K} \cdot \left(\frac{A_{ws}}{A_p}\right)^{4/3}\right)$$

where the various areas are illustrated in Figure 36.

It should be noted that for fully rough walls

$$C_f \doteq \frac{\rho_\omega \, u^{*^2}}{1/2 \, \rho_e \, u_e^2} = \frac{\rho_R \, U_R^2}{\rho_e \, U_e^2} \cdot C_D \cdot B\left(\frac{K}{2}\right) \cdot \frac{A_p}{A_s}$$

or

$$\frac{U_R}{U^*} = u_R^* = \sqrt{\frac{2}{C_D B\left(\frac{K}{2}\right)} \cdot \frac{A_s}{A_p} \cdot \frac{\rho_\omega}{\rho_R}}$$

therefore from equation 2, for incompressible flows putting A = 5, and

we obtain
$$f(\lambda) \doteq 5 - \sqrt{\frac{2}{C_D B\left(\frac{K}{2}\right)} \lambda}$$

or for
$$C_D \cdot B\left(\frac{K}{2}\right) = 1$$
$$f(\lambda) \doteq 5 - \sqrt{2\lambda}$$

which, as shown in Figure 37 is in relatively good agreement with the incompressible data for flow 'without cavities'.

ROUGHNESS ELEMENT DRAG

$$\tfrac{1}{2}\rho_R u_R^2\, C_{D_R} \times B$$

DRAG COEF. INDIVIDUAL ELEMENT

BLOCKAGE COEFF.

SIMPSON SHAPE PARAMETER $\dfrac{A_p}{A_s}$

DIRLING SHAPE PARAMETER $\dfrac{D}{K}\left(\dfrac{A_{ws}}{A_p}\right)^{4/3}$

SMOOTH WALL DRAG $\Sigma \Delta D_s$

$$\Delta D_s = \tfrac{1}{2}\rho_e u_e^2\, C_{F_s} A_s$$

$$\Delta D_T = \Delta D_s + \Delta D_R$$

FORM DRAG OF ROUGHNESS ELEMENT ΔD_R

$$\Delta D_R = \tfrac{1}{2}\rho_R u_R^2 \cdot C_{D_R} A_p \cdot B$$

$$\Sigma \Delta D_T = \tfrac{1}{2}\rho_e u_e^2\, C_{F_R} \Sigma A_s$$
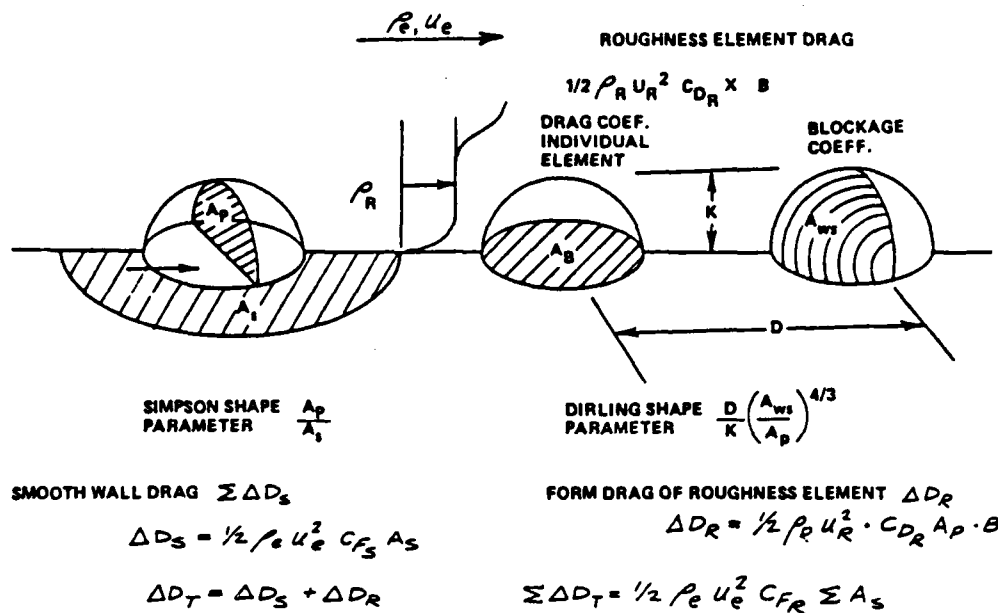
$$\frac{C_{F_R}}{C_{F_S}} = 1 + \frac{1}{C_{F_S}} \cdot \frac{\rho_R u_R^2}{\rho_e u_e^2} \cdot B \cdot C_{D_R} \cdot \left(\frac{A_s}{A_p}\right)^{-1}$$

Figure 36   SIMPLIFIED DRAG MODEL FOR ROUGH-WALL SKIN FRICTION

SCHLICHTING 3-D ELEMENTS

- ○ HEMISPHERES
- ◇ SPH. SEGMENTS
- △ CONES
- □ RIGHT ANGLES

2-D SQUARE ROD ELEMENTS

- ■ BETTERMAN
- ◓ LIU (ET AL.)

NIKURADSE SAND

CLOSED CAVITY

OPEN CAVITY

k_s/k

$\lambda = D/K\,(A_{ws}/A_p)^{4/3}$

Figure 37   "EFFECTIVE" ROUGHNESS CORRELATIONS FOR DIFFERING ROUGHNESS GEOMETRIES AND SPACINGS

56

In recent studies of effects of roughness shape and spacing on the heat transfer and skin friction to the roughness, nosetips, frusta and flaps of a typical MRV configuration, Holden used both the Dvorak/Simpson parameter A_S/A_p and the Dirling parameter $\frac{D}{K}\left(\frac{A_p}{A_{W_S}}\right)^{4/3}$, and achieved reasonable success in correlations. In these studies, the effects of roughness shape and spacing on the heat transfer and skin friction both for surfaces with sand-grain roughness and those constructed with geometrically well-defined hemispherical and conical roughness elements were examined. Also, heat transfer, skin-friction, and pressure-distribution measurements were obtained on spherical and ablated noseshapes, conical frusta, and the control surfaces of MRV model in hypersonic flow. The results of this work have demonstrated that the low-speed measurements of Nikuradse[16], Schlichting[17], and others, and the correlations of Dirling[18]/Simpson[19], cannot be used directly to predict rough-wall heating and skin friction in supersonic and hypersonic flows over non-adiabatic surfaces. Even the more solidly founded prediction scheme developed by Finson[20], which is based upon his detailed numerical solutions, consistently overpredicts the roughness-enhanced heating levels in high-speed flows. While direct measurements of the skin friction of, and heat transfer to, geometrically well-defined rough surfaces provide the opportunity to more closely evaluate the accuracy of the current shape-chang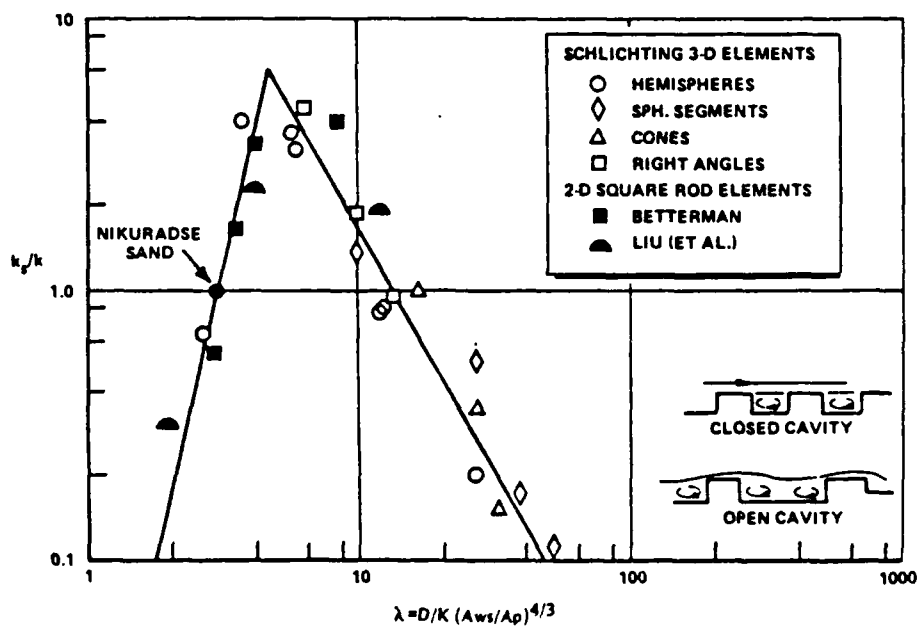e codes and the more fundamental treatments like that of Finson in high Mach number, high Reynolds number flows, there remains a basic need to define more closely the fundamentals of the fluid dynamics which control momentum and energy exchange in high-speed flows over adiabatic and non-adiabatic surfaces.

3.2.2 Combined Blowing and Surface Roughness Effects in High-Speed Flows

The models used in the current codes to describe the effects of surface roughness in the presence of surface blowing unfortunately have little foundation in physical modeling and even less support from experimental measurements. While there have been a series of experimental studies from Nikuradase to Holden to determine the effects of surface roughness, skin friction, and heat transfer, little work has been done to examine the separate and combined effects of surface blowing and surface roughness on the heat transfer and skin friction to rough surfaces. In fact, only two studies, one conducted in low speed flow (v = 50 ft/sec) by Healzer et al,[21] and a second by Voisinet[22] in a wind tunnel wall in a Mach 3 airflow in the absence of heat transfer, (where the key parameters were orders of magnitude different from those encountered in hypersonic re-entry), are available to substantiate theoretical modelings.

In the Healzer studies, the surface was constructed with hemispherical roughness elements while Voisinet employed a porous surface constructed from wire mesh. In both cases, an effective sand-grain roughness height was selected from Nikuradase[23] or Dirling[24] correlations of low speed roughness measurements. In the Healzer studies, the skin friction measurements were deduced indirectly from velocity profiles and momentum-integral techniques. While this reduction technique can be relatively accurate for the non-blowing case, when applied to experiments with surface blowing, the accuracy of the technique is poor. Apparently, this was the case because Healzer did not present correlations of his skin friction measurements. One very interesting feature of the results of the Stanford[25] study is the form of this expression to correlate the effects of heating on rough walls:

$$\frac{St_{BLOWING}}{St_{UNBLOWN}} = \left[\ln\left(1 + \frac{\rho_\omega V_\omega}{\rho_e U_e C_H}\right)\right]^{1.25} \cdot \left(1 + \frac{\rho_\omega V_\omega}{\rho_e U_e C_H}\right)^{1/4}$$

This is very similar to the form of the correlation developed at Stanford for smooth walls. Here it should be noted that the non-blowing value of heating coefficient was taken at the same enthalpy thickness as in the blowing case, rather than at a common Reynolds number based on scale length. These measurements were compared with a prediction scheme based on a modified Van Driest method for rough walls; however, because they were tailored to this specific experiment, they have not been used in shape change codes.

Voisinet's[26] studies of the combined effects of roughness and blowing were conducted at Mach 6 under adiabatic wall conditions ($q_w = 0$) on a wind tunnel wall, and only surface skin friction measurements were made. This is unfortunate because while modified Reynolds analogy relationships (however poor) have been developed for rough walls, linking skin friction to heat transfer in the presence of both roughness and blowing is a very difficult theoretical task. However, Voisinet's measurements have clearly demonstrated that the combined effects of flowing and roughness on skin friction cannot be described in a simple manner. First, Voisinet found that on the tunnel wall, where the experiments were conducted, the effects of surface roughness alone on skin friction could be correlated in terms of the roughness Reynolds number, $\tilde{R}e_K$; a result consistent with earlier measurements on adiabatic walls by Goddard[27] and Reda[28]. In contrast, measurements on models placed in the flow involving significant levels of heating ($T_w/T_o > 0.5$) have in general correlated better with parameters like

58

K/δ, K/θ or K/δ_T; which, as shown by the theoretical studies of Dvorak and Finson, should have greater relevance to roughness effects on re-entry vehicles. Voisinet's studies demonstrated that the effects of surface rougness and blowing on skin friction cannot be deduced from simple expressions derived from the measurements made of each of the separate effects. While correlations were presented to enable skin friction to be deduced in the presence of combined roughness and blowing, extrapolating these measurements to flows at higher Mach numbers over highly cooled surfaces, as well as inferring changes in heat transfer from the skin friction measurements, is clearly highly speculative.

A correlation of the measurements on transpiration-cooled "smooth" flat plates and cones at lower Mach numbers are shown in Figure 38a. Measurements by Holden[1] on transpiration cooled nosetips and are compared with the earlier measurements in Figure 38b. These measurements are compared with the results of current studies in Section 4.3.

Because the current theoretical models such as those developed by Finson[29] and Lin and Bywater[30] are capable of describing in detail the flow over rough surfaces constructed with well-defined roughness geometries, there remains little value in continuing to conduct experiments on with poorly defined roughness and blowing characteristics surfaces, such as those constructed with sand grains or sintered materials. Correspondingly, the macroscopic irregularities of the blowing from most porous screen materials, coupled with their poorly defined roughness characteristics, makes it difficult to unambiguously interpret the experimental studies with the detail required to evaluate the key empirical relationships used in the theoretical modeling. To advance the state of the art in the prediction of ablation and shape change of MRVs, research requires a program of experimental research in which both heat transfer and skin friction measurements are made on models with well-defined roughness and blowing characteristics. Such experimental studies must be conducted in high Reynolds number, high Mach number flows if the blowing and roughness effects are to be simulated correctly, particularly in region of shock-boundary layer interaction.

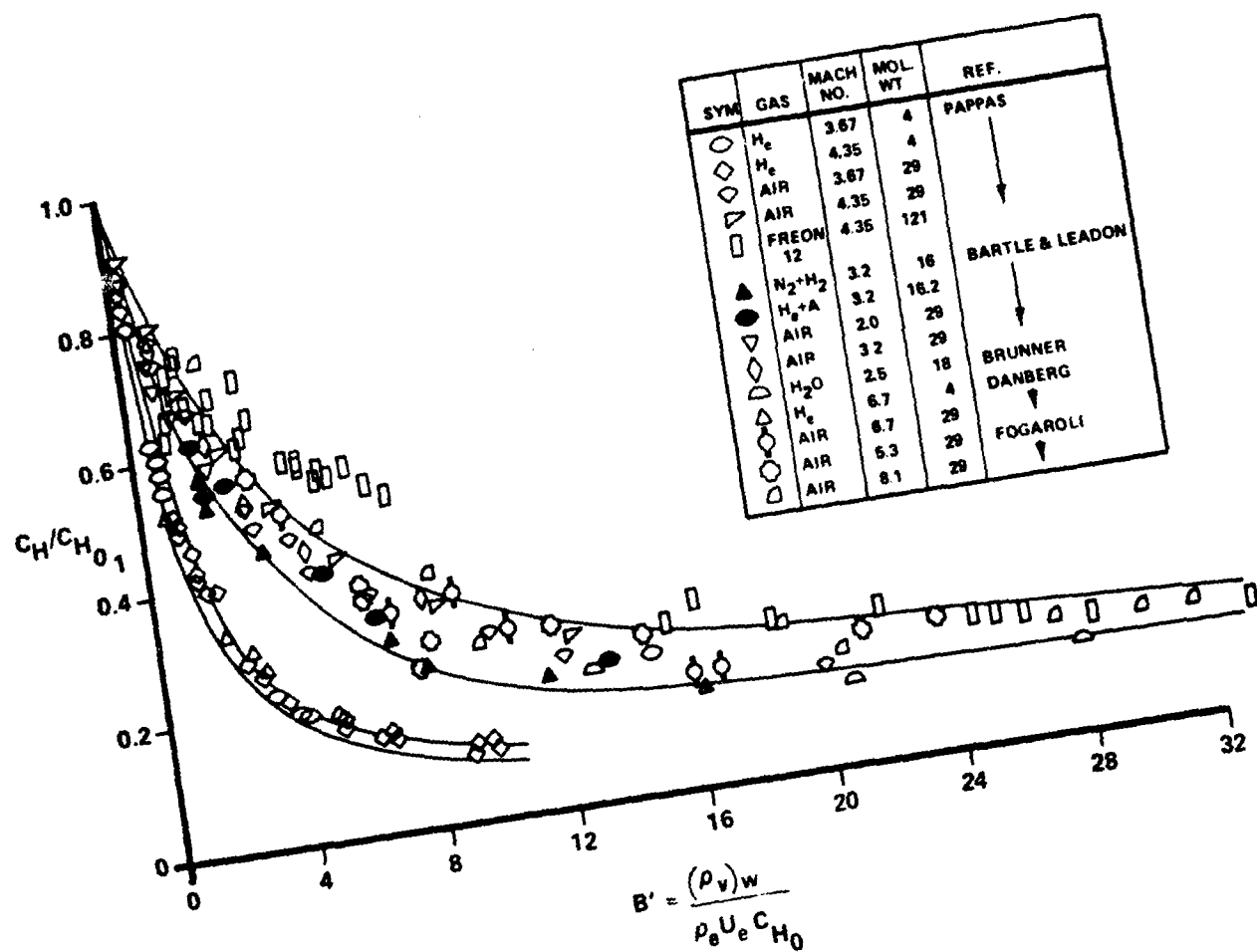| SYM	GAS	MACH NO.	MOL WT	REF.
○	H_e	3.67	4	PAPPAS
◇	H_e	4.35	4	
◇	AIR	3.67	29	
▷	AIR	4.35	29	
▯	FREON 12	4.35	121	BARTLE & LEADON
▲	N_2+H_2	3.2	16	
⬤	H_e+A	3.2	16.2	
▽	AIR	2.0	29	
◇	AIR	3.2	29	BRUNNER
◇	H_2O	2.5	18	DANBERG
△	H_e	6.7	4	
◇	AIR	6.7	29	FOGAROLI
◇	AIR	5.3	29	
◁	AIR	8.1	29	

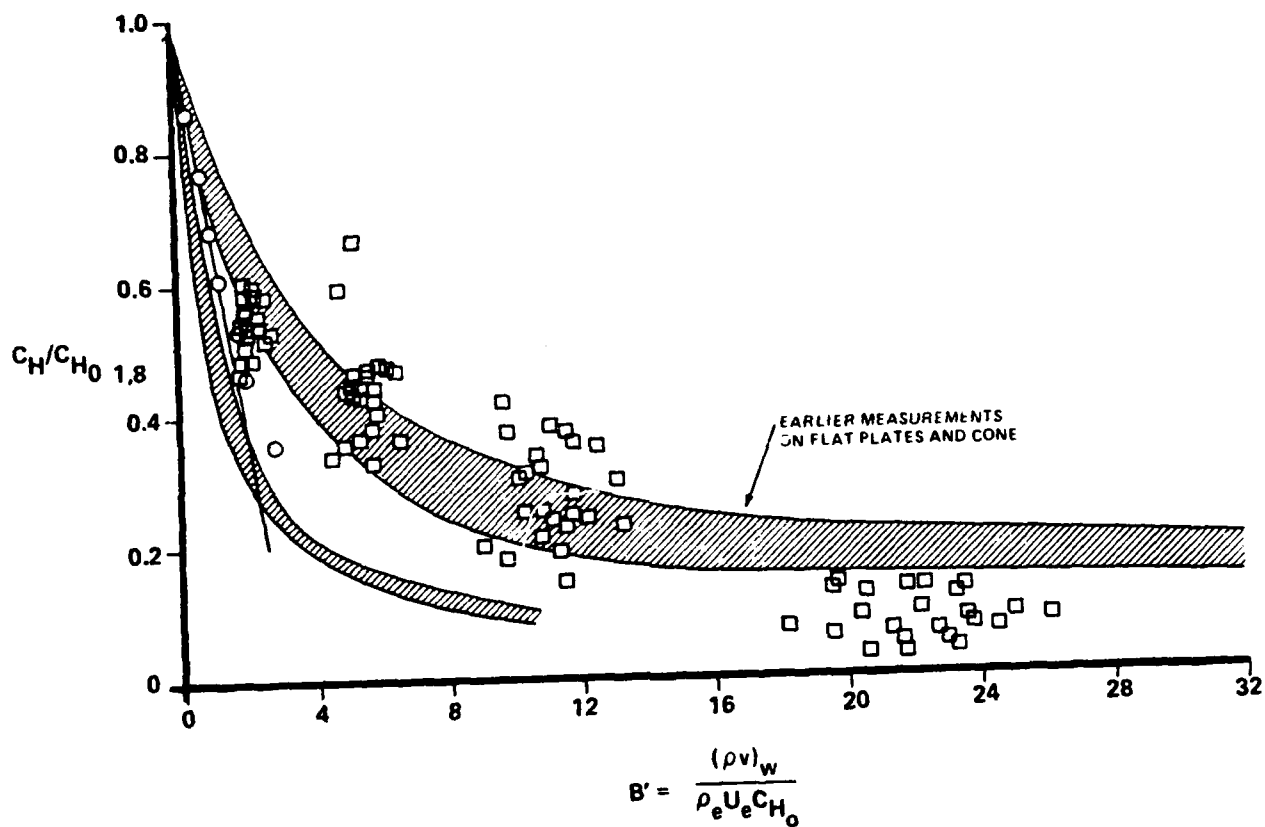Figure 38a   SUMMARY OF BLOCKAGE HEATING FROM EARLIER STUDIES ON FLAT PLATES AND CONES IN TURBULENT FLOW

Figure 38b COMPARISON BETWEEN THE MEASUREMENT MADE ON THE TRANSPIRATION-COOLED NOSETIPS WITH NITROGEN INJECTANT AND THE EARLIER BLOCKAGE DATA

61

3.3   OBJECTIVE AND DESIGN OF THE EXPERIMENTAL PROGRAM

The objective of this experimental study of blowing and roughness effects in high Reynolds number hypersonic flow was to obtain detailed heat transfer and skin friction as well as flow field measurements to evaluate the models of the surface/flow field interaction. The development of computer codes which, in principal, can be used to describe the macroscopic features at the base of the boundary layer, has basically outmoded the use of surfaces with poorly defined roughness characteristics such as "sand grain" roughness. An in-depth review of surface roughness studies suggests that the definition of sand grain roughness is related more to a theoretical criteria based on a measured velocity profile rather than the geometric characteristics of the surface. In fact, Nicaradase[31] who first introduced sand grained roughness based bonding sand grains "end to end" to a surface noted found that sand of the same size from a different geographic location exhibited different roughness characteristics. From the viewpoint of generating measurements with which to provide a definitive evaluation of predictive techniques, it is important that the roughness geometry is well defined. Schlicting was the first researcher to obtain measurements on surfaces whose geometric roughness could be reproduced in both theoretical and experimental studies. From the results of these and subsequent studies in subsonic, adiabatic flows, an empirical relationship was devised between roughness shape and spacing and an "effective sand-grain roughness height." The correlation of the measurements further perpetuated the use of "sand grain roughness" as a standard. The single parameter characterization used in many "shape-change" codes designed to predict change in the noseshape of an ablating nosetip as it re-enters the atmosphere is based principally on measurements in low speed, low temperature flows at Mach numbers and Reynolds numbers differing significantly from re-entry conditions. In these studies, the surfaces were characterized by parameters such as k/d, k/θ and Tw/To. The roughness shape parameter (λ), which has been defined in various ways by different investigators, can be generally expressed as the product of the spacing ratio (D/K) and a parameter related to the shape of the roughness element or its drag coefficient. The relationship between K/Ks and the shape parameter λ (the lambda curve shown in Figure 1) exhibits large changes in Ks for small changes in the λ and a key question is whether the correlation is sensitive to flow structure between the roughness elements resulting from changes in the local Mach number and Reynolds number.

3.4   EXPERIMENTAL PROGRAM

3.4.1   Experimental Facilities and Test Conditions

The experimental program was conducted in Calspan's 96-inch Shock Tunnel at freestream Mach numbers from 11 to 16, for Reynolds numbers up to 100×10^6 and wall-to-freestream stagnation temperature ratios of 0.1 and 0.2. At Mach numbers up to 13, boundary layer transition is complete on the completely smooth models within six inches of the nosetip. For the blowing model at Mach numbers up to 16, transition is within six inches from the nosetip. These studies were conducted at roughness Reynolds numbers $(\tilde{R}e_K)$ from 20 to 300 on the conical forebody and 200 to 2000 on the flap, thus covering transitional to fully rough regime. Non-dimensional blowing rates, $\dfrac{\dot{M}}{\rho_e U_e C_{HO}}$, from 0 to 0.5 were used in the studies, with both uniform and spatially varying blowing rates.

3.5   MODELS AND INSTRUMENTATION

3.5.1   Models

A small MRV configuration with three nosetip sizes was constructed for AFWAL for these studies. This model (shown in Figure 39) has transpiration cooled surfaces fed from eight high-pressure reservoirs through eight Valcor fast acting valves. Each section of the model is constructed with six zones that run from the front to the rear of the model. This enabled us to vary the blowing circumferentially to simulate the effects of differential blowing resulting from model incidence. To distribute the gas from the reservoirs uniformly to the surface, each model employs three inserts (see Figure 40); each insert contains a matrix of distribution passages. Figure 41 shows the inserts and the porous surface for the MRV configuration. The porous force flap is shown in Figure 42.

3.5.2   Construction of the Rough and Smooth Surfaces

In our earlier studies of the effects of patterned roughness on the aerothermal characteristics of MRVs, we used hemispherical roughness elements. A molding technique that was developed at Calspan to produce a number of different roughness patterns was used to obtain the smooth and rough surfaces. The low velocity
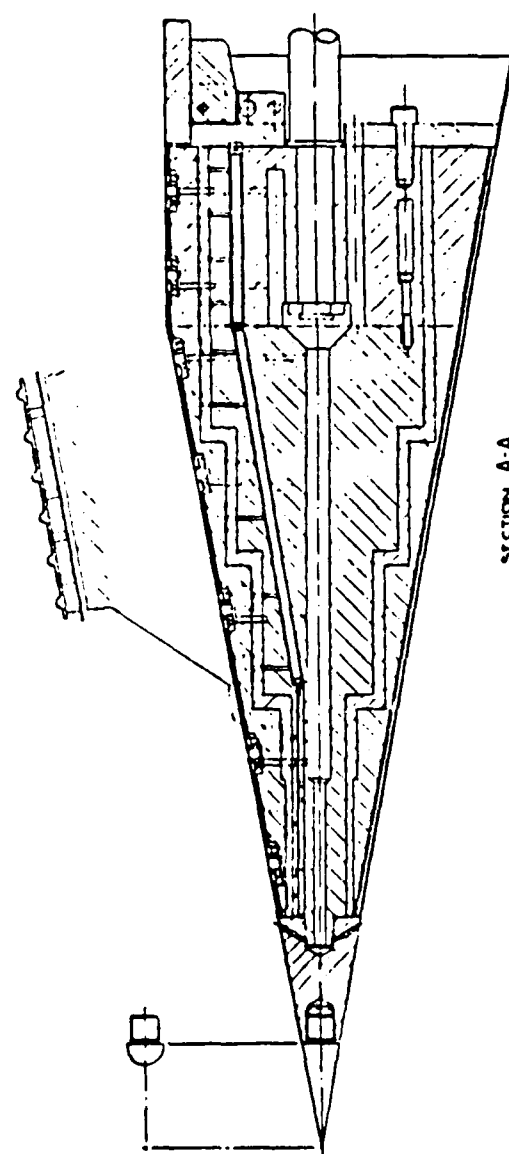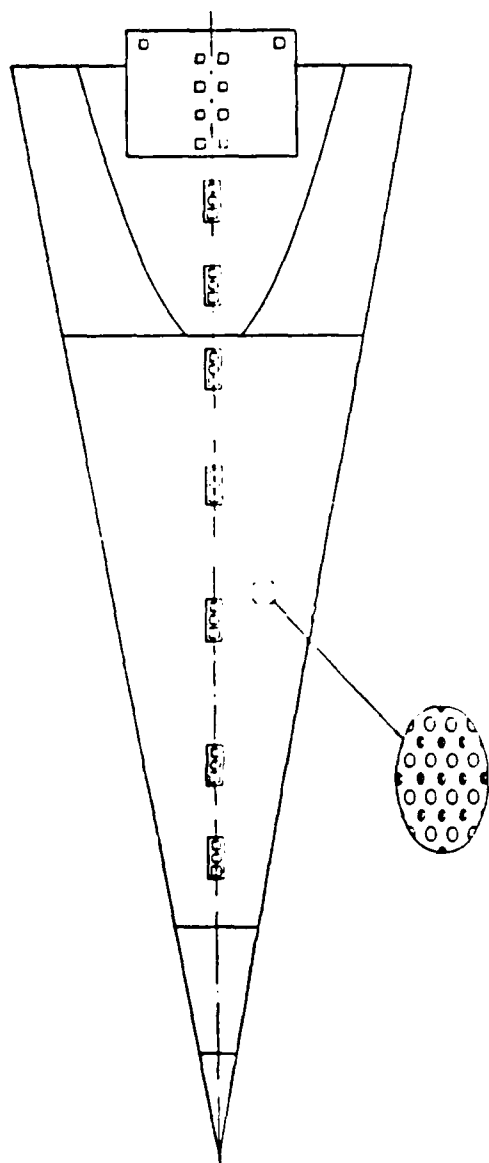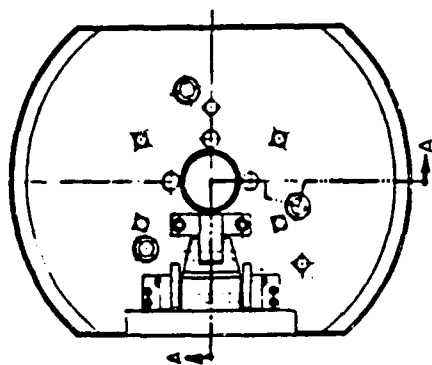
63
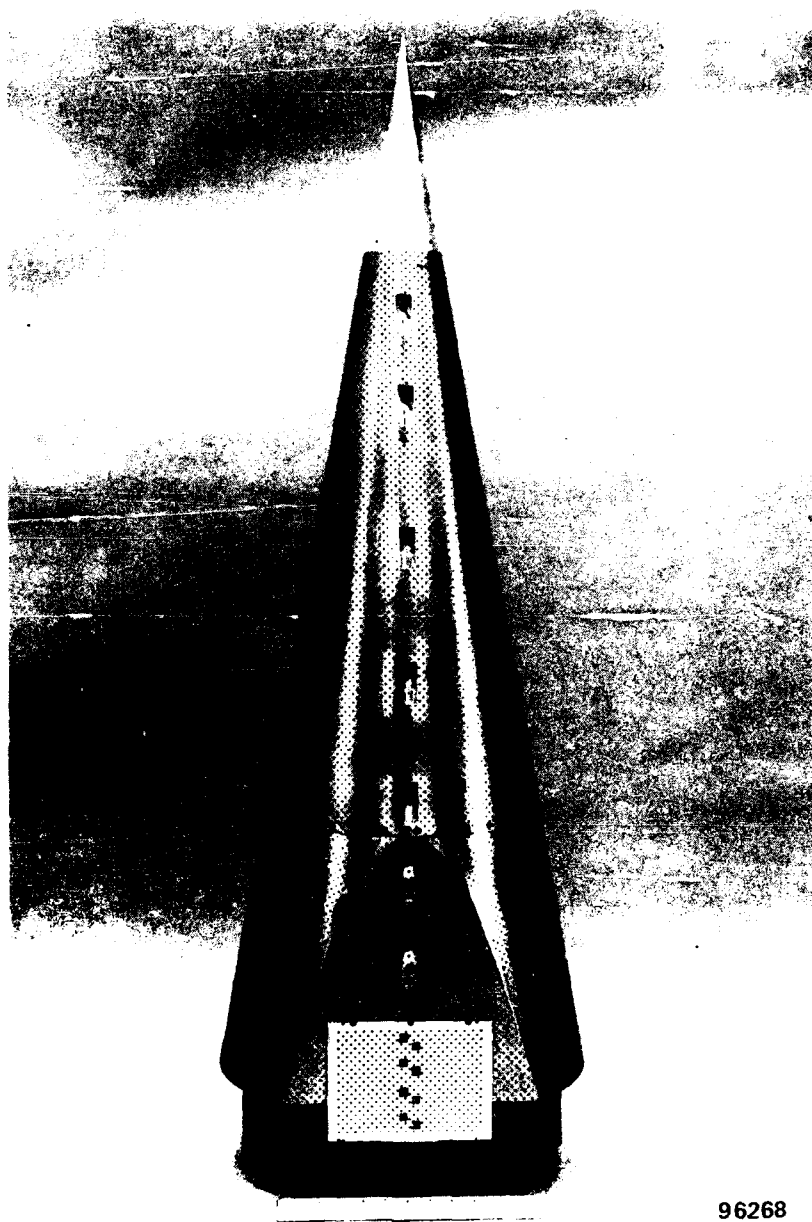
96268

Figure 39   SMALL MRV MODEL

Figure 40 ROUGHNESS BLOWING MODEL

SECTION A-A

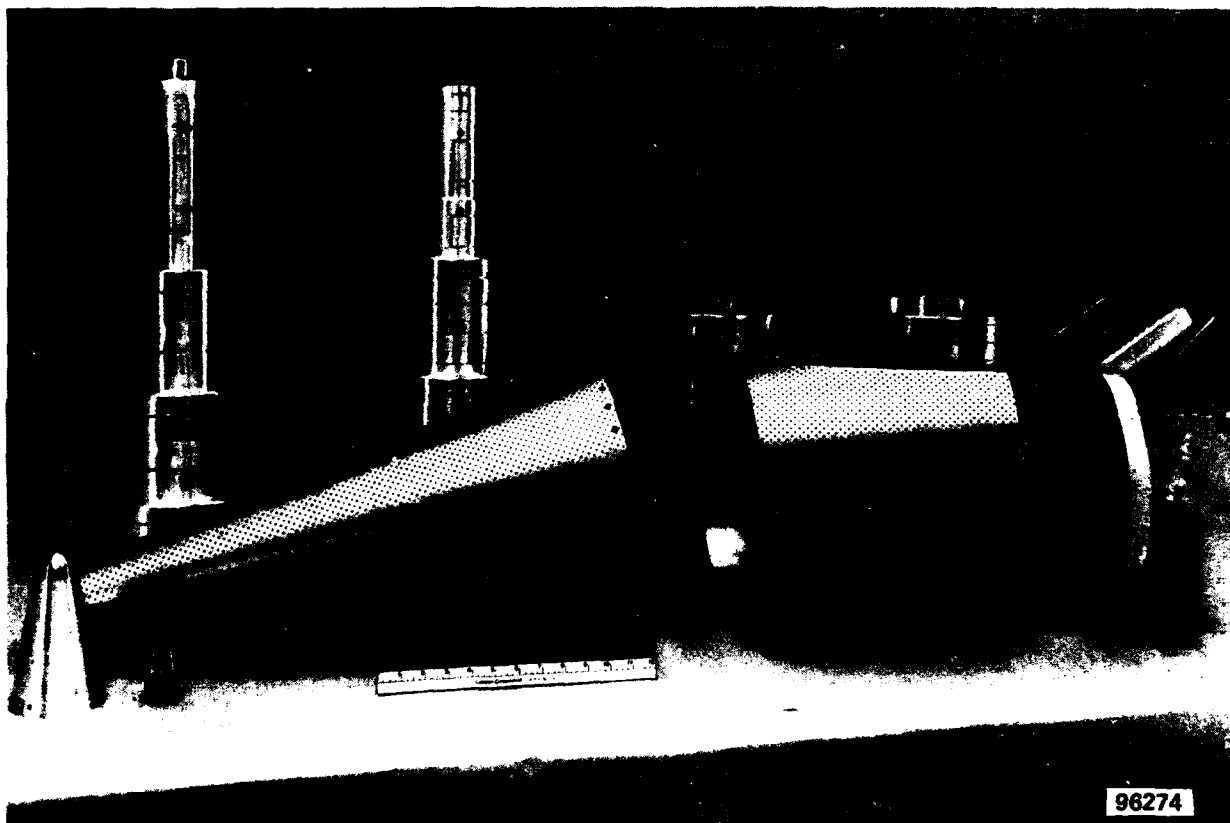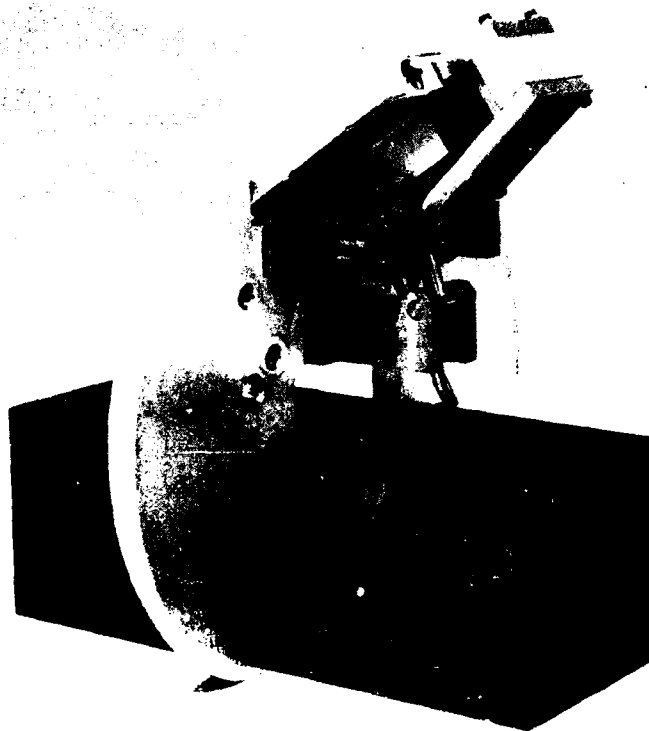Figure 41   MRV MODEL SHOWING INSERTS AND POROUS SURFACE

96273

Figure 42   POROUS FORCE FLAP

mass addition between each roughness element occured from passages molded in the skin between the flow, which was controlled by sonic orifices at their base. This latter technique was employed very successfully in our earlier transpiration-cooled studies where we were able to obtain precisely controlled blowing conditions. The flow from each hole in the model was controlled by eight sonic orifices in the model skin that were fed from plenum chambers in the model. The flow from each orifice was released into a cylindrical passage molded in the rubber skin between each roughness element. The area ratio between the orifice and circular passage allowed injectant flows from the surface at velocities of approximately 100 ft/sec. While this type of model construction is a painstaking task, the end result--an experiment where surface roughness and blowing are completely defined--is worth the effort. Because we used choked orifices over the entire model, mass flow from each model zone was precisely controlled by plenum pressures. Mass flows over the model were unaffected by the distribution of surface pressure on transients associated with tunnel starting. Although spherical roughness elements were used in the current studies, this technique can be used to construct rough surfaces that replicate any ablated surface.

3.5.3   Surface Instrumentation

The heat transfer instrumentation developed to measure the surface distribution of heat transfer to the roughness is shown in Figures 43 and 44. Eighteen of these units, each with 13 heat-transfer gages, were constructed. The two instrumented hemispherical roughness elements can be rotated in the holder to provide measurements on the windward and leeside surfaces of the element. Also, the gage can be rotated in the holder to provide greater details of the heat transfer at the base of the roughness elements. As in the rest of the model, the blowing velocities were in the range of 80 to 300 ft/sec, generating dynamic pressures of less than 1% of the freestream values.

A blowing calorimeter gage developed specifically for this program is shown in Figure 45. The calorimeter element is minted from a high-purity silver billet and drilled to accent the passages for the blowing holes. The back of the gage is highly polished and the electrically insulating, but thermally conducting films are evaporated on this surface. A nickel resistance thermometer is then deposited on the insulation layers (Figure 43). The calorimeter element is mounted in a Macor holder and the passages for the coolant are installed with a highly insulating adhesive. Twenty of these transducers were designed and constructed.
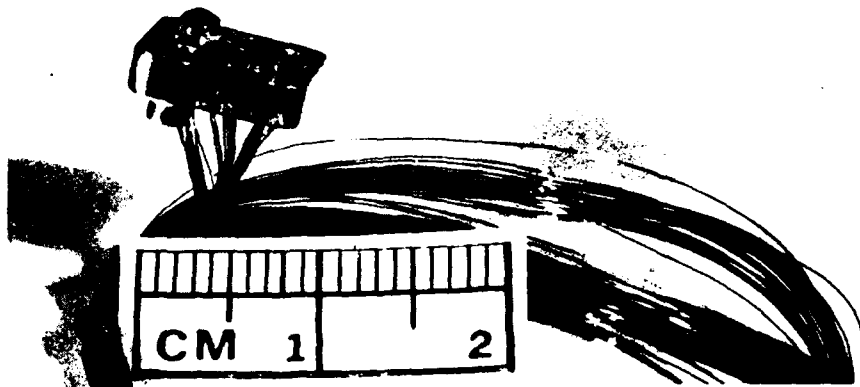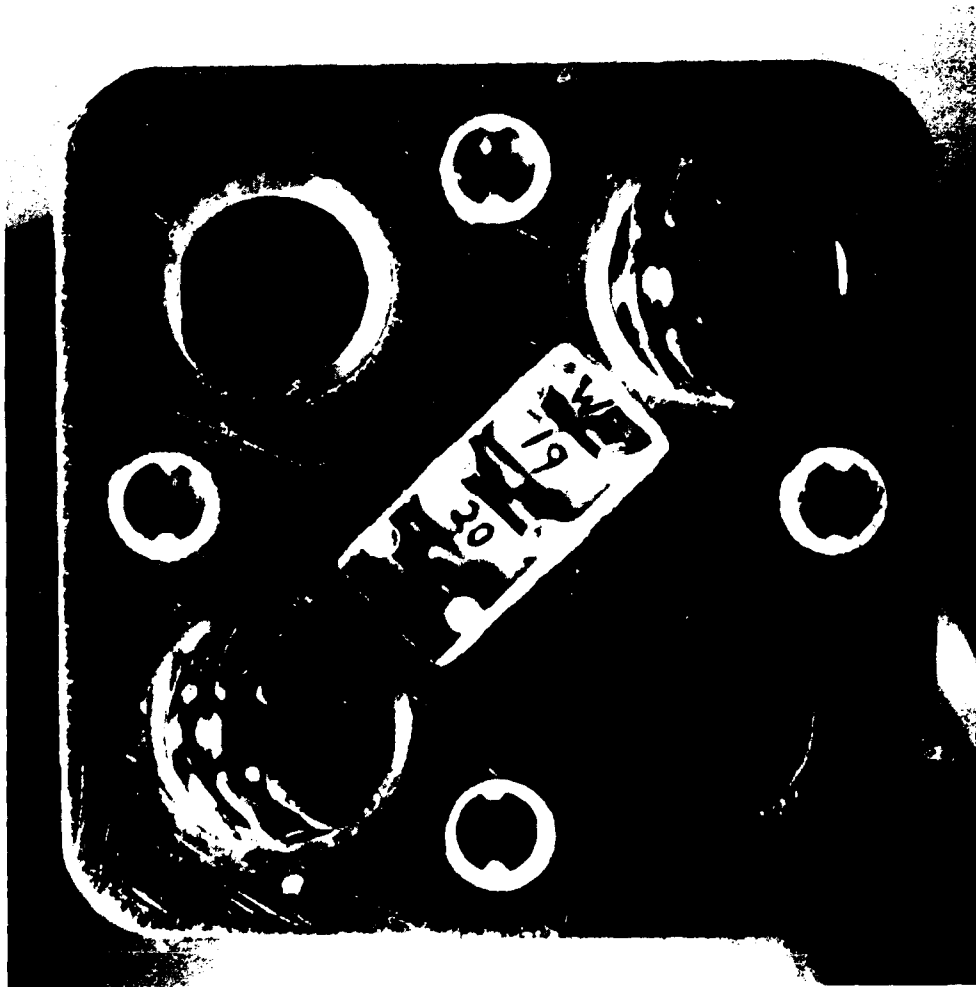
68

Figure 43   THIN FILM GAGES

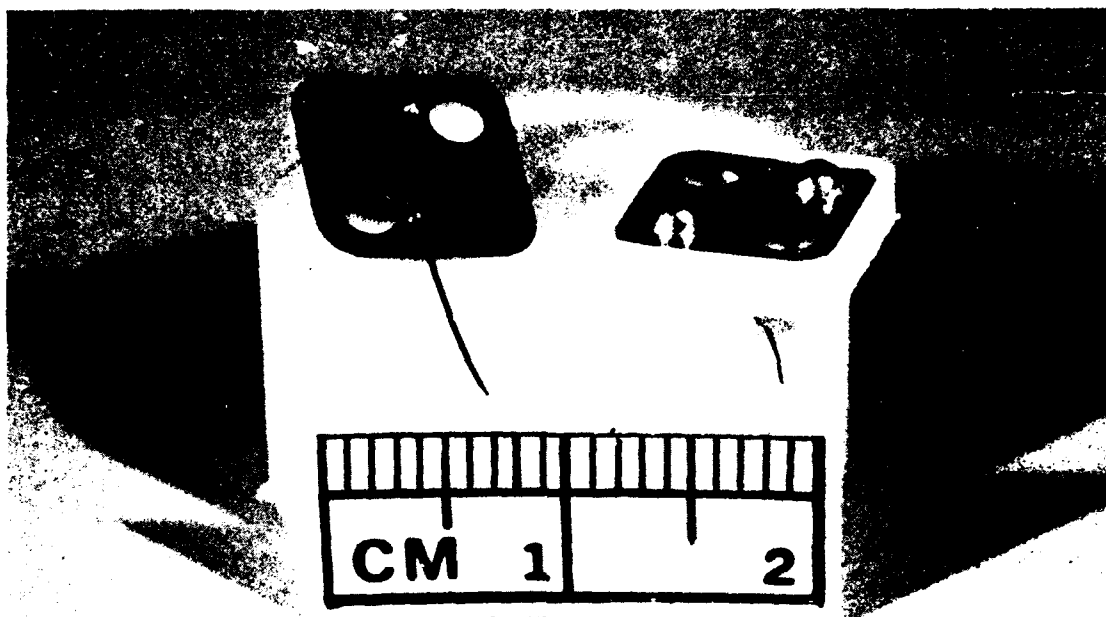Figure 44   THIN FILM GAGE VIEWED FROM ABOVE

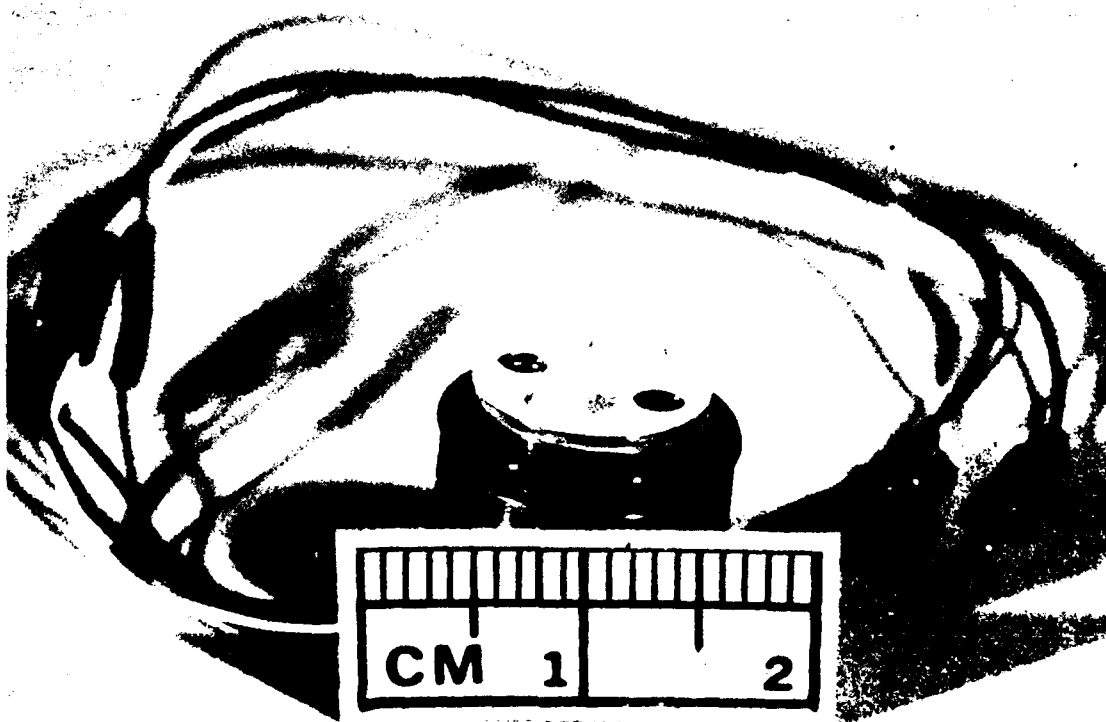Figure 45   CALORIMETER GAGE

Figure 46   SKIN FRICTION GAGE

70

One of the skin friction gages that was designed, developed and constructed is shown in Figure 46. After a number of different approaches were tried, a design was developed with non-metric coolant passages passing through the metric diaphragm with very little clearance. Such tight clearances are allowed because the crystal and rubber support and measuring system on which the diaphragm is mounted is very stiff, so that deflection under load is insignificant. The gage has a linear response up to 0.7 psia and a nominal sensitivity of 20,000 mV/psi.

Pressure measurements were made using flush-mounted Kulite transducers. Pressure gages have been mounted flush with the silicon skin to record the pressure fluctuations, as well as the mean pressure on the flap resulting from the unsteady shock-wave/turbulent boundary layer interaction at the cut/flap junction. Such information is required to specify the vibration environment on the flap as well as to provide insight into the base flow structure.

3.5.4   Holographic Interferometry

Holographic interferometry was used to make flowfield measurements. Interferograms of complex flowfields provide good qualitative basis for evaluating some of the important phenomena that control the characteristics of these flows. CUBRC's holographic recording system was used in this study. Both single plate and dual plate techniques are required to record holograms, which are subsequently used in the playback step to obtain shadowgrams, Schlieren photographs, and interferograms of the tests. The holographic interferometry measurements made in the current blowing and roughness studies are discussed in Section 2.3.9.

Figure 47 shows a typical example of a single plate holographic interferogram. This hologram was made by double-exposing a single plate, first with the reference beam just before the test, and then approximately 15 minutes later, with the scene beam of the test. Here, the interferogram was fixed in the hologram. In this interferogram, the model wall appears as a solid black surface, while in the interferogram reconstructed using the dual plate technique, the model appears as a gray silhouette. The photographs show enlargements of 35mm photographs of the reconstructed object waves as viewed through the eyepiece of a 20X telescope. Because this direct viewing approach was used, details in the hologram can be magnified to achieve pictures of greater clarity than would otherwise be obtained. Since the hologram

71

Figure 47 FLOW STRUCTURE IN A TWO DIMENSIONAL CORNER FLOW (M=11 R_{e_L} = 30 x 10^6)

results from the integrated effects of density changes from the beam splitter to the recording plane, these photographs must be interpreted with care, especially in and close to regions of separated flow.

Section 4
RESULTS AND DISCUSSION

4.1 INTRODUCTION

The experimental studies were conducted at Mach Numbers of 11 and 13 for a range of blowing rates (B' from 0.01 to 5). Both sharp and blunt nosetip configurations were employed in this study, however the principal emphasis was on flows which were not influenced by entropy swallowing effects. The molecular weight of the injectant was varied by diluting the principal injectant nitrogen with helium to provide a gas with a molecular weight similar to that of a typical ablator. A major objective of the current study was to investigate the effects of blowing on boundary layer separation and to this end, measurements were made for a series of flap angles for which, in the absence of blowing, the flow was attached. We also studied the effects of blowing and roughness on flows which were well-separated. A matrix of the runs made in the current experimental program is shown in Figures 48 and 49, and the test conditions reported in Figures 50 and 51.

4.2 PERFORMANCE OF NEW HEAT TRANSFER AND SKIN FRICTION INSTRUMENTATION

A major accomplishment under the present contract was the development three new types of instrumentation to obtain detailed measurements in the presence of roughness and blowing. To provide information which is of direct value to those attempting to model the macroscopic flow mechanics around the roughness elements, we must provide measurements of the heat transfer distribution around and at the base of the roughness elements. These measurements would be of little use if the gages themselves were not an integral part of the blowing surface with the injected gas passing through and flowing over the sensing element. Clearly, such requirements significantly complicate the design and construction of the gage. However, these very difficult problems were overcome, and a series of very unique measurements were obtained.

74

Run #	Mach #	Reynolds # (10 6/Ft)	Reservoir (Psia)	Injectant	Flap Angle (Deg)	A.O.A. (Deg)	Nose Type
2	13	5.0	0	Nitrogen	15	0	Sharp
3	13	5.0	0	Nitrogen	15	0	Sharp
4	13	5.0	100	Nitrogen	15	0	Sharp
5	13	5.0	100	Nitrogen	15	0	Sharp
6	13	5.0	200	Nitrogen	15	0	Sharp
7	13	5.0	500	Nitrogen	15	0	Sharp
8	13	5.0	50	Nitrogen	15	0	Sharp
9	13	5.0	50	Nitrogen	25	0	Sharp
10	13	5.0	200	Nitrogen	25	0	Sharp
11	13	5.0	500	Nitrogen	25	0	Sharp
12	13	5.0	100	Nitrogen	25	0	Sharp
13	13	5.0	75	Nitrogen	25	0	Sharp
14	13	5.0	10	Nitrogen	25	0	Sharp
15	13	5.0	350	Nitrogen	25	0	Sharp
16	13	5.0	100	N2/He	25	0	Sharp
17	13	5.0	35	N2/He	25	0	Sharp
18	13	5.0	250	N2/He	25	0	Sharp
20	13	5.0	80	Nitrogen	30	0	Sharp
21	13	5.0	35	Nitrogen	30	0	Sharp
22	13	5.0	650	Nitrogen	30	0	Sharp
23	13	5.0	250	Nitrogen	30	0	Blunt
24	13	5.0	80	Nitrogen	30	0	Blunt
25	13	5.0	35	Nitrogen	35	0	Sharp

Figure 48   TEST MATRIX FOR THE BLOWING AND ROUGHNESS STUDIES

Run #	Mach #	Reynolds # (10 6/Ft)	Reservoir (Psia)	Injectant	Flap Angle (Deg)	A.O.A. (Deg)	Nose Type
26	13	5.0	80	Nitrogen	35	0	Sharp
27	13	5.0	250	Nitrogen	35	0	Sharp
28	13	5.0	80	N2/He	35	0	Sharp
29	11	4.0	35	Nitrogen	25	0	Sharp
30	11	4.0	80	Nitrogen	25	0	Sharp
31	11	4.0	0	Nitrogen	25	0	Sharp
32	11	10.0	300	Nitrogen	25	0	Sharp
33	11	10.0	120	Nitrogen	25	0	Sharp
34	11	10.0	35	Nitrogen	25	0	Sharp
35	11	10.0	700	Nitrogen	25	0	Sharp
36	11	10.0	80	N2/He	25	0	Sharp
37	11	10.0	200	N2/He	25	0	Sharp
38	11	10.0	40	N2/He	25	0	Sharp
39	11	10.0	300	N2/He	25	0	Sharp
40	15	1.5	15	Nitrogen	25	0	Sharp
41	15	1.5	40	Nitrogen	25	0	Sharp
42	15	1.5	100	Nitrogen	25	0	Sharp
43	13	7.0	90	Nitrogen	25	3	Sharp
44	13	7.0	40	Nitrogen	25	3	Sharp
45	13	7.0	300	Nitrogen	25	3	Sharp
46	13	6.0	90	Nitrogen	25	3	Blunt
47	13	6.0	90	Nitrogen	25	6	Blunt
48	13	6.0	40	Nitrogen	25	6	Sharp
49	13	6.0	90	Nitrogen	25	6	Sharp
50	13	6.0	300	Nitrogen	25	6	Sharp

Figure 49 TEST MATRIX FOR THE BLOWING AND ROUGHNESS STUDIES

Run	$P_o/10^4$ (Psia)	$H_o/10^7$ $(\text{ft/sec})^2$	T_o $^\circ R$	M	U ft/sec	T $^\circ R$	P (Psia)	Rho Slugs/ft^3
3	1.7860	2.1181	3063.0	12.968	6417.3	101.820	.076982	6.3447(-5)
4	1.8555	2.0879	3027.2	13.026	6372.1	99.500	.078939	6.6579(-5)
5	1.7671	2.0745	3011.5	13.003	6351.4	99.205	.075545	6.3905(-5)
6	1.8268	2.1142	3061.5	13.019	6412.0	100.870	.077164	6.4199(-5)
7	1.8100	2.0850	3025.8	13.028	6367.8	99.339	.076571	6.4686(-5)
9	1.7010	2.0126	2939.2	13.052	6256.5	95.549	.071542	6.2835(-5)
10	1.7815	2.1206	3073.3	13.031	6421.9	100.990	.074230	6.1681(-5)
11	1.8303	2.2023	3174.1	13.014	6544.2	105.150	.075595	6.0334(-5)
12	1.8320	2.1121	3059.7	13.029	6409.0	100.620	.077089	6.4231(-5)
13	1.8383	2.1364	3091.3	13.034	6445.9	101.710	.076666	6.3259(-5)
14	1.8366	2.1037	3048.2	13.025	6399.1	100.280	.077665	6.4996(-5)
15	1.8235	2.1237	3075.0	13.028	6426.6	101.180	.076408	6.3372(-5)
16	1.7693	2.0641	2997.2	12.997	6335.2	98.793	.076130	6.4669(-5)
17	1.8415	2.0137	3048.2	13.027	6396.1	100.250	.077837	6.5160(-5)
18	1.8528	2.1195	3069.3	13.037	6420.3	100.840	.077633	6.4605(-5)
20	1.7933	2.1111	3059.9	13.025	6407.5	100.630	.075254	6.2760(-5)
21	1.7983	2.1333	3088.5	13.028	6441.0	101.630	.074909	6.1853(-5)
22	1.7878	2.0882	3030.6	13.026	6372.6	99.531	.075458	6.3623(-5)
23	1.8753	2.1386	3092.2	13.032	6449.0	101.830	.078565	6.4745(-5)
24	1.8060	2.0894	3033.7	13.047	6374.8	99.273	.075531	6.3850(-5)
25	1.6813	2.0606	2996.34	12.994	6329.9	98.672	.071683	6.0966(-5)

Figure 50 EXPERIMENTAL TEST CONDITIONS

Run	$P_o/10^4$ (Psia)	$H_o/10^7$ (ft/sec)^2	T_o °R	M	U ft/sec	T °R	P (Psia)	Rho Slugs/ft^3
26	1.8528	2.1216	3073.2	13.048	6423.7	100.790	.077172	6.4254(-5)
27	1.7658	2.0785	3023.0	13.062	6358.3	98.528	.073123	6.2282(-5)
28	1.7993	2.0640	3002.2	13.058	6335.9	97.905	.075321	6.4562(-5)
29	.72940	1.7309	2598.2	11.006	5768.8	114.250	.092331	6.7820(-5)
30	.74835	1.7749	2655.0	10.998	5841.5	117.320	.094527	6.7618(-5)
31	.75930	1.7521	2625.9	11.012	5804.1	115.520	.095770	6.9572(-5)
32	1.7363	1.6998	2575.8	11.347	5723.5	105.800	.207250	1.6439(-4)
33	1.7585	1.7248	2609.1	11.354	5765.6	107.230	.208200	1.6294(-4)
34	1.7423	1.7265	2612.3	11.356	5768.4	107.290	.250350	1.6062(-4)
35	1.7263	1.7357	2624.8	11.353	5783.7	107.930	.202780	1.5767(-4)
36	1.7350	1.7200	3602.3	11.343	5757.4	107.130	.206210	1.6154(-4)
37	1.7435	1.7341	2621.6	11.351	5781.0	107.870	.205710	1.6004(-4)
38	1.6933	1.7223	2607.9	11.348	5761.3	107.180	.199160	1.5593(-4)
39	1.7123	1.6855	2557.2	11.343	569.2	104.980	.204900	1.6380(-4)
40	1 7995	4.0076	5484.8	15.867	8869.7	129.930	.012272	7.9261(-6)
41	1.8348	2.9248	4028.1	15.414	7572.9	100.370	.019757	1.6519(-5)
42	1.8133	2.9680	4080.7	15.396	7628.5	102.090	.019439	1.5979(-5)
43	2.0123	1.7570	2646.7	13.319	5849.1	80.192	.083197	8.7065(-5)
44	2.0323	1.7925	2693.2	13.326	5908.0	81.733	.082990	8.5211(-5)
45	2.0693	1.8393	2754.4	13.338	5984.8	83.714	.083076	8.3280(-5)
46	1.9748	1.8215	2733.0	13.329	5955.6	83.012	.079161	8.0027(-5)
47	2.0848	1.8666	2788.7	13.326	6028.8	85.111	.083643	8.2473(-5)
48	2.0440	1.8476	2766.1	13.341	5998.3	84.058	.081471	8.1337(-5)
49	2.0260	1.8653	2789.9	13.342	6027.0	84.854	.080084	7.9203(-5)
50	2.0383	1.8941	2827.2	13.343	6073.2	86.142	.079889	7.7829(-5)

Figure 51 EXPERIMENTAL TEST CONDITIONS

4.2.1   Design and Measurements with the New Skin Friction Gages

The skin friction gage (which is shown schematically in Figure 46) is an acceleration compensated single component force balance in which transpiration cooling passages are vented through the surface of the gage. A floating diaphragm, which in this particular design embodies two roughness elements, is supported flush with the surface on a piezoelectric sensing beam through a single fixture. The diaphragm is stabilized around its perimeter silicon posts which are molded into a gasket that contains a rubber boot which is cemented between the diaphragm and the body of the gage to prevent the hot gases from reaching the crystal beam. A second beam and diaphragm combination is incorporated into the body of the gage to provide a signal with which to acceleration compensate the transducer. The electrical signals from the sensing and compensation beam are added electrically in such a manner that when the gage is "shaken" in the absence of an air load, the net output is zero. The injection flow through the gage is metered through a series of sonic orifices set in the base of the gage. The geometric and mechanical design features of the gages were refined in a series of bench tests and tunnel studies. The developed gage has a frequency response of 20 kHz and a sensitivity of 20,000 mV/psi. A typical output of this skin friction instrumentation during a run with injection through the gage is shown in Figure 52. Seven blowing and roughness gages were constructed for this program and these gages were calibrated and used successfully in this program.

4.2.2   New "Roughness and Blowing" Heat Transfer Instrumentation

During the course of these studies we developed two new gages to measure heat transfer in the presence of roughness and blowing. The first was a calorimeter gage which measured the total heat transfer rate to a segment of the surface. The second was a gage which provided the detailed distribution of heat transfer over the roughness elements and on the base of the model between the roughness elements and on the base of the model between the roughness elements. In each case, the size and geometry of the gage was a selected so that it was representative segment of the roughness and blowing surface. Thus, we selected a rectangular segment which contained two roughness elements and two transpiration cooling ports.
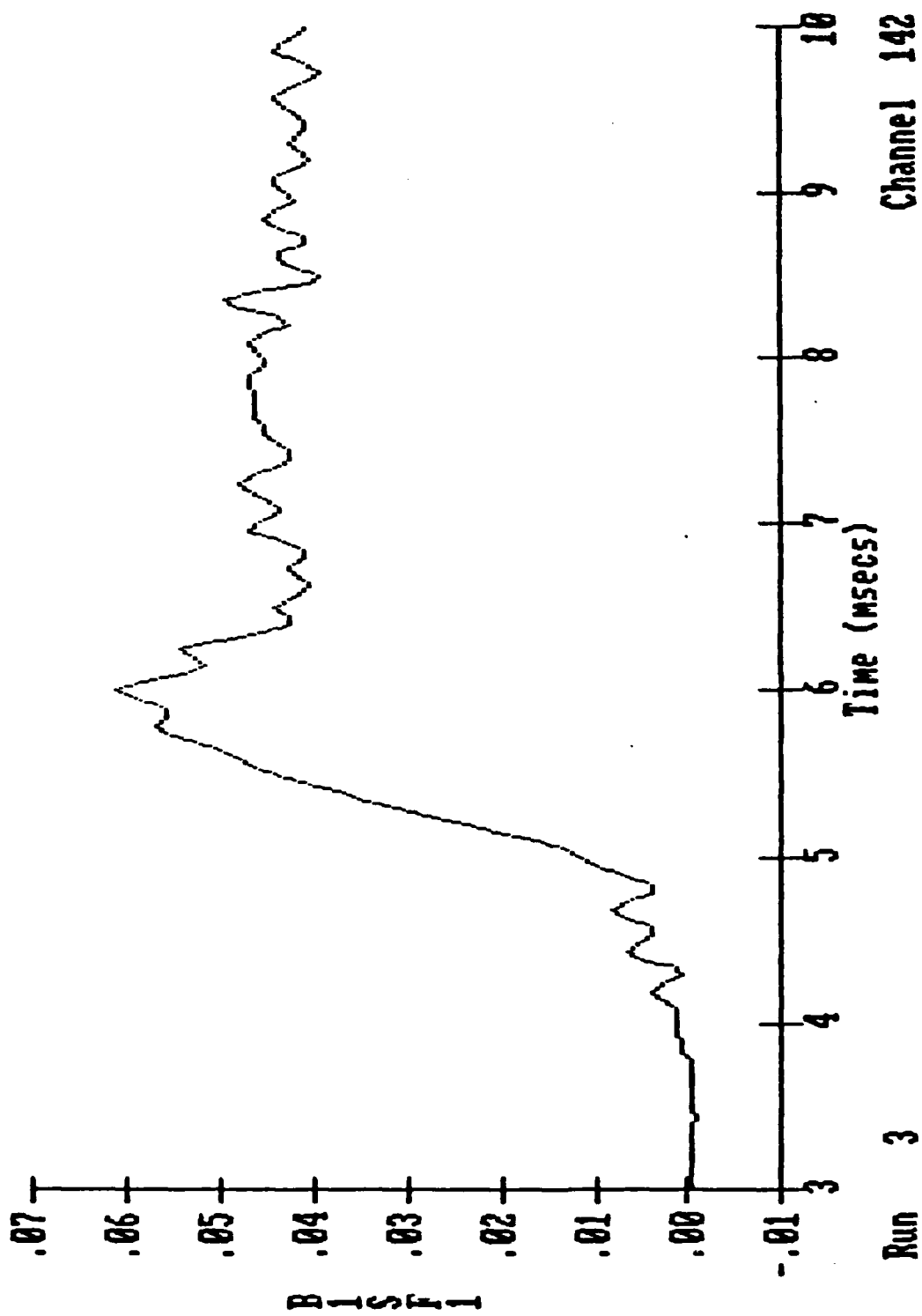
Figure 52   TIME HISTORY TRACE FROM SKIN FRICTION INSTRUMENTATION

80

4.2.3 Calorimeter Instrumentation

A photograph of the calorimeter gage is shown in Figure 45. The sensing element is a silver calorimeter slug the temperatue of which is measured with a nickel resistance thermometer attached to the rear surface. Two roughness elements are molded into the surface of the calorimeter slug as the element is minted from a pure silver billet. The rear surface of the gage is highly polished, and then coated with several different, thin, electrically insulating, but thermally conducting layers upon which the nickel film is deposited. While this gage is significantly more difficult to construct than one employing a thermocouple sensor peened into the base of the silver slug, attaining a sensitivity of almost an order of magnitude larger that the thermocouple gage is well worth the added effort. The calorimeter elements are cemented into a Macor holder with an ultra-low conductivity, polyurethane adesive which has a thermal diffusion depth of a fraction of a thousand during the 7 millisecond test time. This same adhesive was used to cement the transpiration tubes as they passed through the calorimeter element. Thus, during the test time, there was negligible loss in heating from this source or the evacuated rear surface of the gage. The injectant which passed through the gage was metered through a series of sonic orifices at the base of the passageway. The design and operation of these gages were refined in a number of bench tests and tunnel studies. While dynamic calibrations have been performed with a high powered laser heat source, we have found that computing the sensitivity on the basis of measuring the mass of the pure silver slug and the temperature coefficient of the nickel resistence thermometer consistantly gives the most accurate results. A typical output from the calorimeter gages is shown in Figure 53. The gage has a response time of less than a millisecond. A sliding least-squares technique is used to fit the temperature record, and this curve-fit is differentiated to obtain the temperature rate of change required to calculate the heat transfer rate. Fifteen of the calorimeter gages were constructed and used successfully in this program.

4.2.4 Thin Film Heat Transfer Instrumentation

The miniature thin film instrumentation employed in this study enabled, for the first time, detailed distributions of heat transfer to be obtained on the actual roughness elements and on the cone surface adjacent to the injection ports and the roughness elements. Again, the size of the gage was selected to give a representative segment of the surface. Each gage contained 11 individual heat transfer gages. The
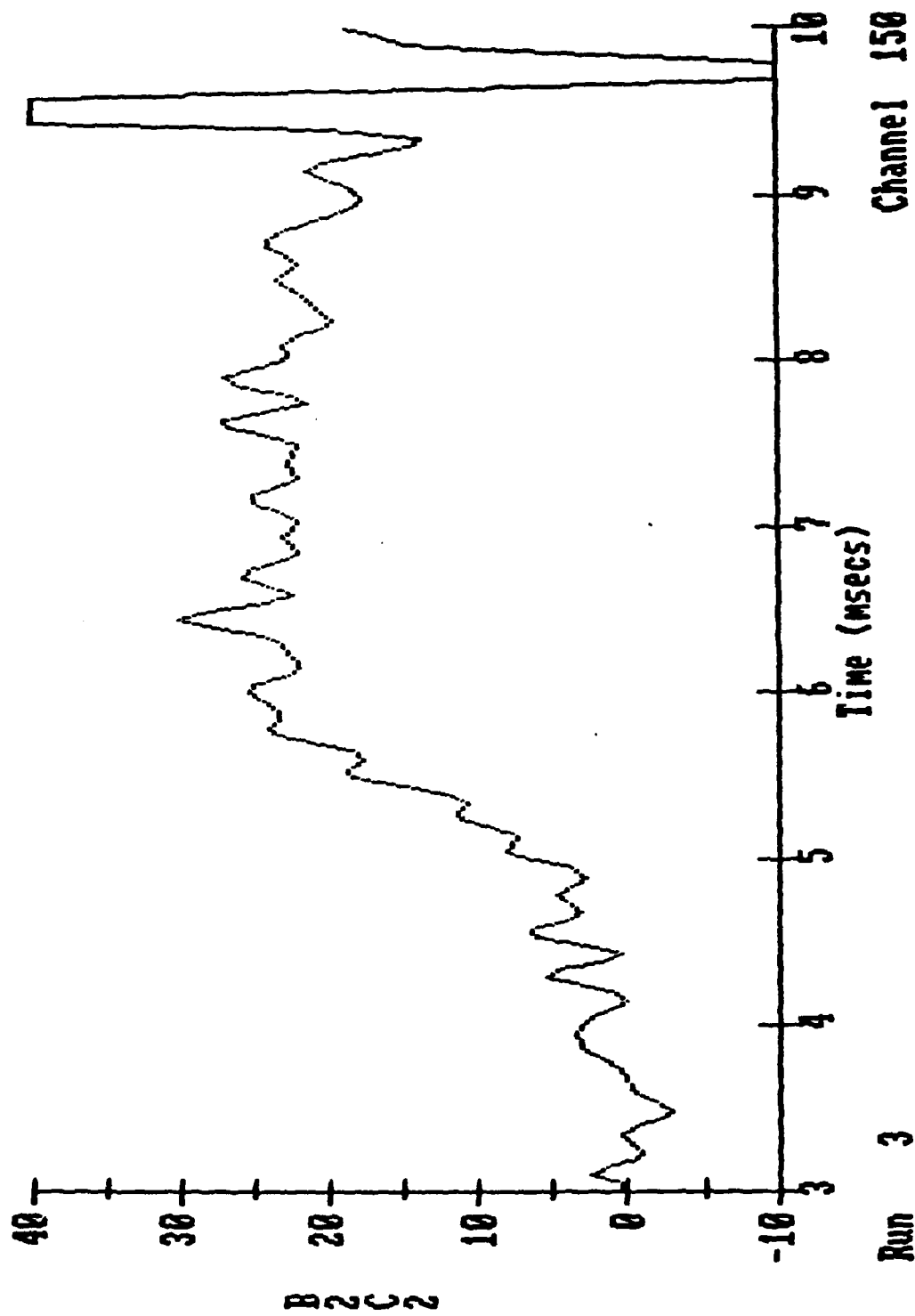
Figure 53   HEAT TRANSFER TIME HISTORY FROM CALORIMETER INSTRUMENTATION

82

positioning of the 7 thin films around the base of the roughness elements and around the injection ports was selected to provide distribution of heating in sufficient detail to infer the key aerothermal phenomena (see Figures 43 and 44). Likewise the five measurements over the roughness elements, which could be oriented relative to direction of the free stream, were selected to obtain the heating loads as well as provide evidence to define the micro-structure of the flow. Two injection passages run through the body of the gage, and as in the calorimeter and skin friction gages, the flow through these passages are regulated by sonic orifices at the base of these tubes. The temperature coefficients of the thin film resistance elements are measured in an oil bath and we employ the thermal properties of the pyrex substrate. The heat transfer rate (a record of which is shown in Figure 54) is derived from the surface temperature/time history using the Rae/Tauble algorithm (Ref. 46a).

4.2.5 Pressure Instrumentation

Kulite pressure transducers were used to measure the pressure along the model and over the flap in these studies. The small sine of these gages (0.064 dia.) enabled us to position this instrumentation between the roughness elements and the injection ports. A typical pressure/time history obtained from this gage is shown in Figure 55.

4.3 EFFECTS OF TRANSPIRATION COOLING ON SURFACE SKIN FRICTION AND HEATING AND PRESSURE

The effects of mass addition on the skin friction and heat transfer to the rough cone/flap configuration were investigated at Mach numbers of 11, 13 and 16 for a range of blowing rates (B') from 0 to 10. A test matrix of these studies is given in Figures 48 and 49 and a listing of the run conditions are tabulated in Figures 50 and 51.

Figure 56 shows the distribution of heat transfer rate to the surface of the rough cone/flap model for a range of blowing rates at Mach 11. The distribution of heating rate on the cone surface and over the roughness elements are shown for each gage station along the model. Here we observe that in the absence of blowing the peak heating on the roughness elements is typically 10 times the levels at the base of the roughness elements. At the higher blowing the peak-to-base heating ratios have dropped to values close to 3.
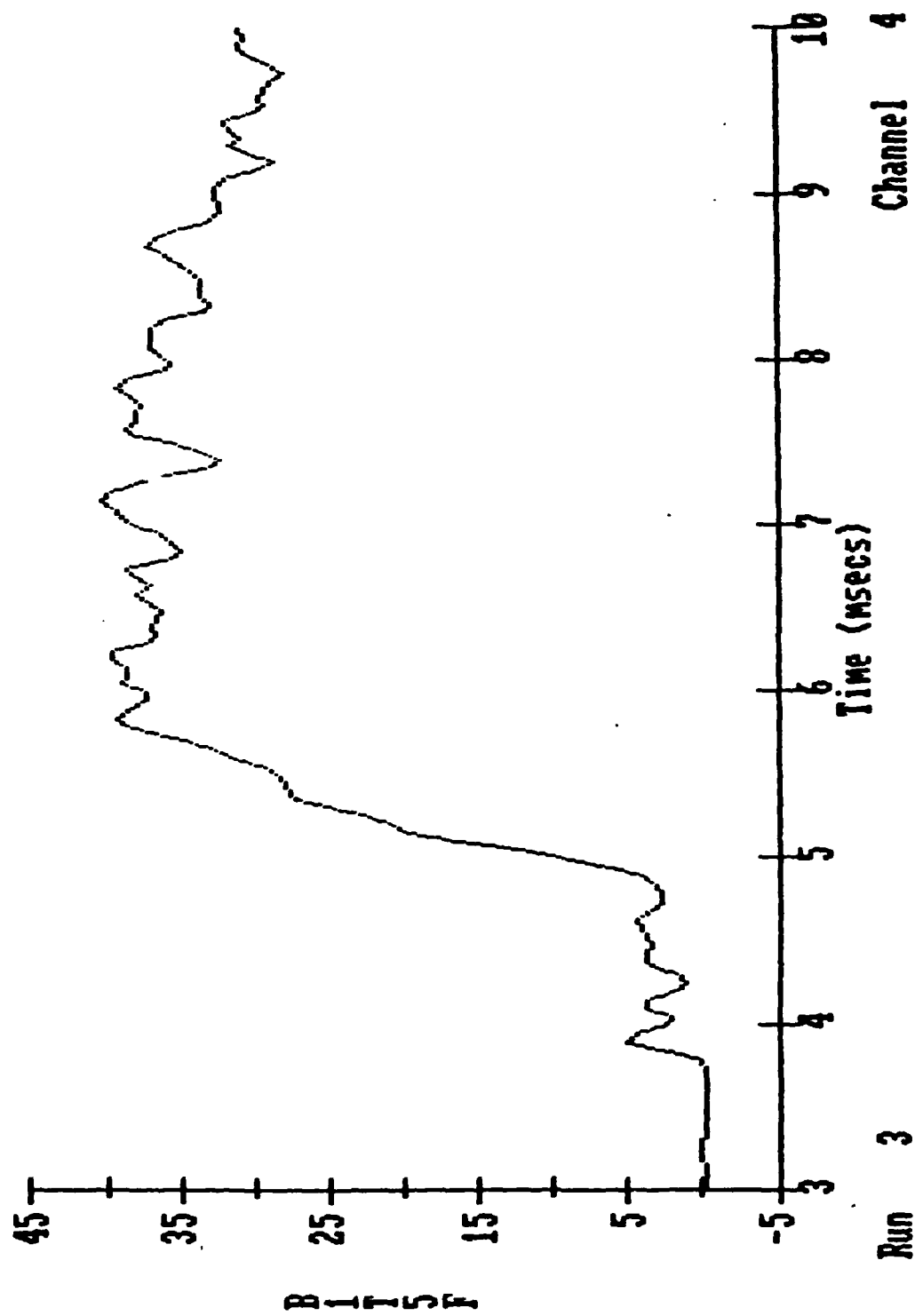
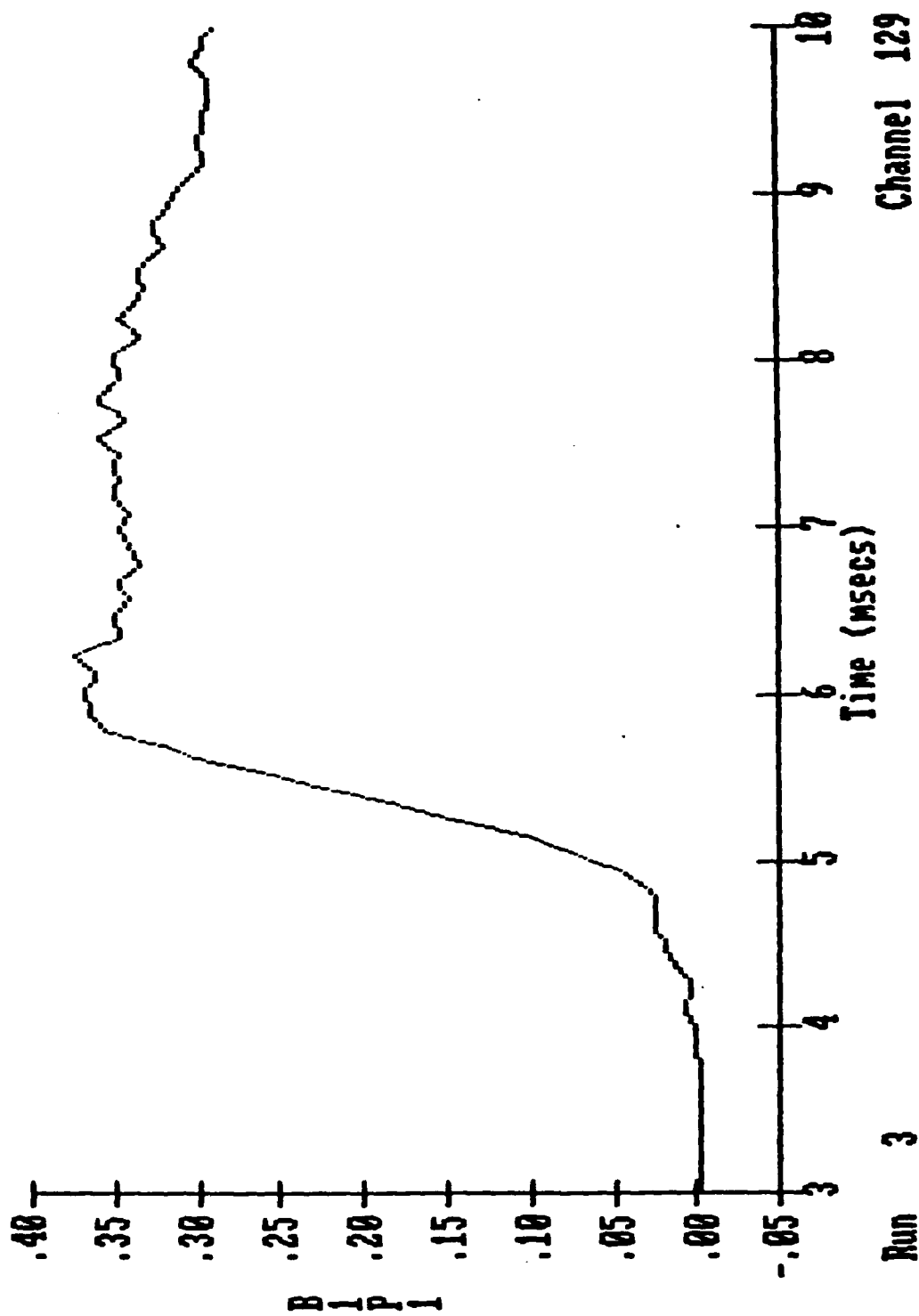Figure 54 HEAT TRANSFER TIME HISTORY FROM THIN FILM INSTRUMENTATION

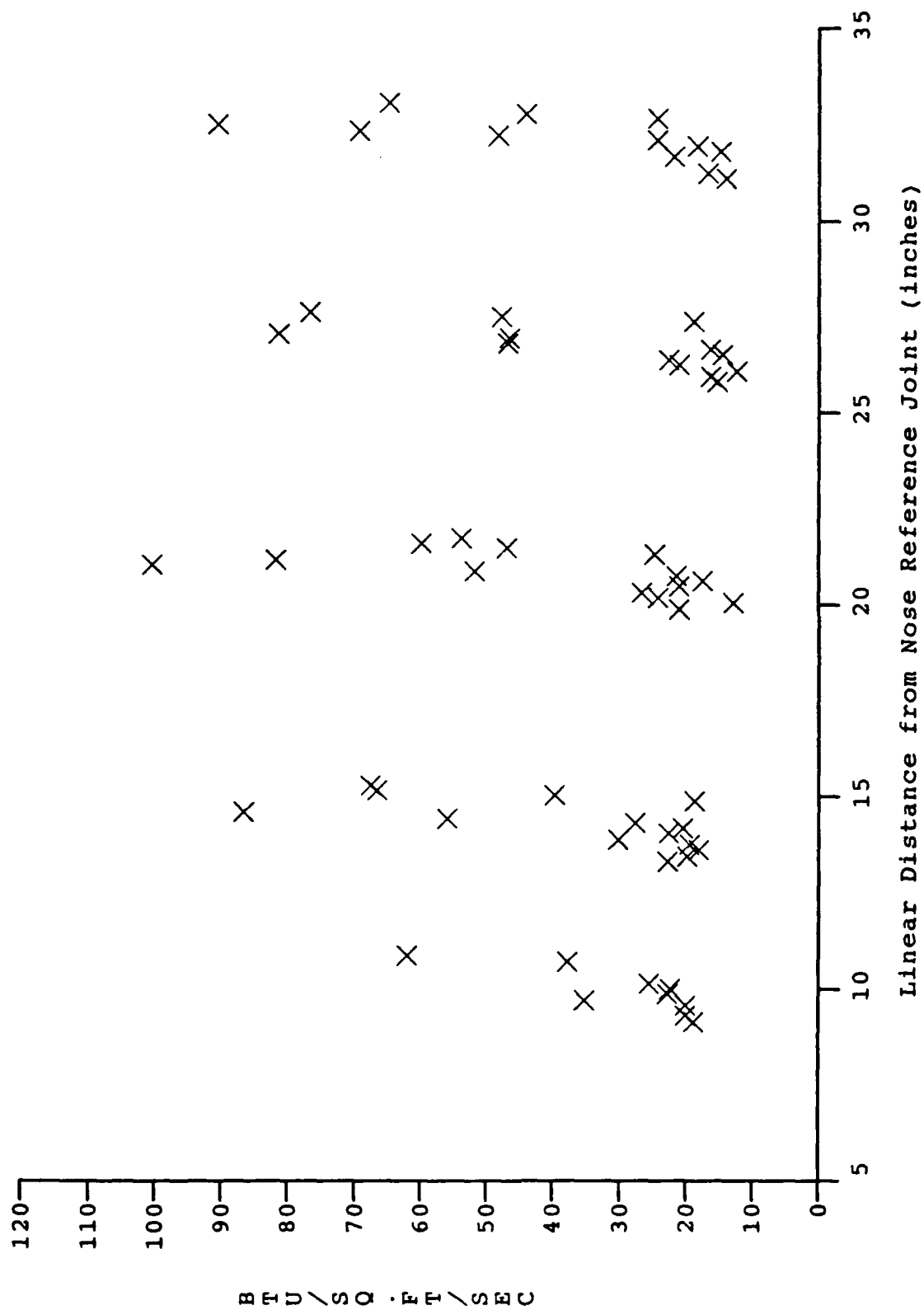Figure 55 TIME HISTORY TRACE FROM PRESSURE GAGE IN CONE

85

Figure 56a. Distribution of Heating Along Model Surface
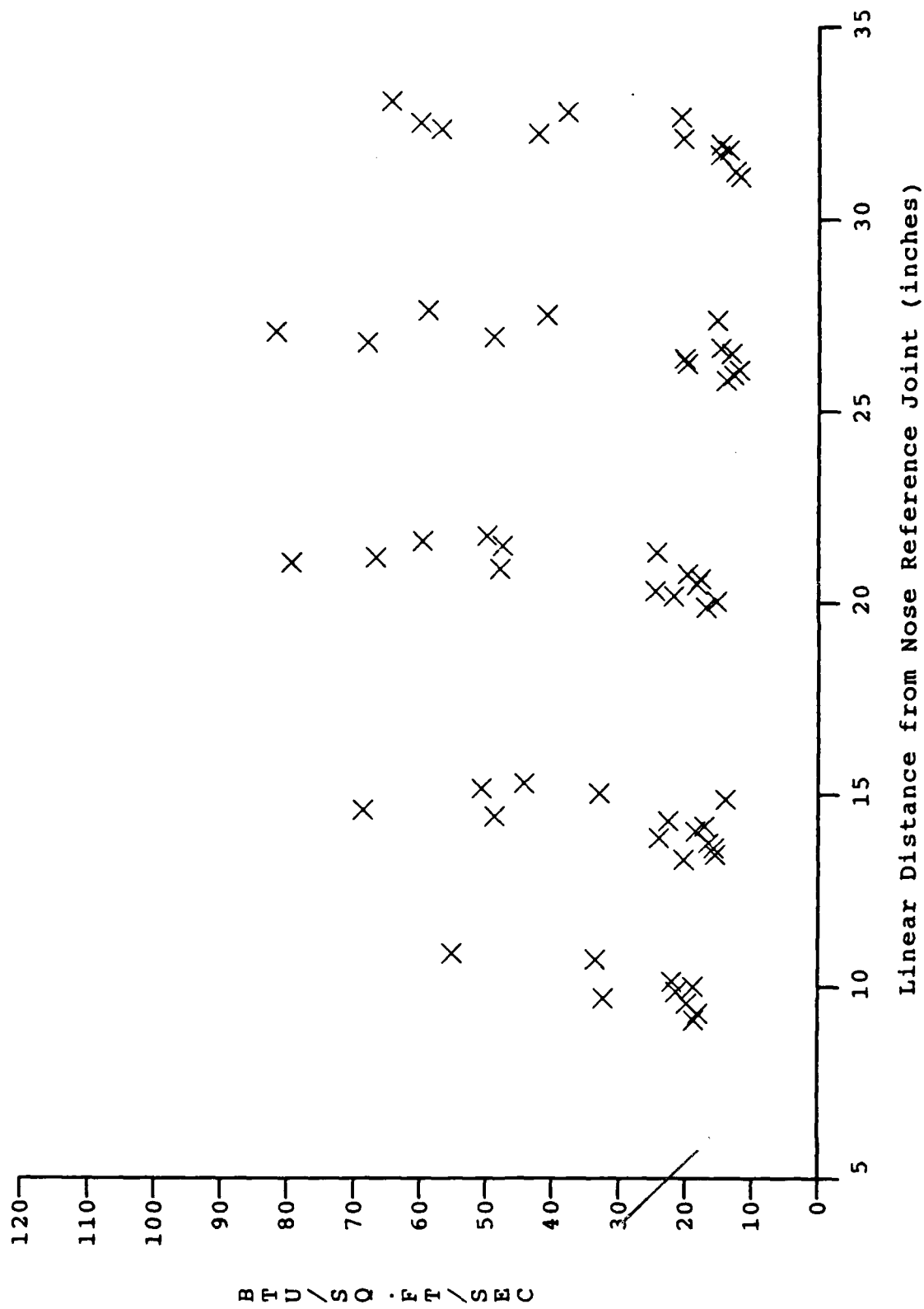[Run # 34, B'=0.231, M=11, Re/ft=1.0X10^7]

Figure 56b. Distribution of Heating Along Model Surface
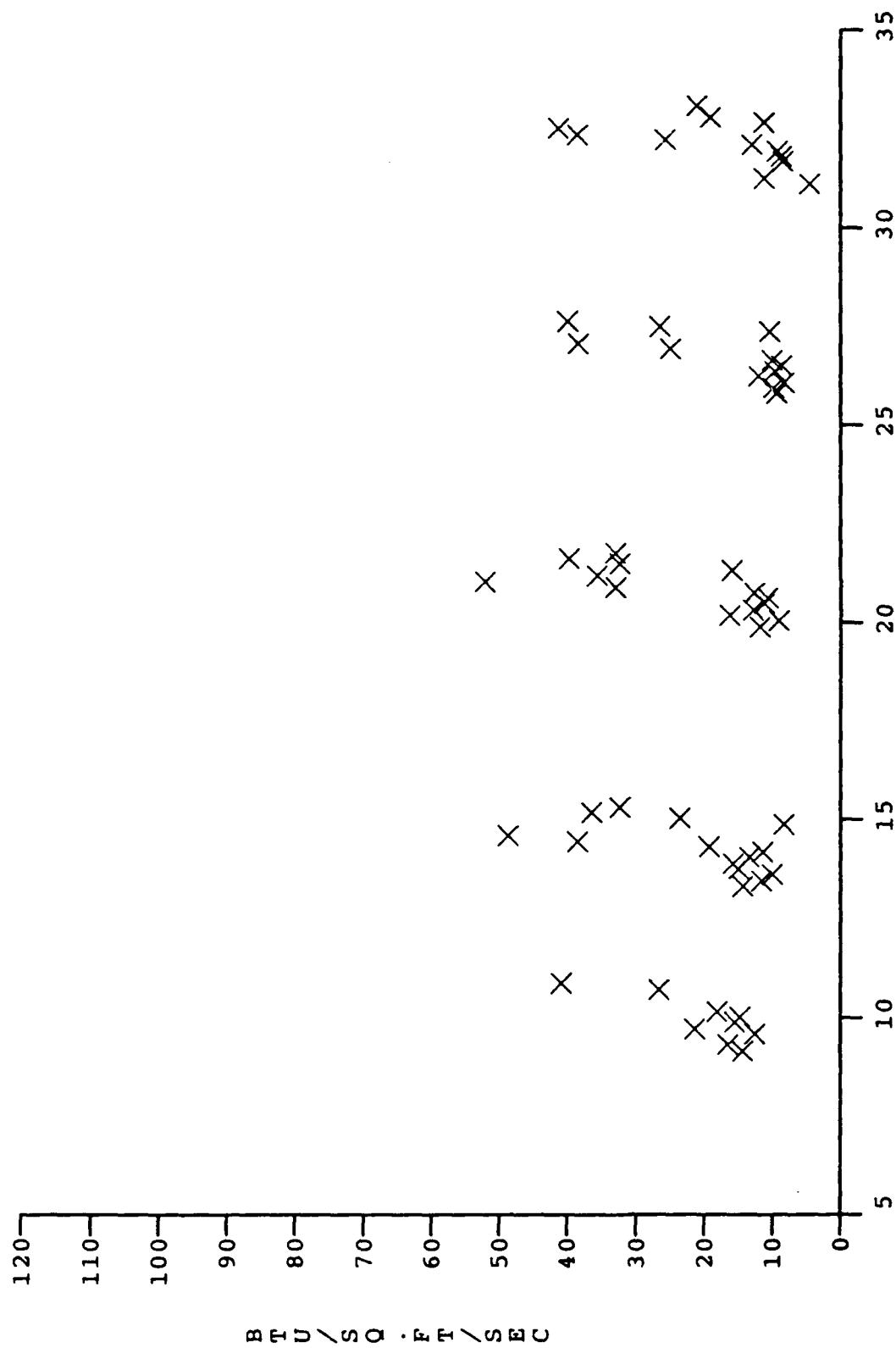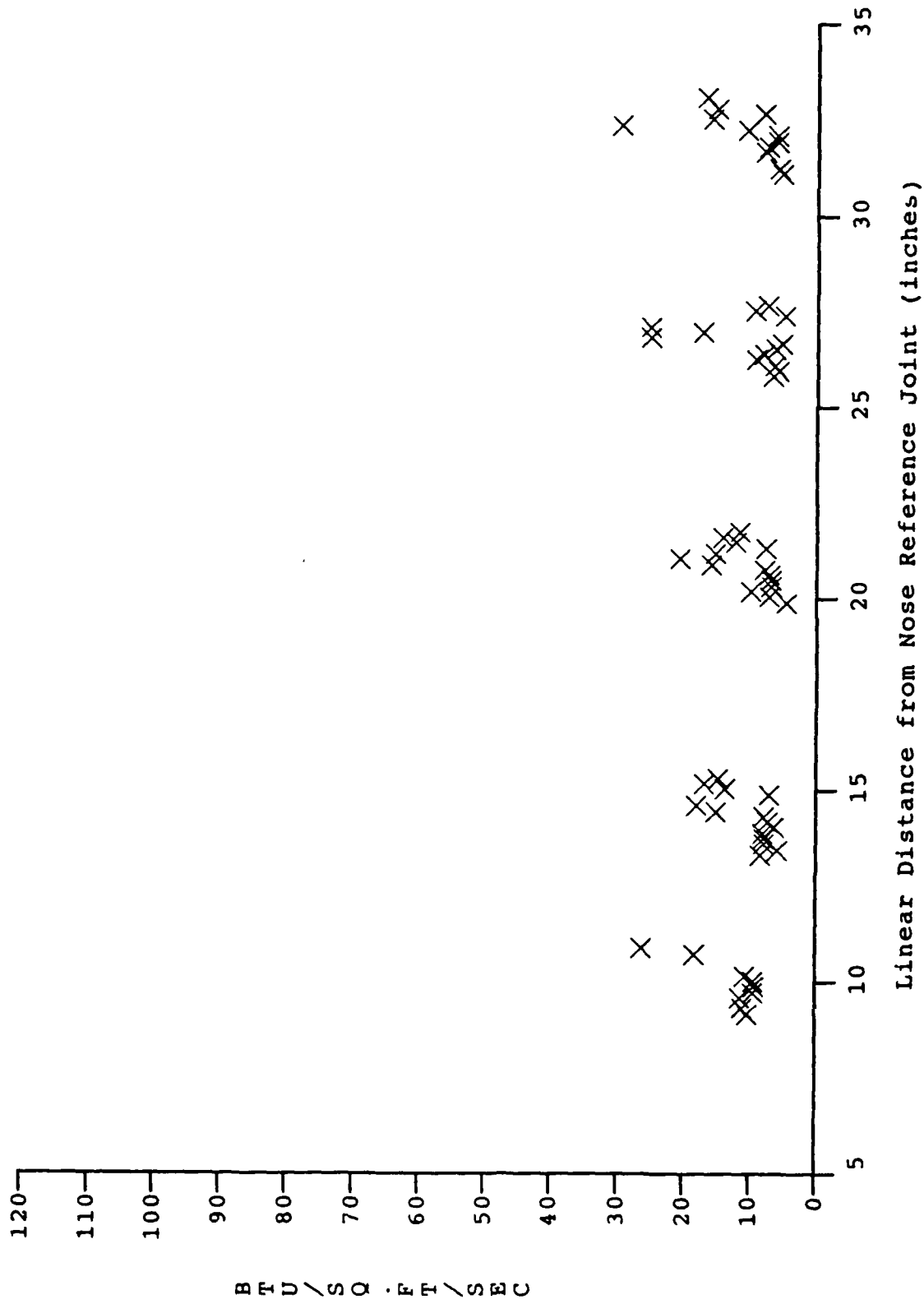[Run# 33, B'=0.705, M=11, Re/ft=1.0x10^7]

Linear Distance from Nose Reference Joint (inches)

B
T
U
/
S
Q
.
F
T
/
S
E
C

87

Figure 56c. Distribution of Heating Along Model Surface
[Run# 32, B'=1.751, M=11, Re/ft=1.0X10^7]

Linear Distance from Nose Reference Joint (inches)

BTU/SQ.FT/SEC

Figure 56d. Distribution of Heating Along Model Surface
[Run# 35, B'=4.083, M=11, Re/ft=1.0X10^7]

89

Measurements similar to those described above are shown for the Mach 13 condition in Figure 57 a-f, and those for the Mach 15 condition are shown in Figure 58 a-c. We again see that the peak/base heating levels are between 3 and 10 depending upon the blowing rates.

The distribution of heating rate over the roughness elements for a range of low blowing rates plotted as a fraction of maximum heating rate is shown in Figure 59a. Here we see that for the lower blowing rates the shape of the distribution becomes more rounded with increasing blowing. At the larger blowing rates shown in Figure 59b, the peak heating is now only three times the base value compared with factors of up to ten times for the weakly blowing case.

The variation of peak heat transfer measured on the roughness elements along the cone for a range of blowing rates for the Mach 11 and 13 conditions are shown in Figures 60a and 60b. Similar distributions are shown for heating levels on the floor between the roughness elements and injectors in Figure 61a and 61b. Measurements from the calorimeter gages plotted in this format are shown in Figure 62a and 62b. Clearly the peak heating levels show a larger variation with lambda than those at the base of the roughness elements.

The measurements of heating to the model, normalized by the value for negligiable blowing rate, are plotted versus blowing parameter in Figures 63a, 63b, 64a, 64b, 65a and 65b. We observe a rapid decrease in the heat transfer rates with blowing rates for low values of the blowing parameter, and for blowing parameters above 3 there is little decrease in heat transfer with increased blowing.

One of the unique features of this study is that both skin friction and heat transfer measurements were obtained simultaneously for each of the blowing rates and free stream conditions. Thus, we can provide an analogous set of skin friction plots to those presented above for heat transfer. The variations in skin friction along the cone for a range of blowing rates are shown in Figures 66a and 66b for Mach 11, 13, respectively. These measurements are non-dimensionalized by the zero blowing value and re-plotted to show the variation of skin friction with blowing rate parameters in Figure 67. Again, following a rapid decrease in skin friction with a mass addition rate above B' of 1, there is little decrease in skin friction with increased blowing. We speculate that for blowing rates of B' over 2.0, the boundary layer beings to lift from
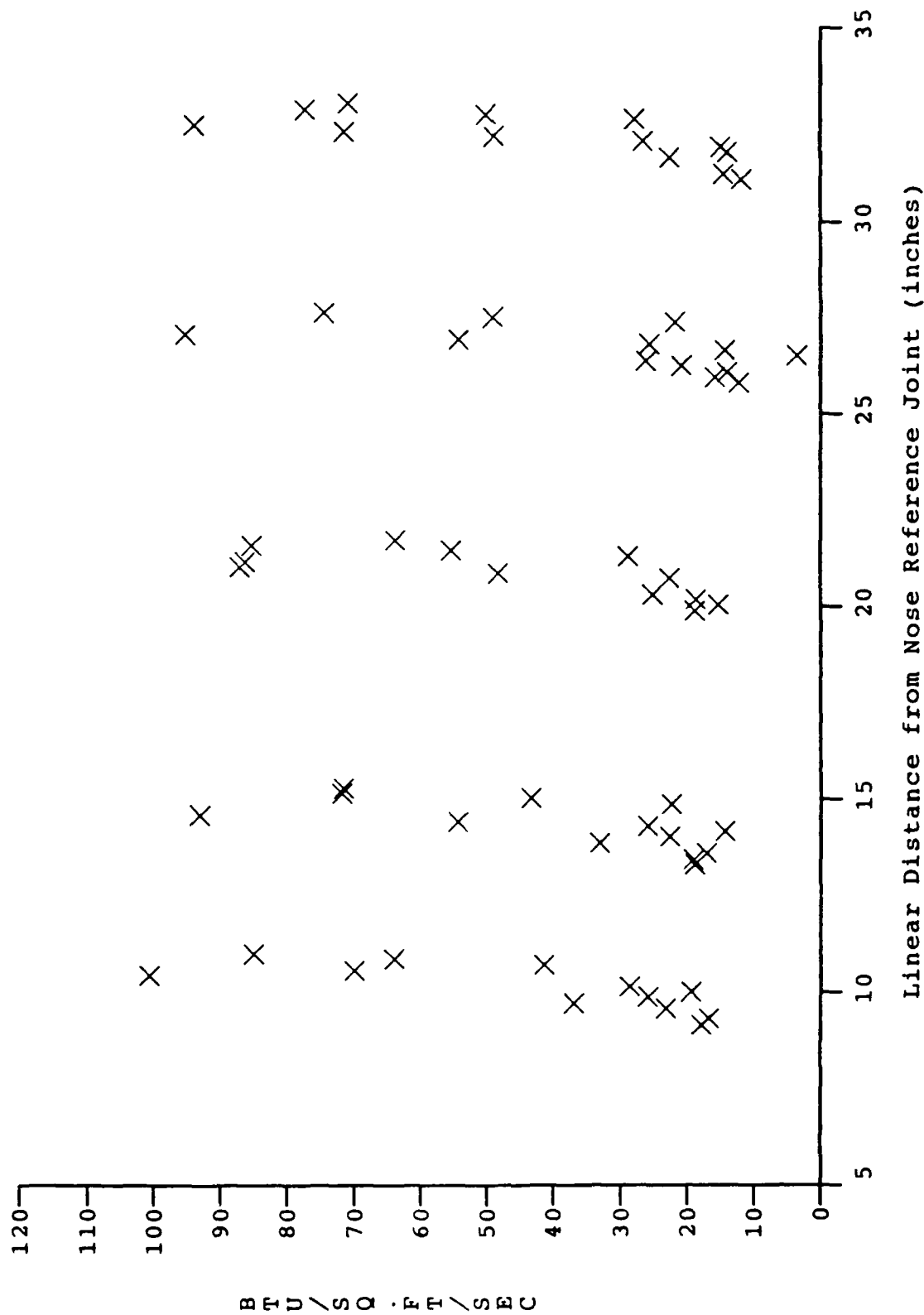
90

Figure 57a. Distribution of Heating Along Model Surface
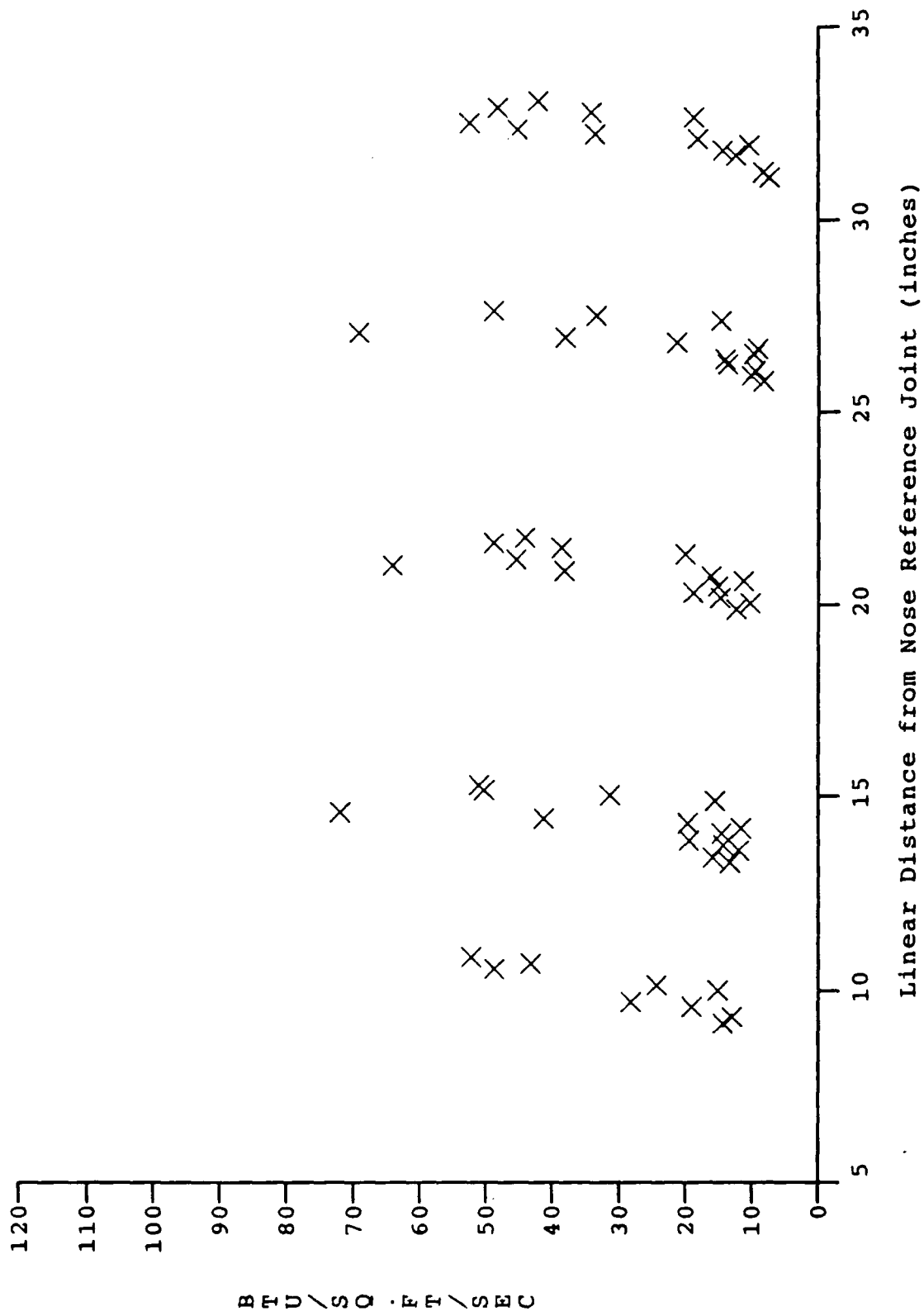[Run# 3, B'=0.000, M=13, Re/ft=5.0X10^6]

91

Figure 57b. Distribution of Heating Along Model Surface
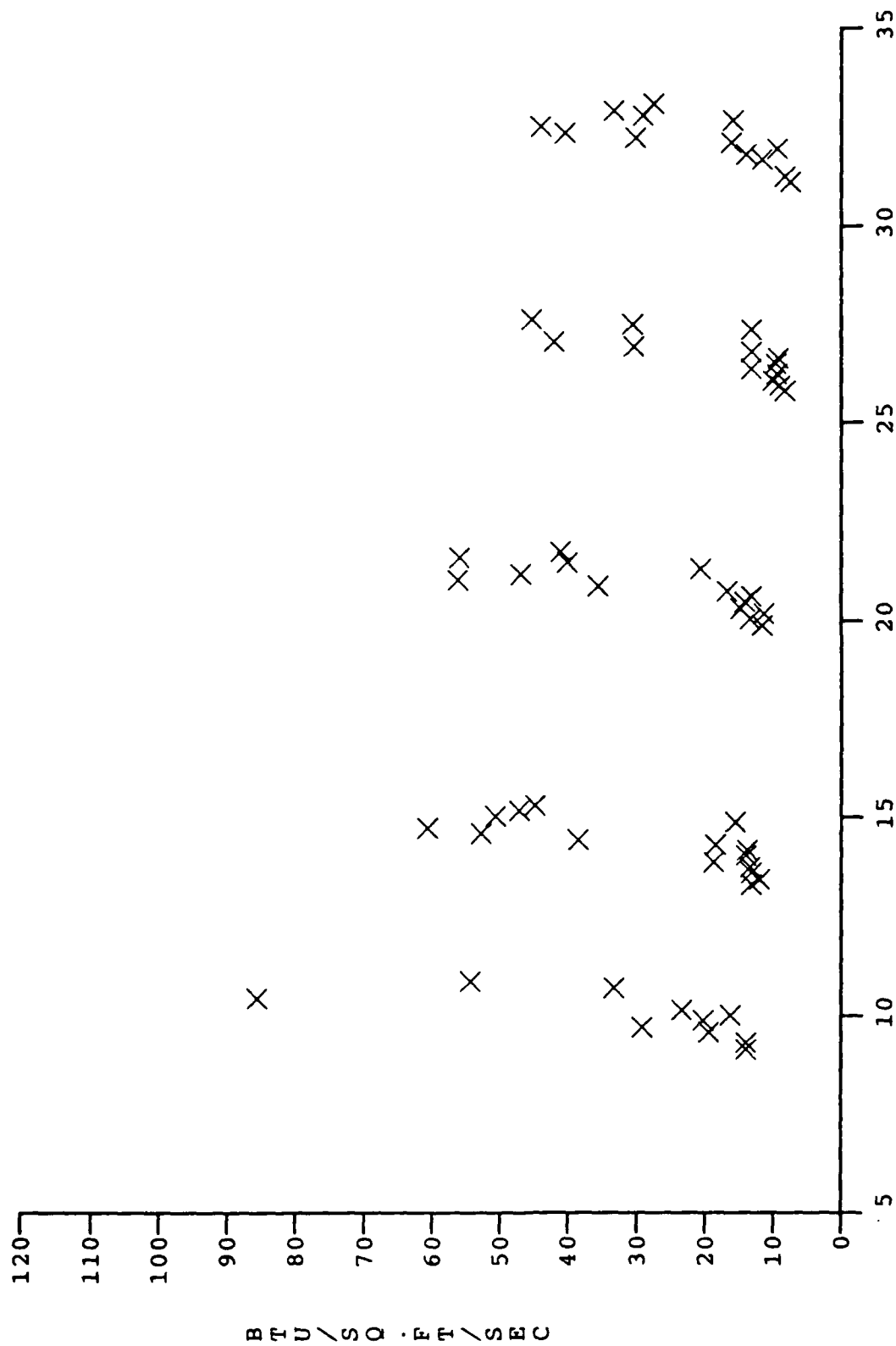[Run# 9, B'=0.366, M=13, Re/ft=5.0X10^6]

92

Figure 57c. Distribution of Heating Along Model Surface
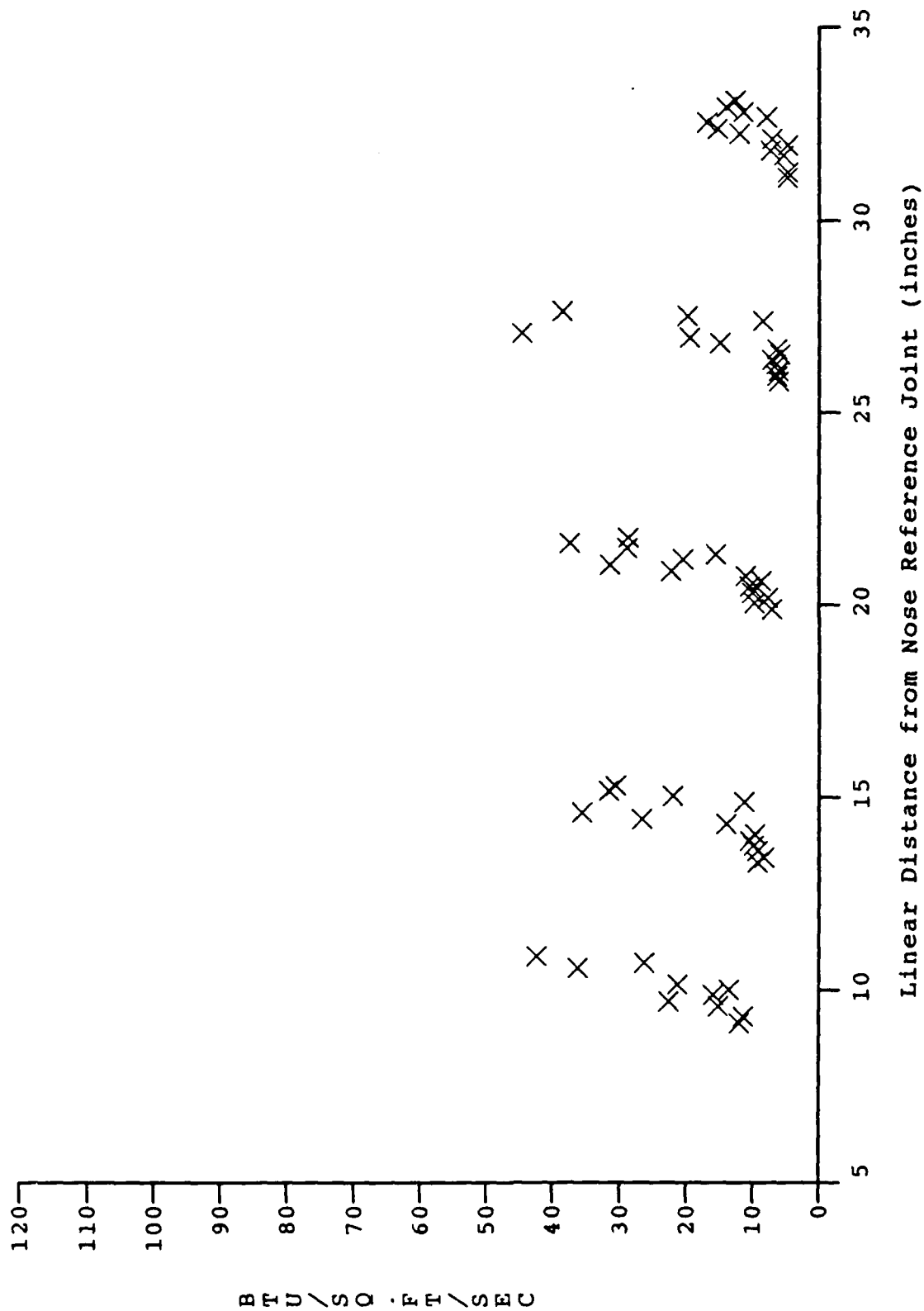[Run# 4, B'=0.639, M=13, Re/ft=5.0X10^6]

93

Figure 57d. Distribution of Heating Along Model Surface
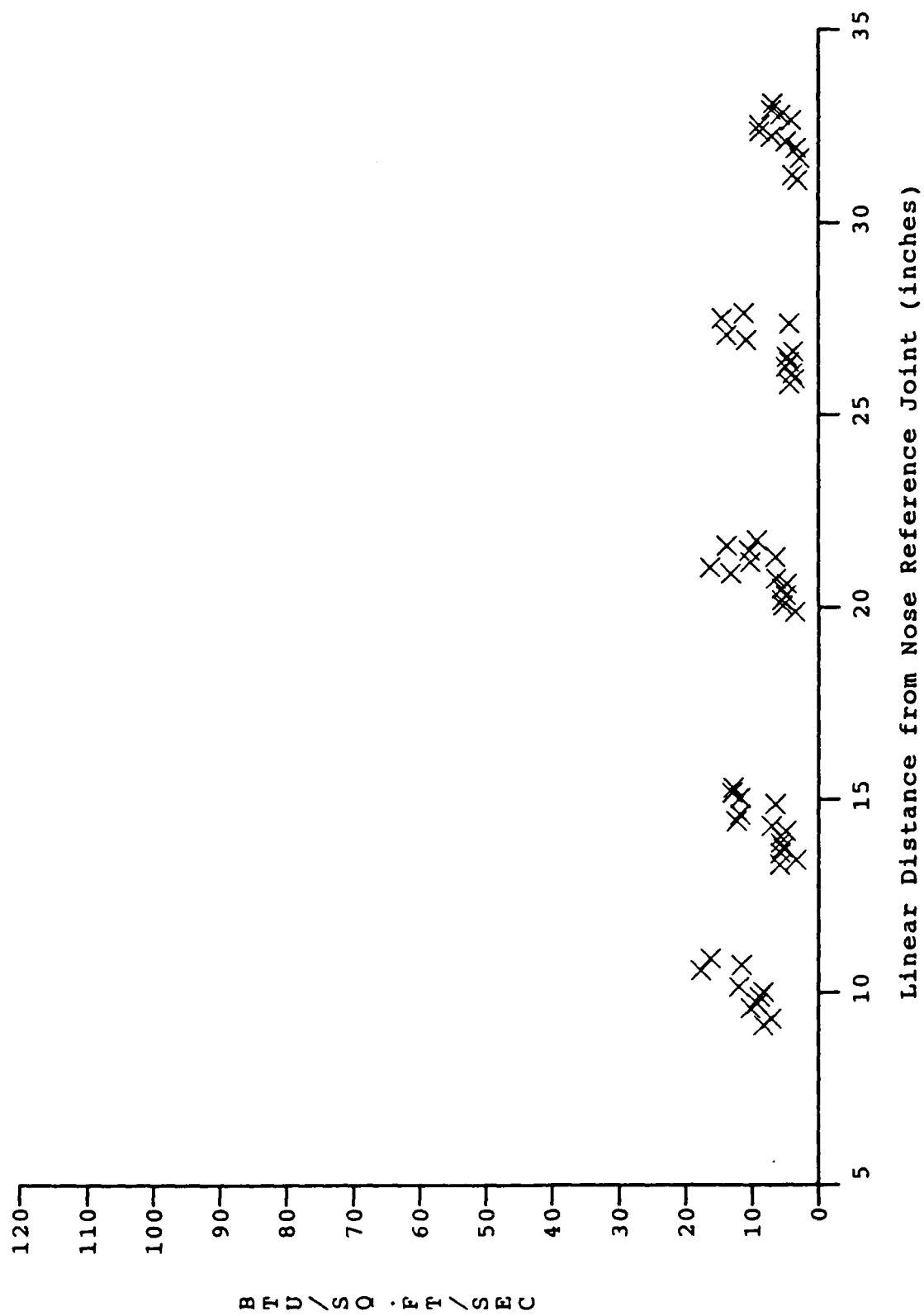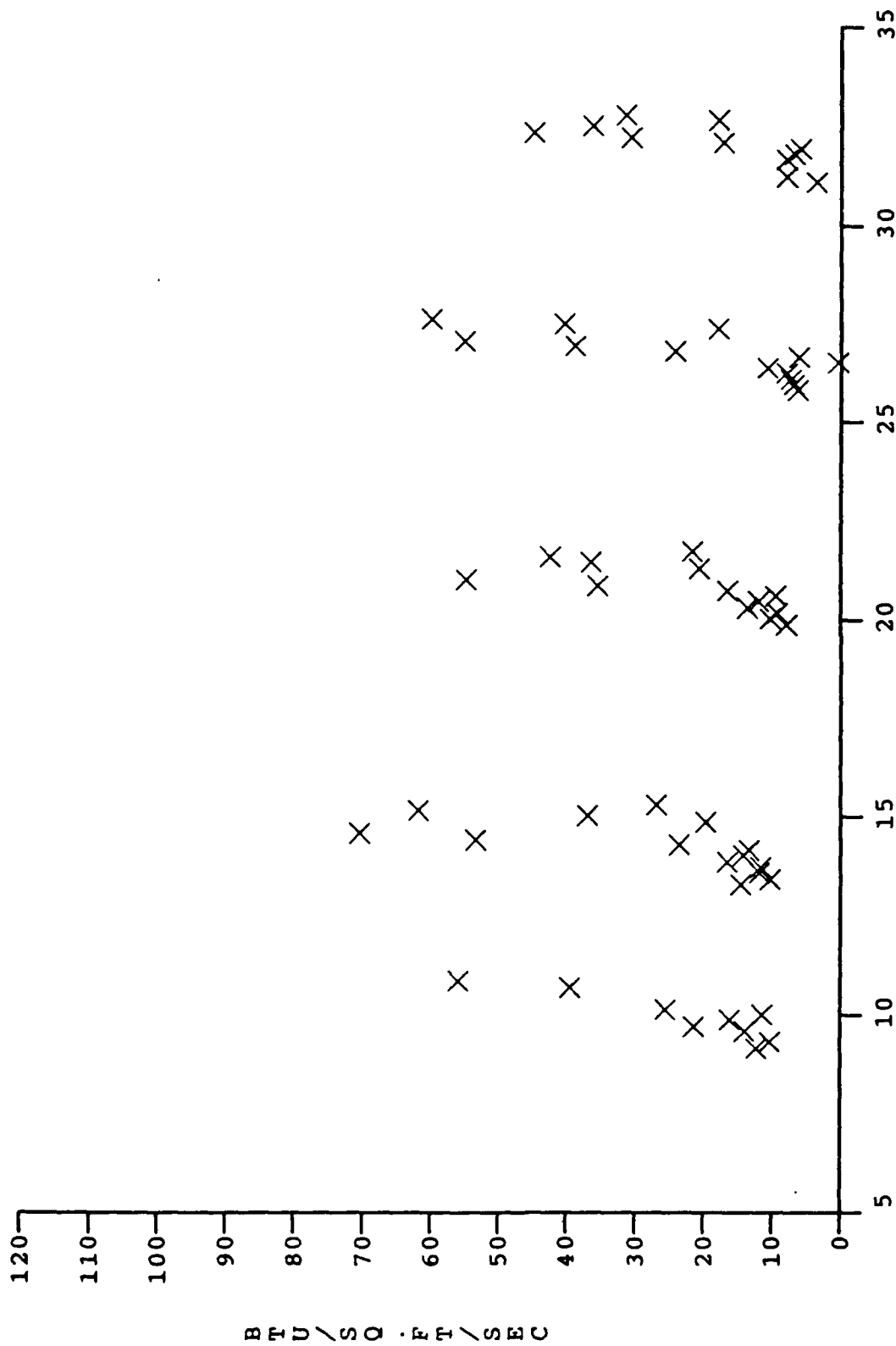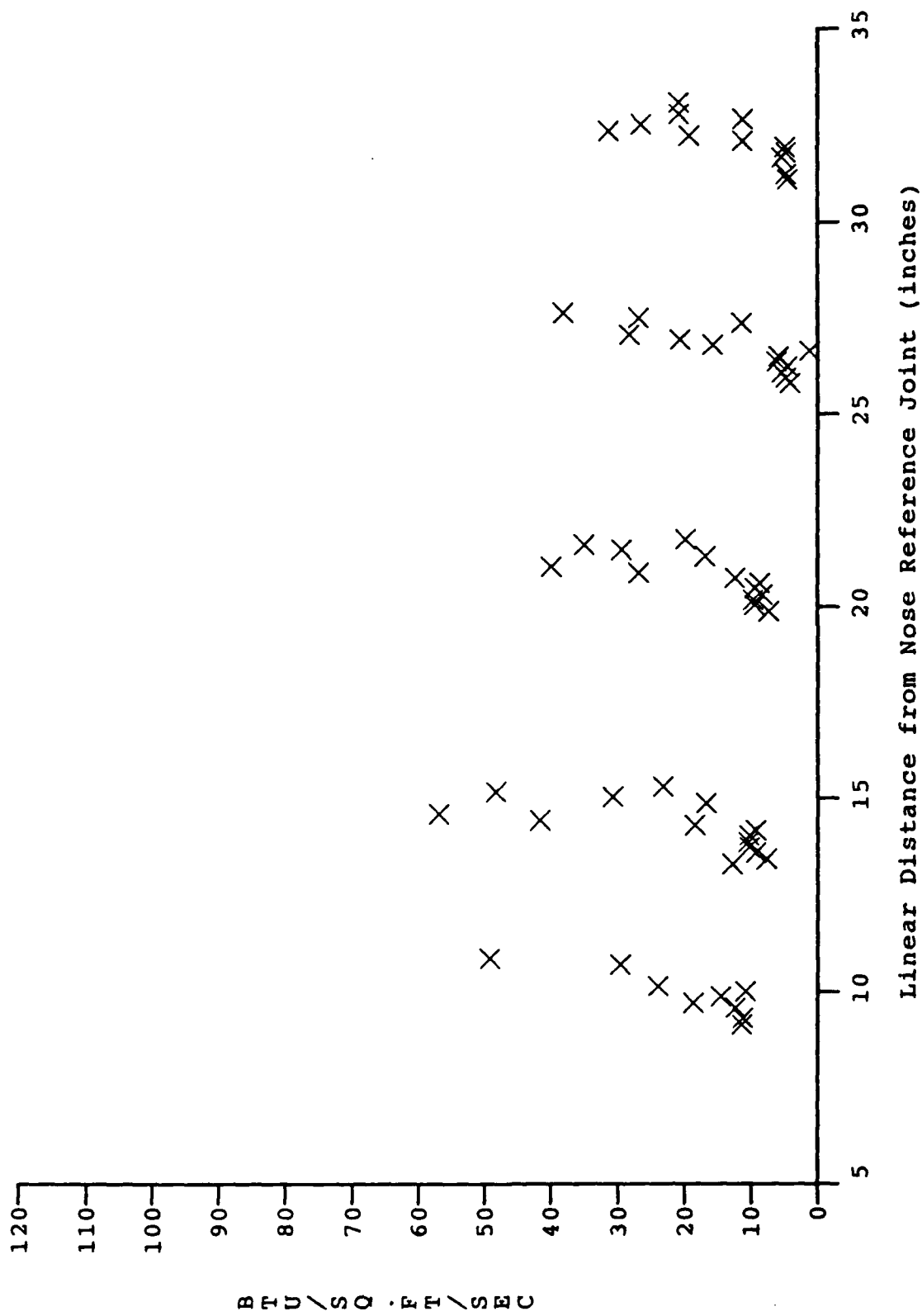[Run# 6, B'=1.259, M=13, Re/ft=5.0X10^6]

Figure 57e. Distribution of Heating Along Model Surface
[Run# 15, B'=2.111, M=13, Re/ft=5.0x10^6]

Figure 57f. Distribution of Heating Along Model Surface
[Run# 7, B'=3.086, M=13, Re/ft=5.0x10^6]

Linear Distance from Nose Reference Joint (inches)

BTU/SQ.FT/SEC

96

Figure 58a. Distribution of Heating Along Model Surface
[Run# 40, B'=0.398, M=15, Re/ft=1.5X10^6]

97

Figure 58b. Distribution of Heating Along Model Surface
[Run# 41, B'=0.560, M=15, Re/ft=1.5X10^6]
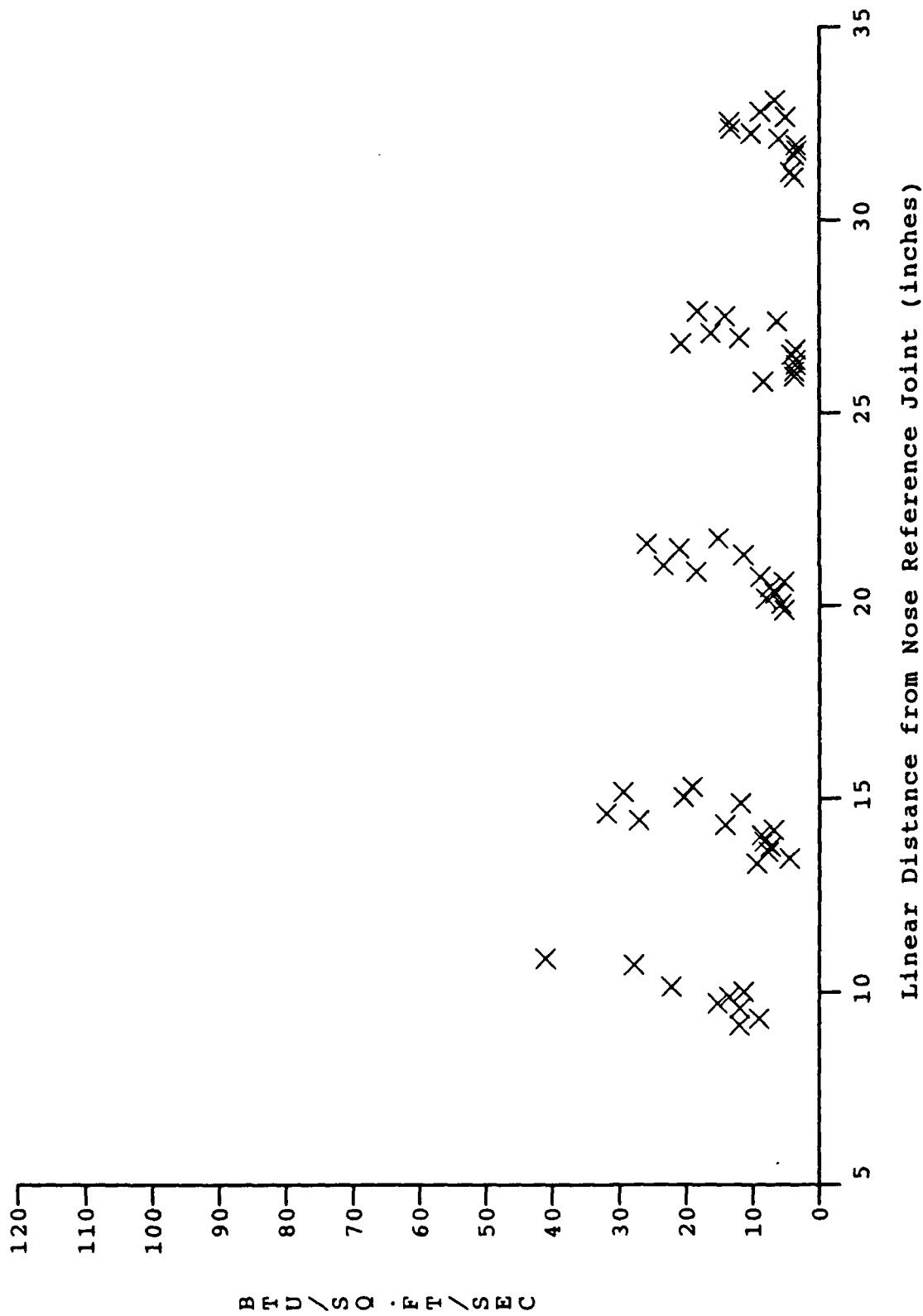
Figure 58c. Distribution of Heating Along Model Surface
[Run# 42, B'=1.329, M=15, Re/ft=1.5x10^6]

Linear Distance from Nose Reference Joint (inches)

BTU/SQ.FT/SEC

99

X zero ☐ 0.077 ◇ 0.269 ○ 0.366 ☆ 0.517 ☆ 0.543

Saddle Block 3 Gauges
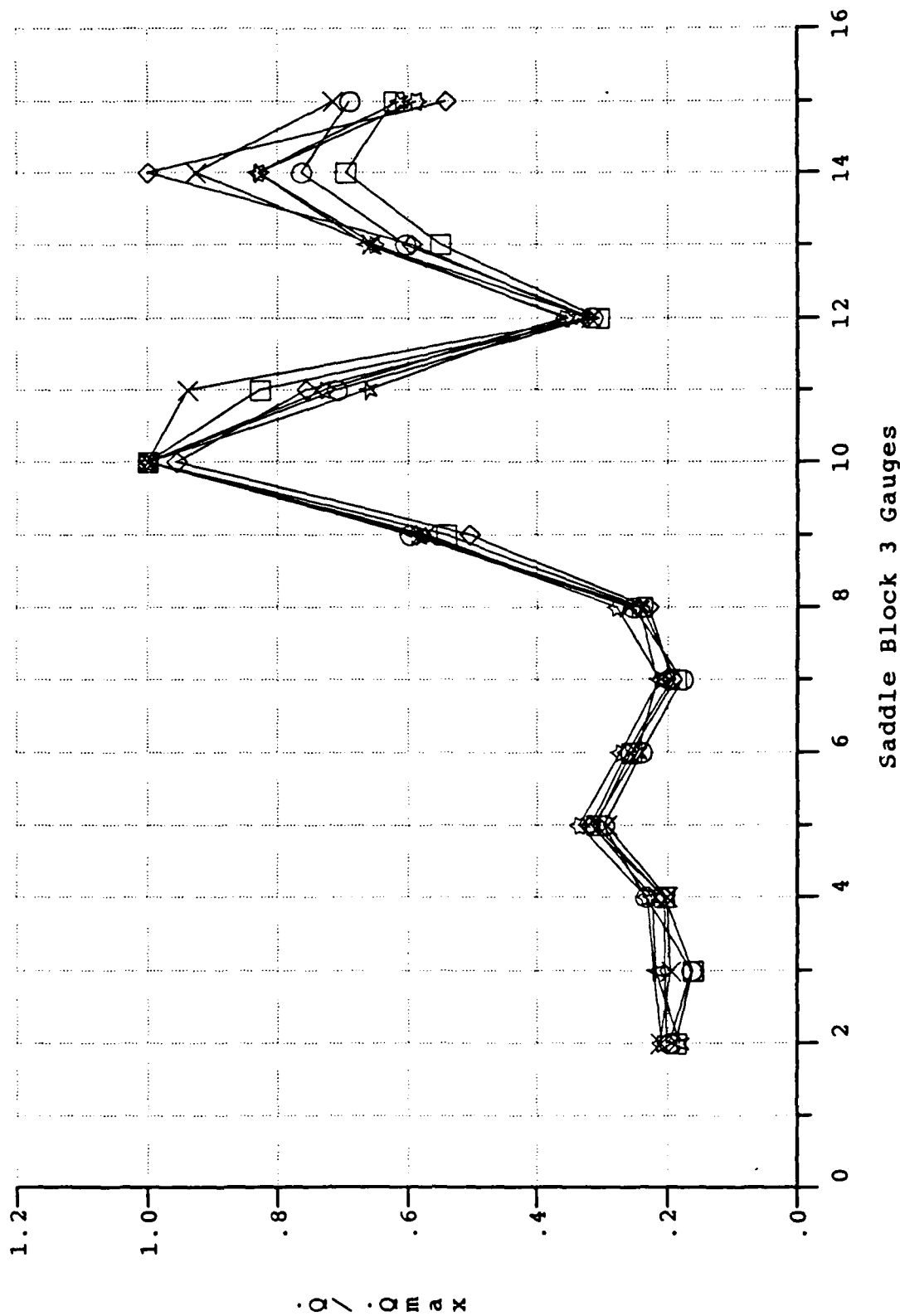
Figure 59a.   Normalized Heat Rate Distributions for Varying Blowing Rate
M = 13, Re/ft = 5X10^6, N2 Injectant, Sharp Nose

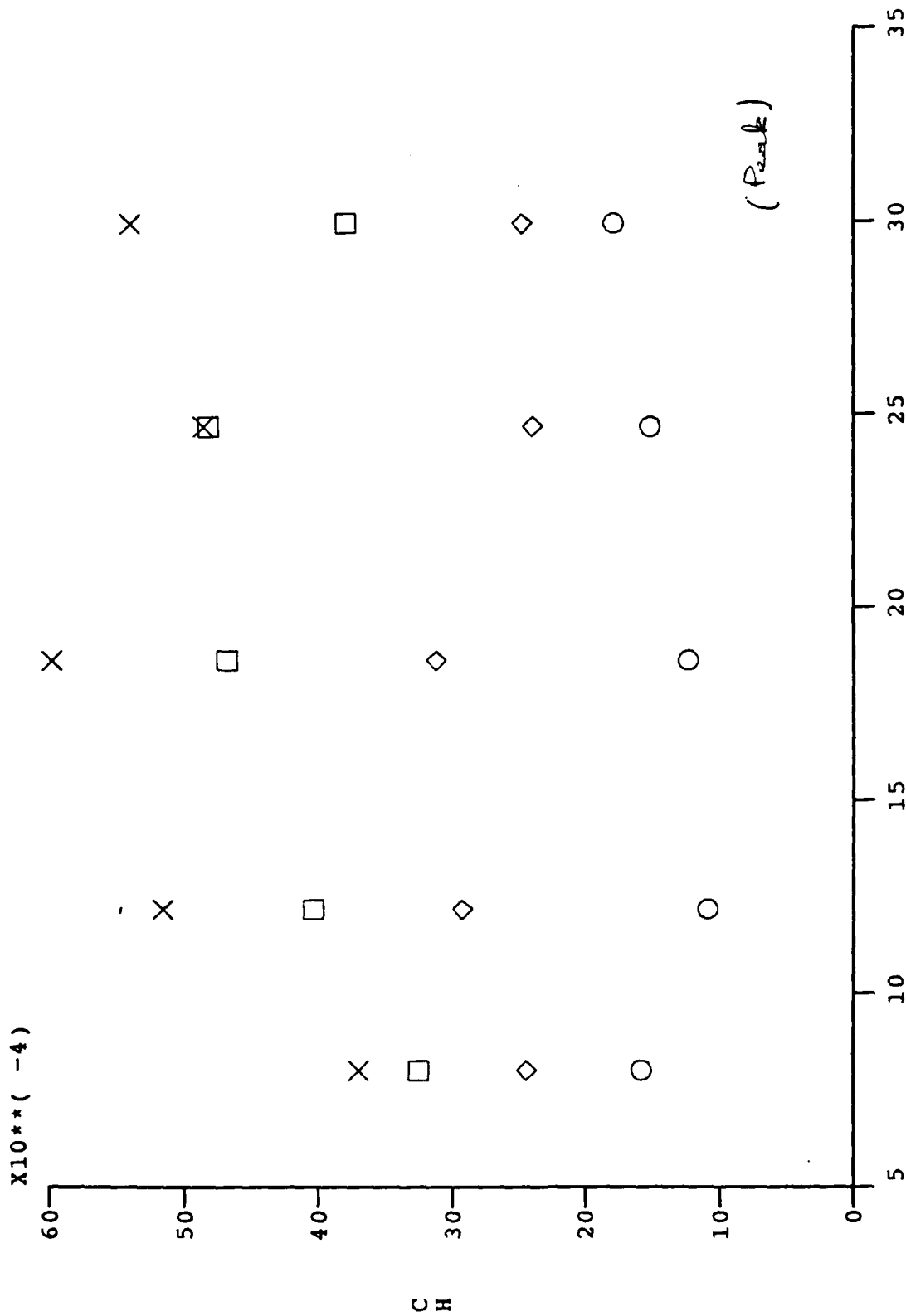Figure 59b. Normalized Heat Rate Distributions for Varying Blowing Rate
M = 13, Re/ft = 5X10^6, N2 Injectant, Sharp Nose

Figure 60a. Heating Rate on Roughness Elements Along Model for Various Blowing Rates [Mach# = 11]
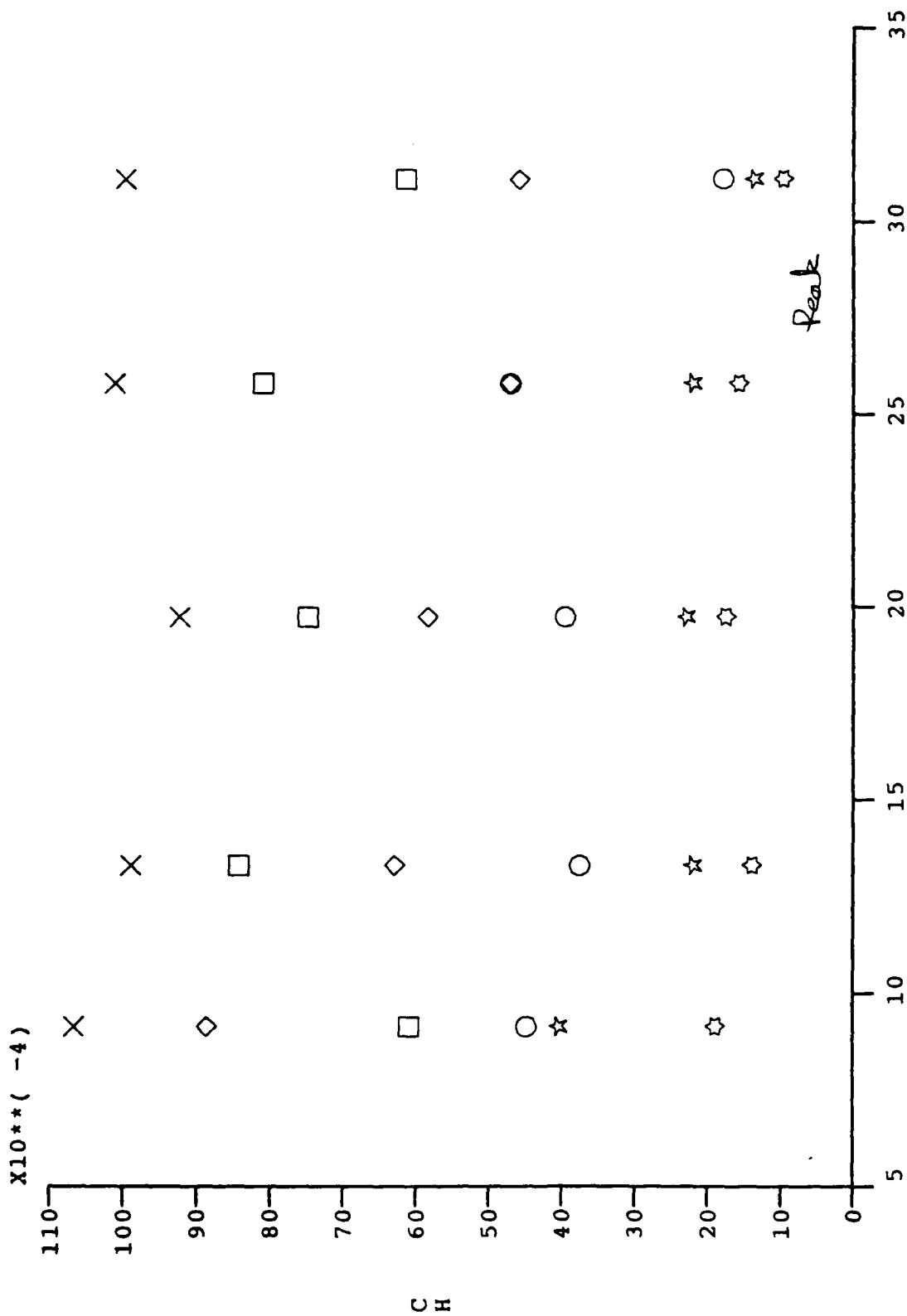
X10**(-4)

Linear Distance from Nose Reference Joint (inches)

C H

Figure 60b. Heating Rate on Roughness Elements Along Model for Various
Blowing Rates [Mach# = 13]

Peak

103

X10**(-4)
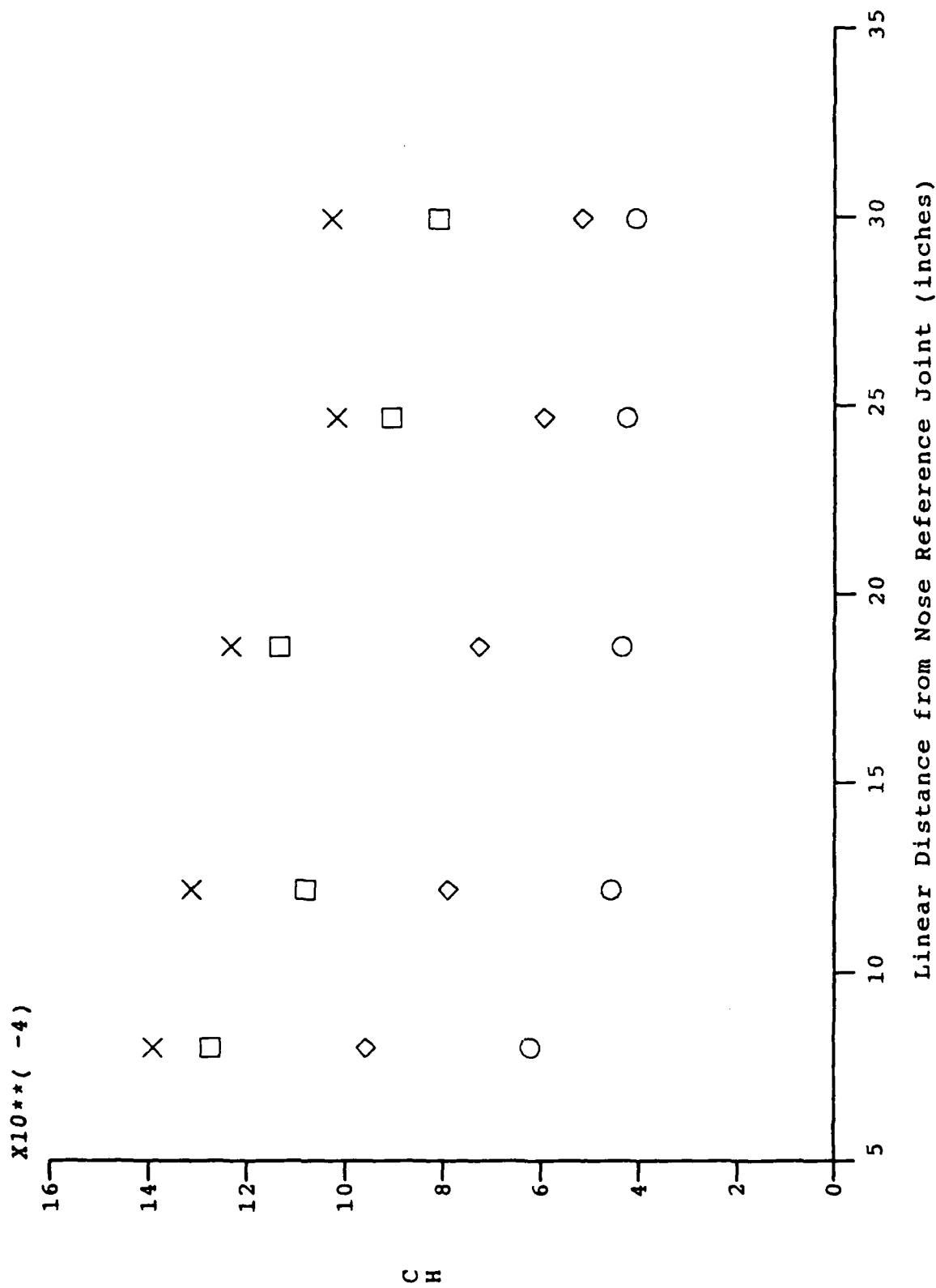
Figure 61a. Heating Rate on Base Elements Along Model for Various
Blowing Rates [Mach# = 11]
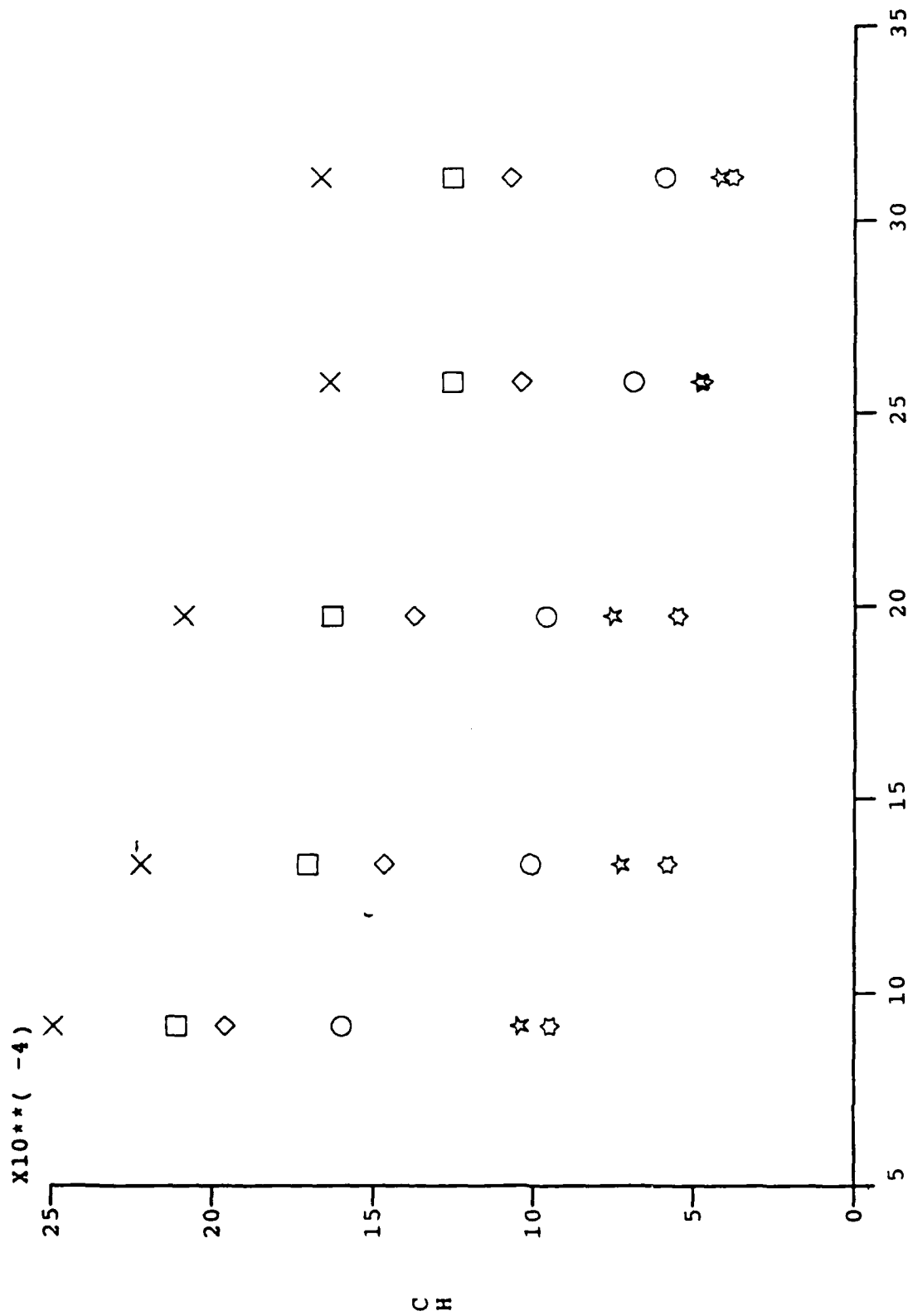
Linear Distance from Nose Reference Joint (inches)

104

Figure 61b. Heating Rate on Base Elements Along Model for Various Blowing Rates [Mach# = 13]

X10**(-4)

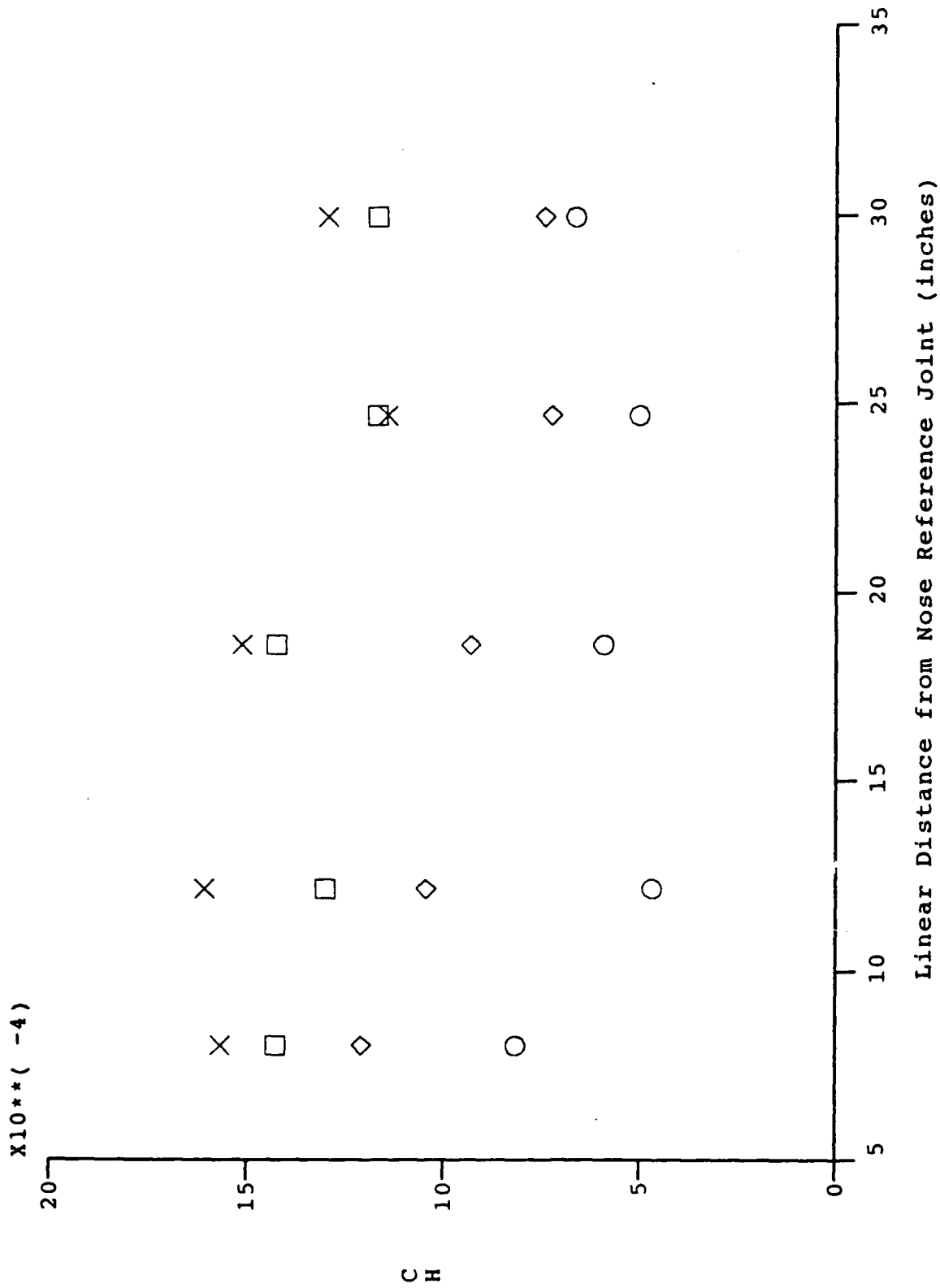Linear Distance from Nose Reference Joint (inches)

Figure 62a. Calorimeter Heating Rate Along Model for Various Blowing Rat
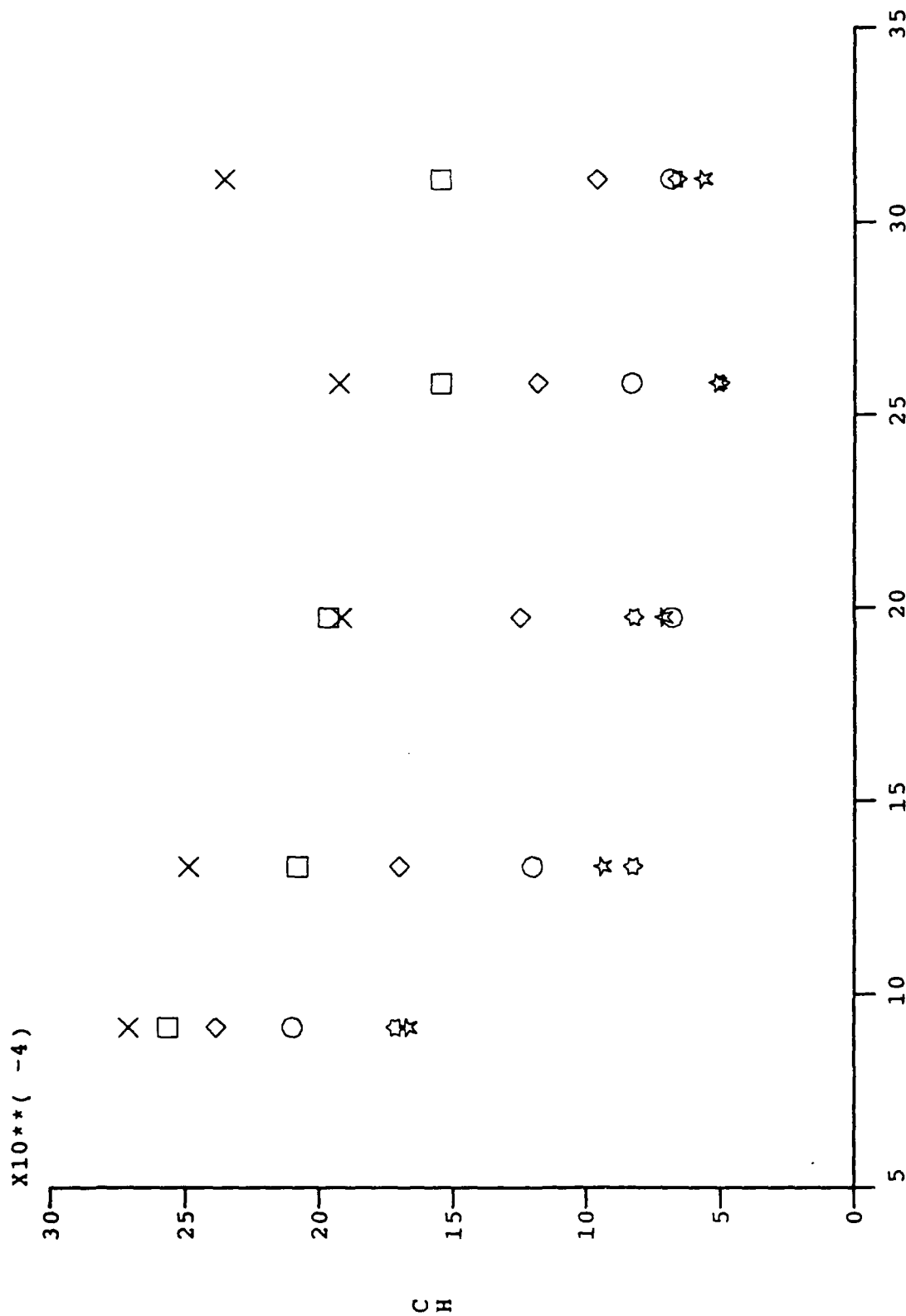[Mach# - 11]

106

Figure 62b. Calorimeter Heating Rate Along Model for Various Blowing Rat
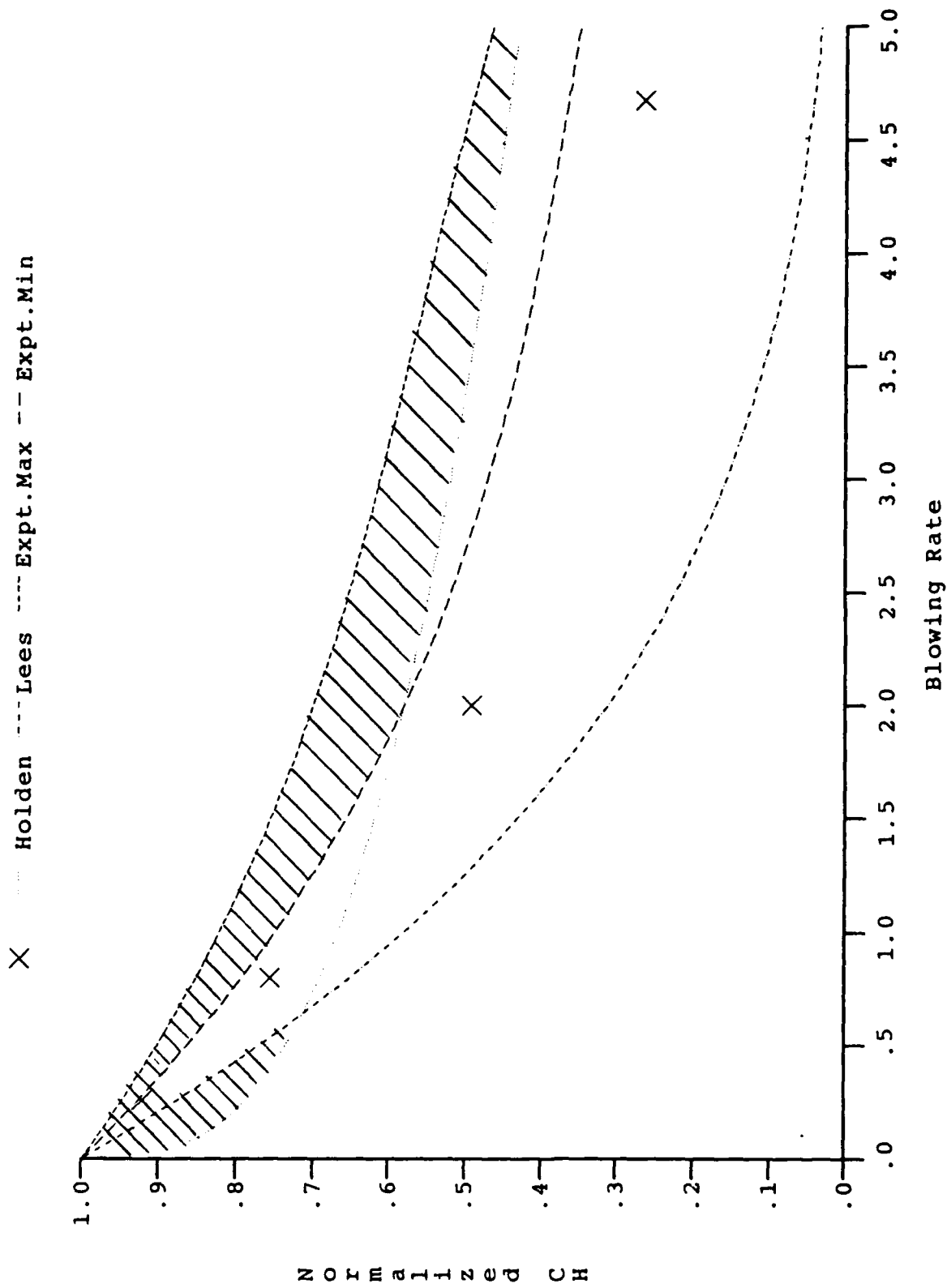[Mach# = 13]

Figure 63a. Variation of Normalized Peak Heating with Blowing Rate
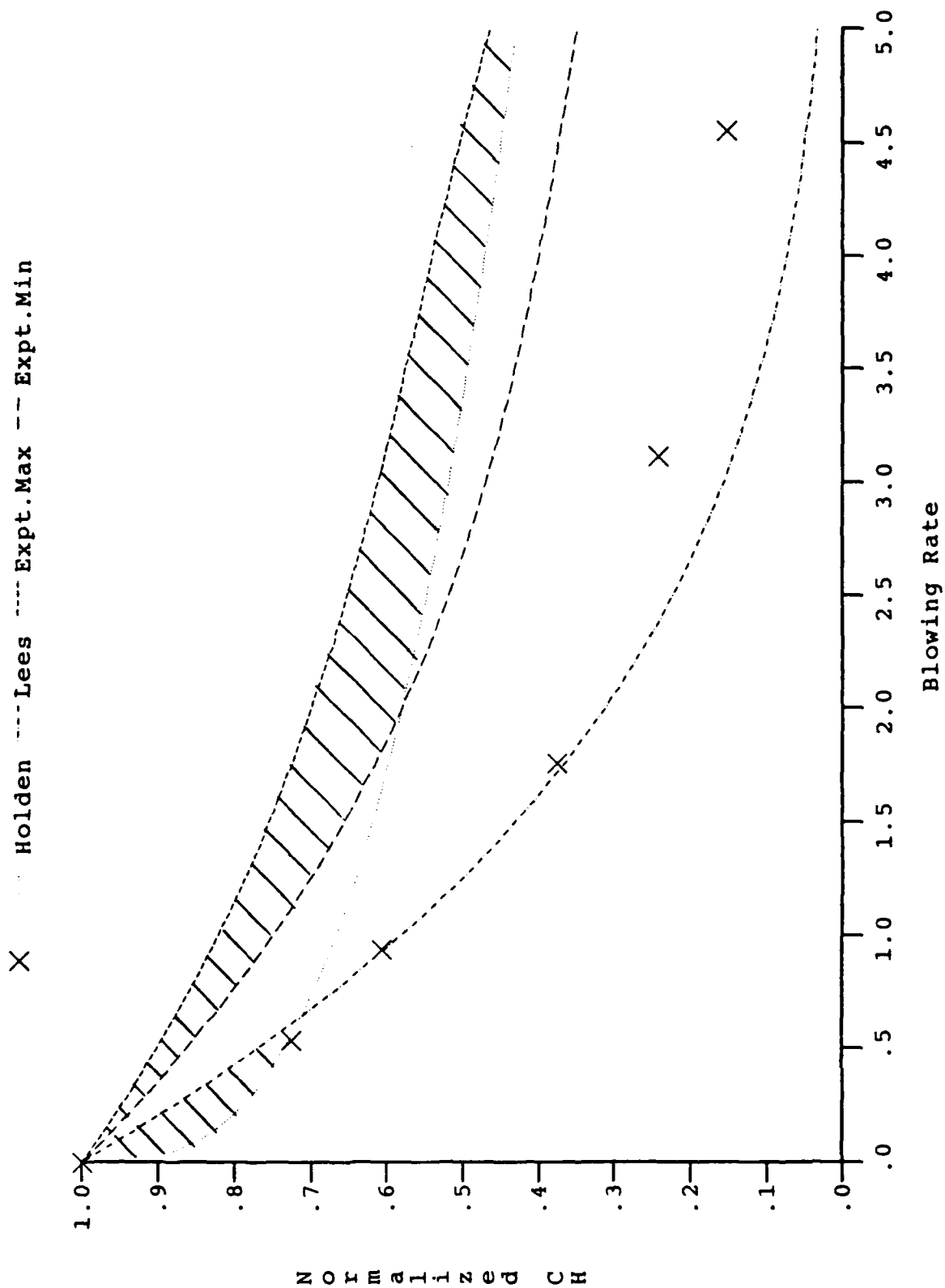Mach# = 11 (Normalized CH = CH / CHo)

Figure 63b. Variation of Normalized Peak Heating with Blowing Rate
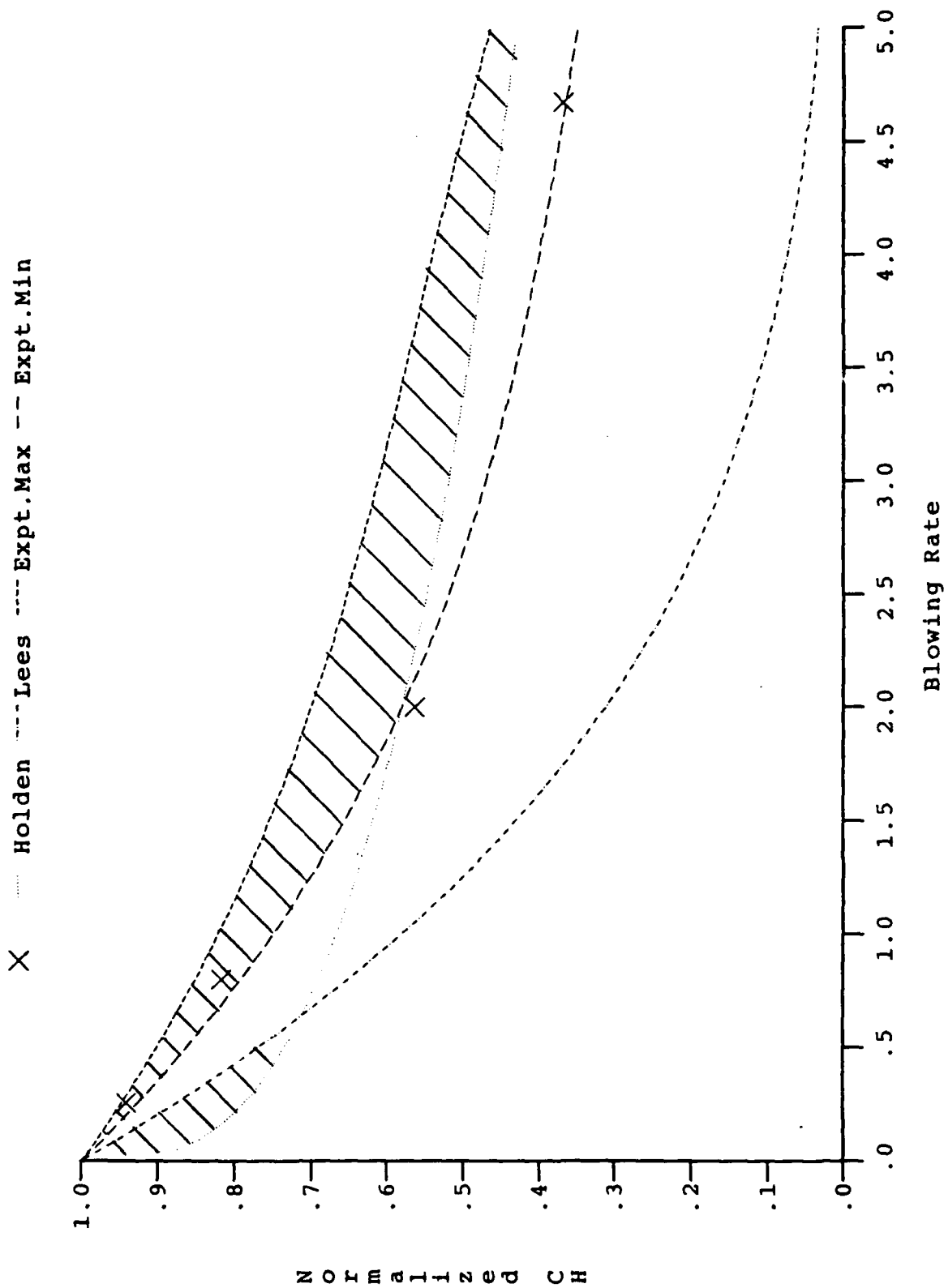Mach# = 13 (Normalized CH = CH / CHo)

Figure 64a. Variation of Normalized Base Heating with Blowing Rate
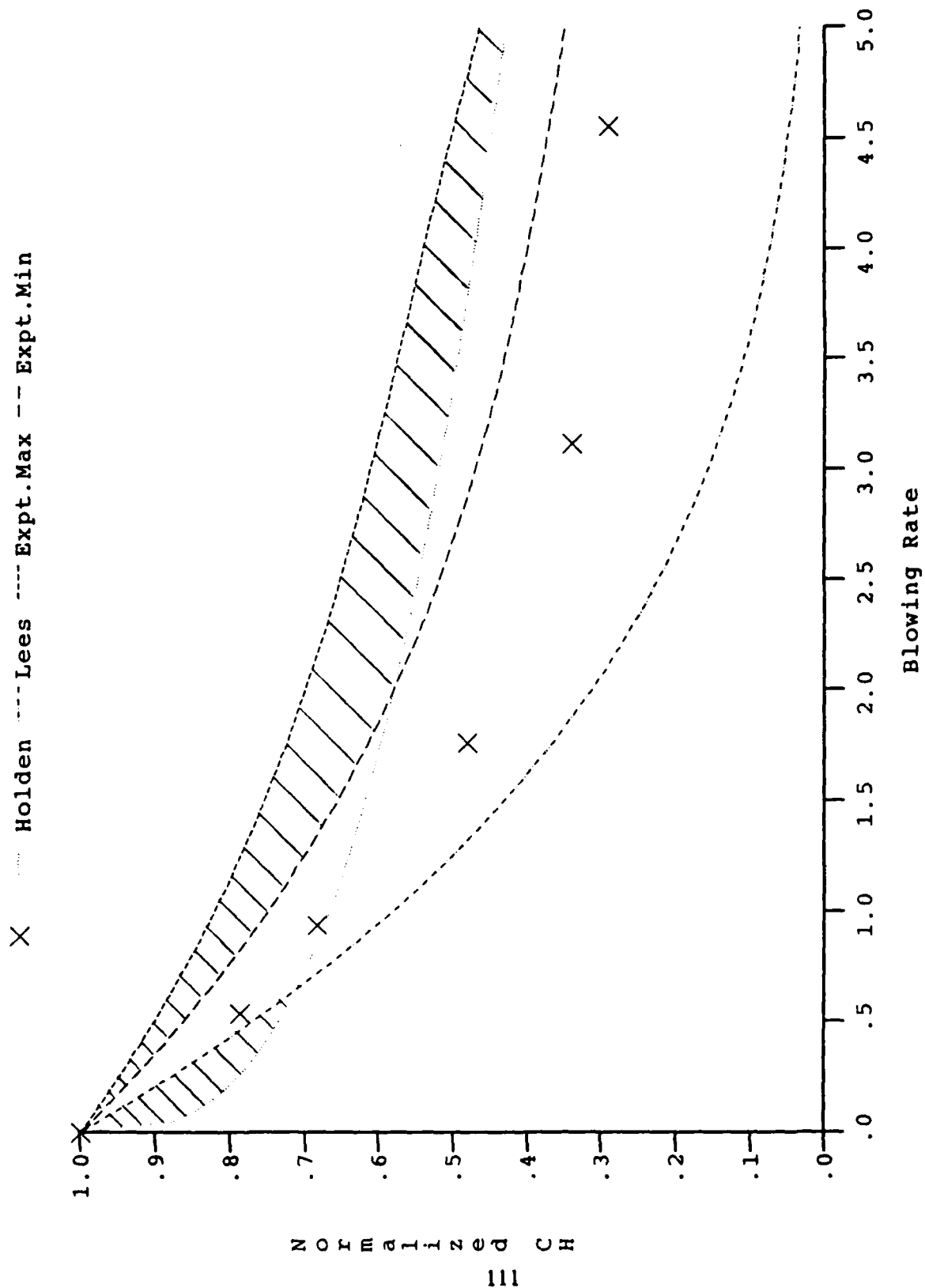Mach# = 11 (Normalized CH = CH / CHo)

110

Figure 64b. Variation of Normalized Base Heating with Blowing Rate
Mach# = 13 (Normalized CH = CH / CHo)

111

Figure 65a. Variation of Normalized Calorimeter Heating with Blowing Rat
Mach# = 11 (Normalized CH = CH / CHo)
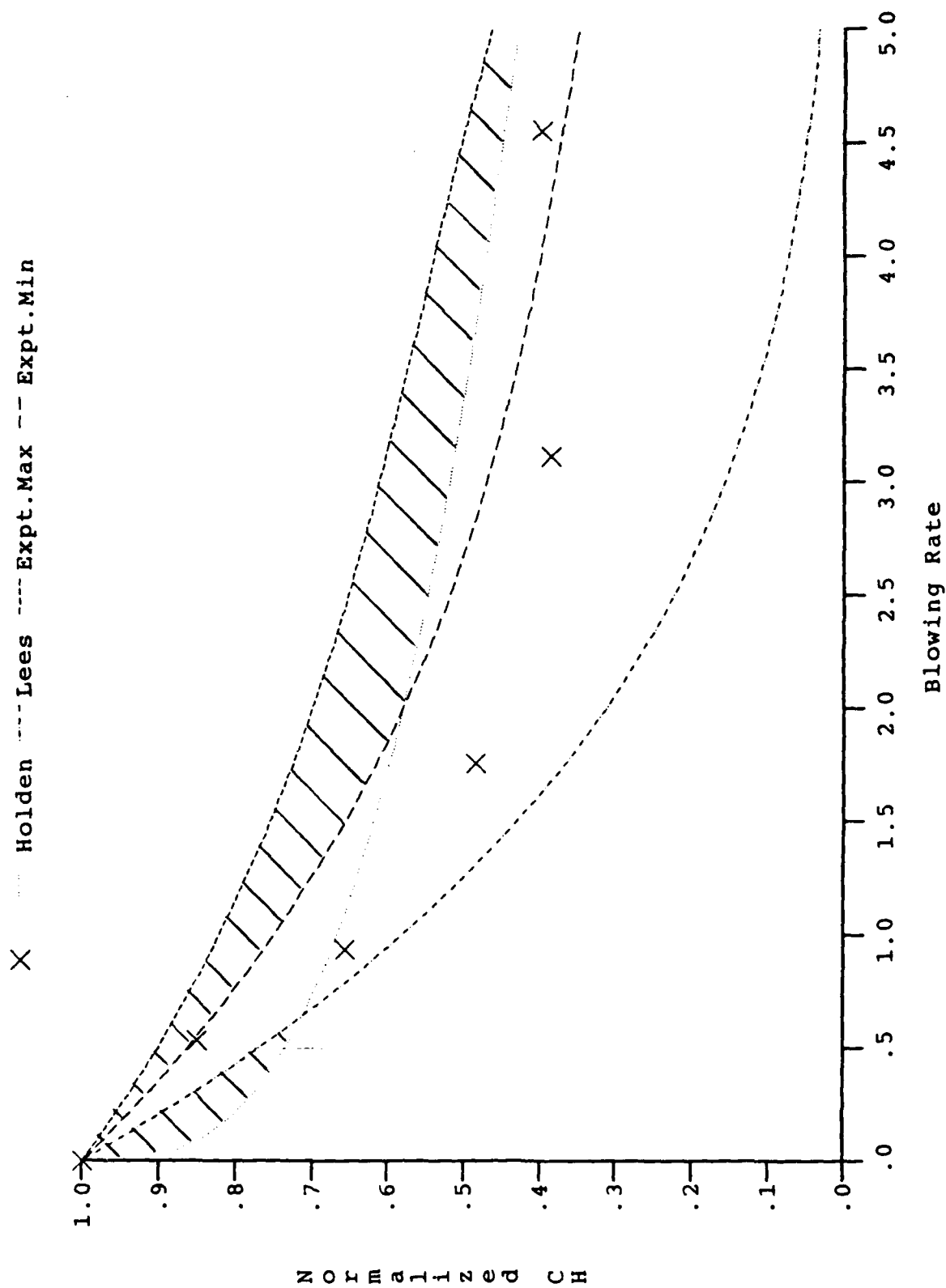
Figure 65b. Variation of Normalized Calorimeter Heating with Blowing Rat
Mach# = 13 (Normalized CH = CH / CHo)

113

X10**(-4)

$\times$ 0.231 $\square$ 0.705 $\diamond$ 1.751 $\bigcirc$ 4.083

C F

80
70
60
50
40
30
20
10
0
-10

0   5   10   15   20   25   30   35

Linear Distance from Nose Reference Joint (inches)

Figure 66a. Skin Friction Along Model for Various Blowing Rates
[Mach# = 15]

114
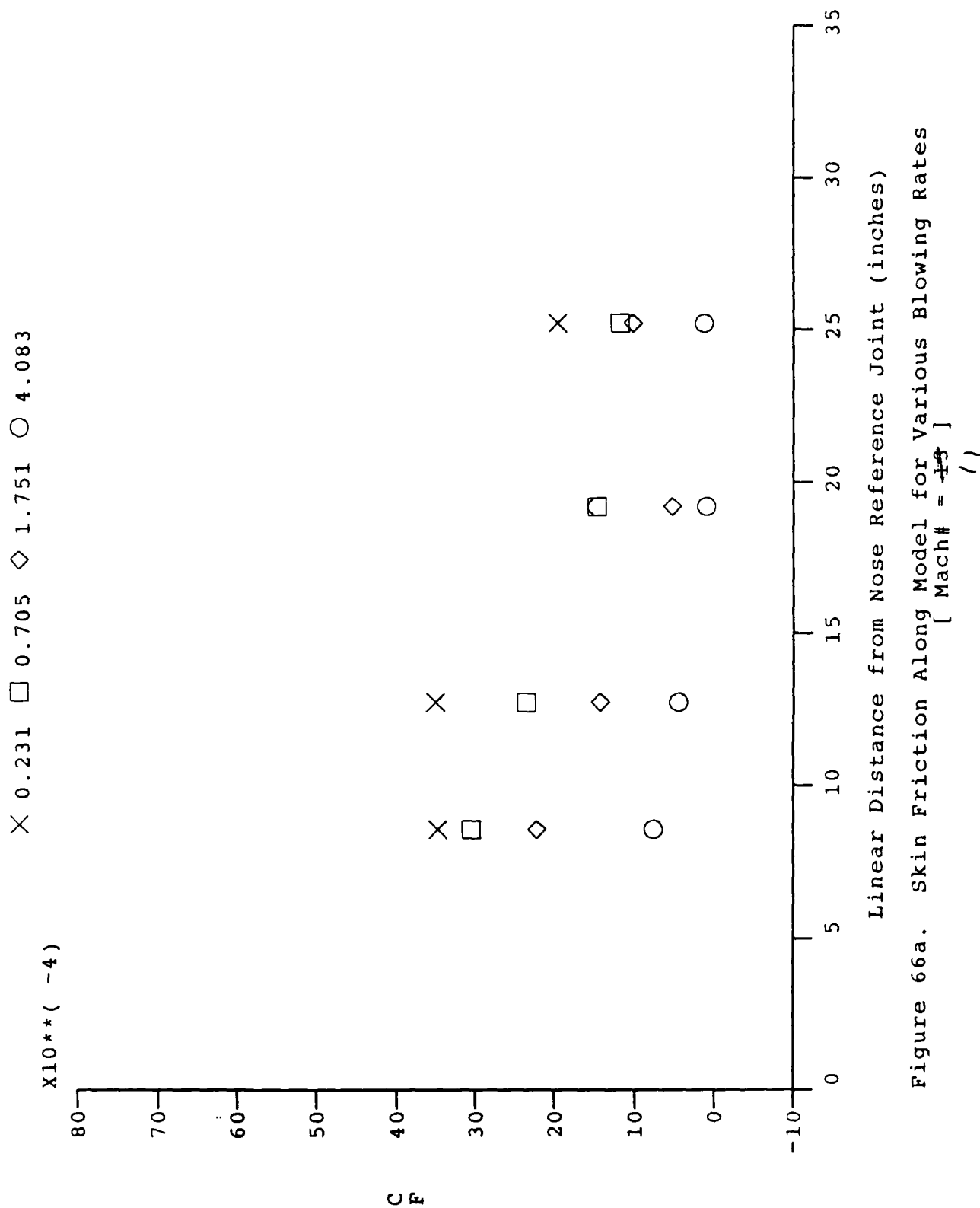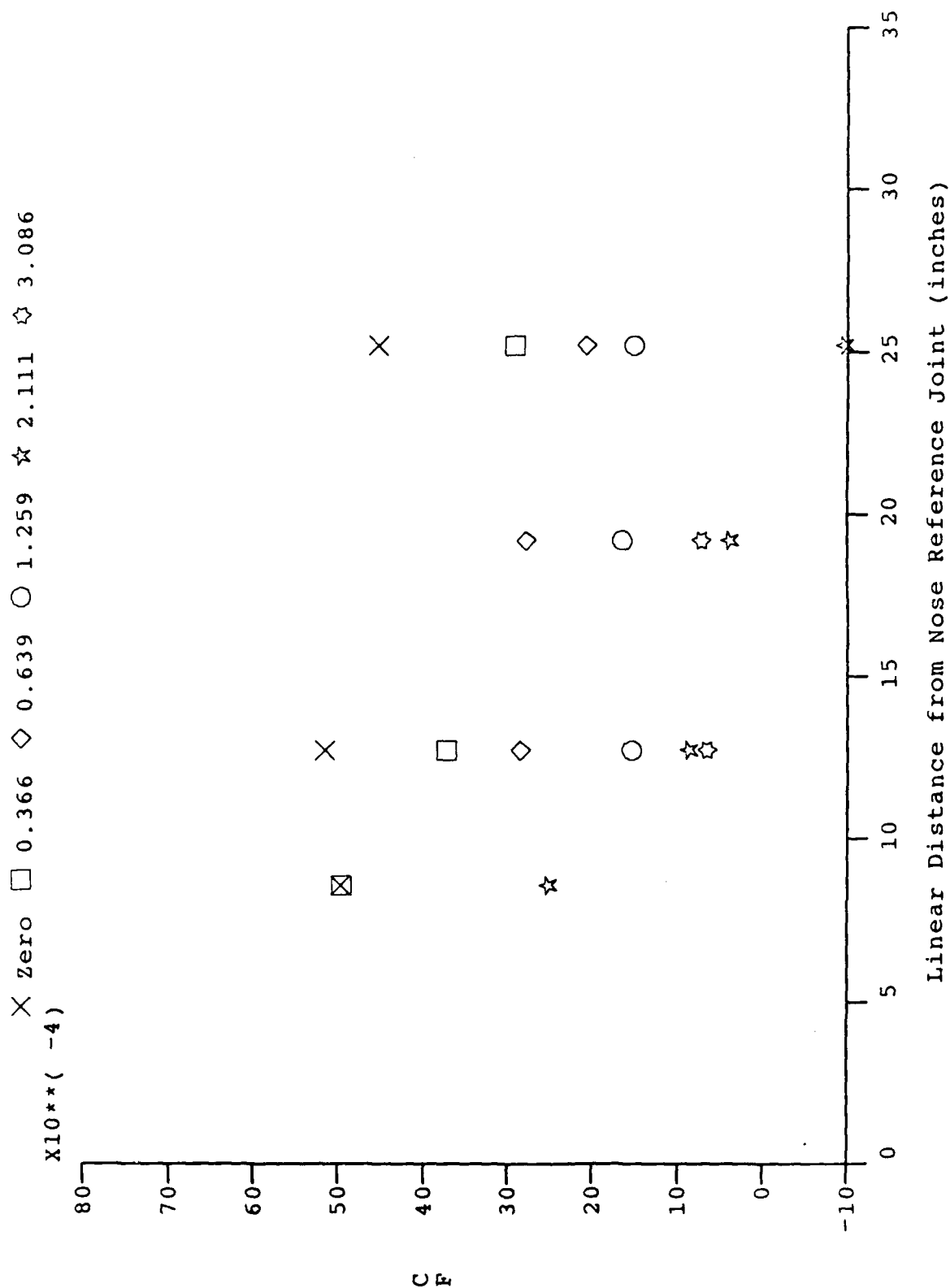
Figure 66b. Skin Friction Along Model for Various Blowing Rates
[Mach# = 13]

115

Figure 87a. Variation of Normalized Skin Friction with Blowing Rate
Mach# = 11 (Normalized CF = CF / CFo)

116

Figure 87b Variation of Normalized Skin Friction with Blowing Rate
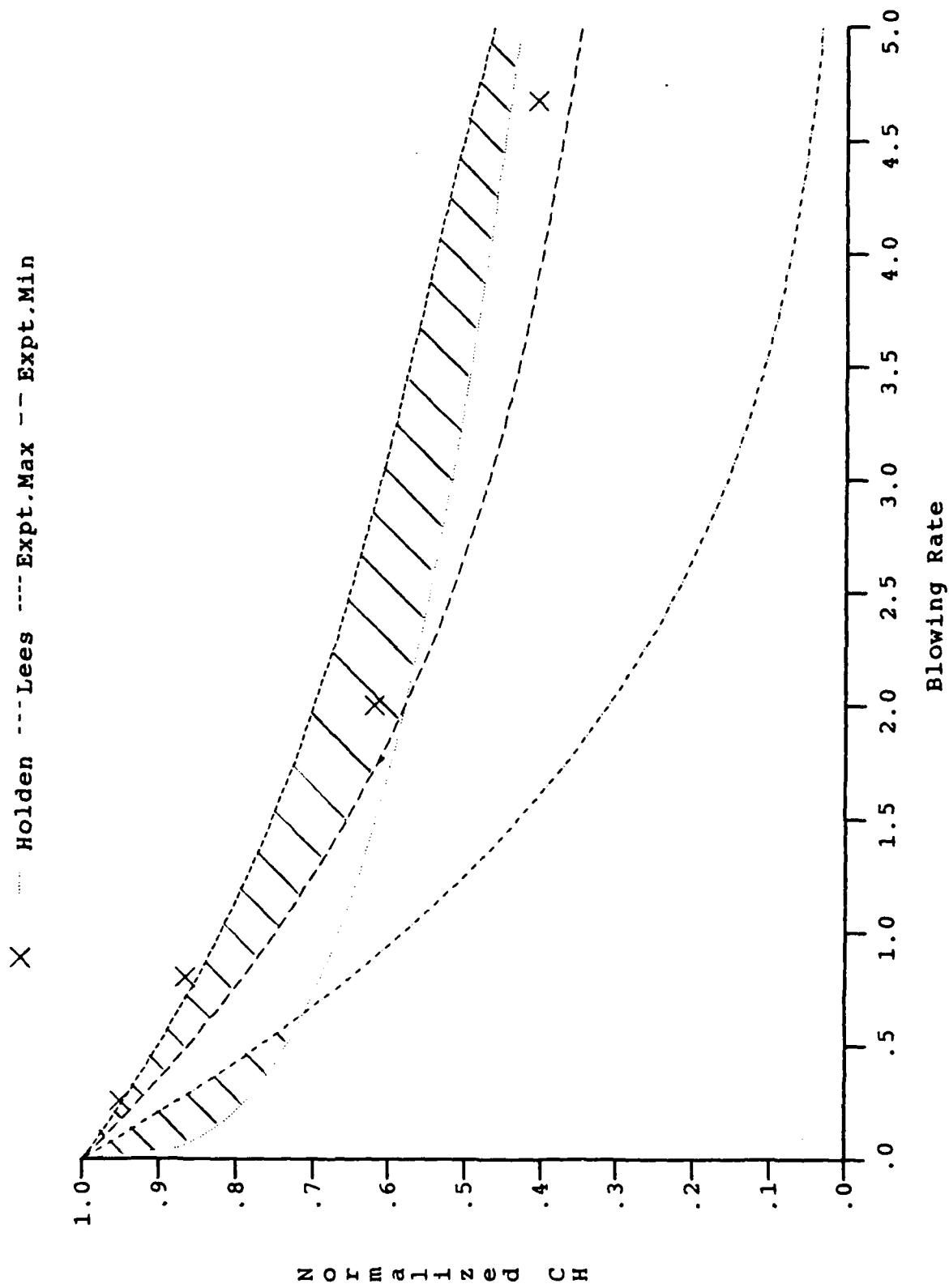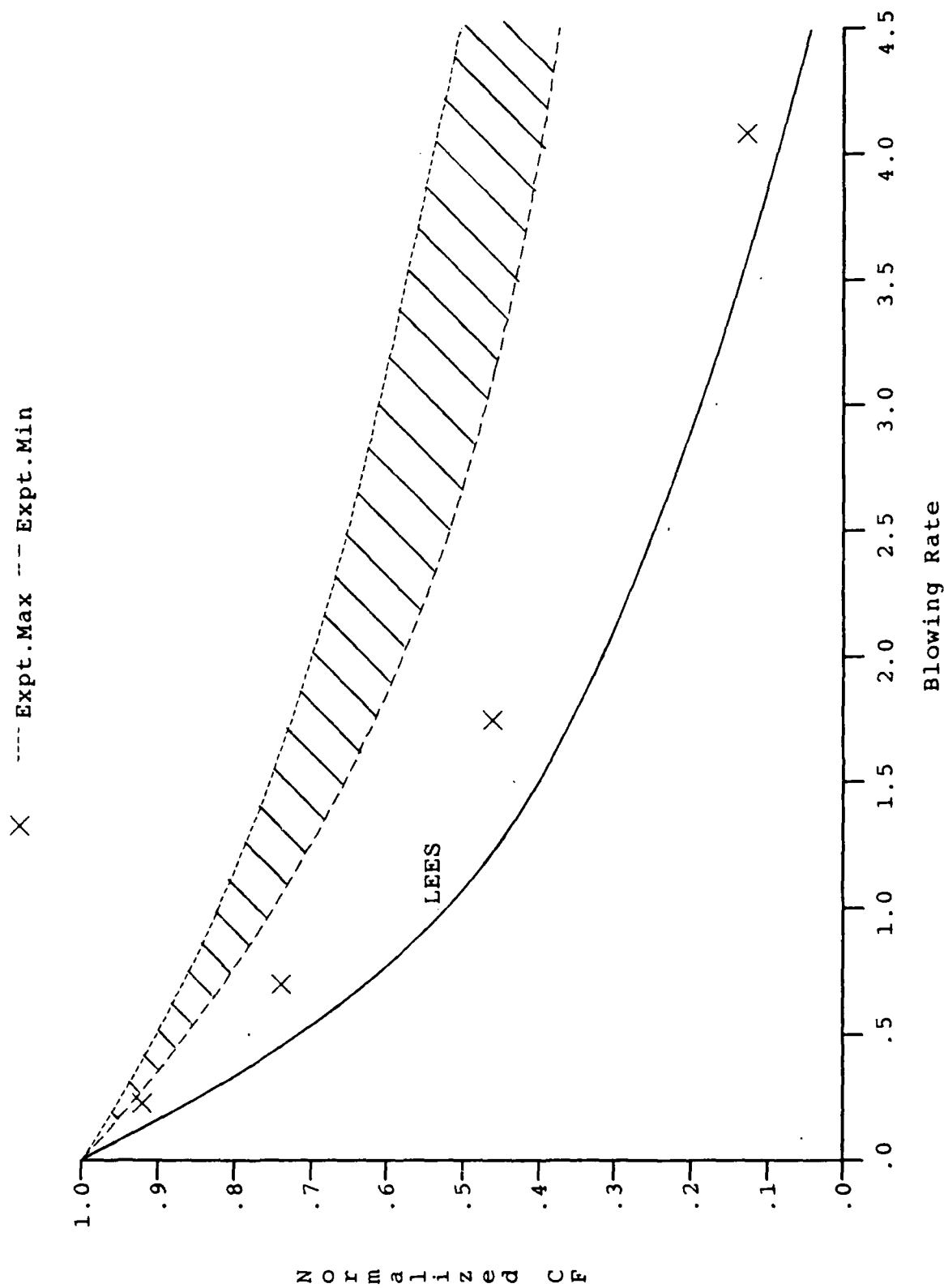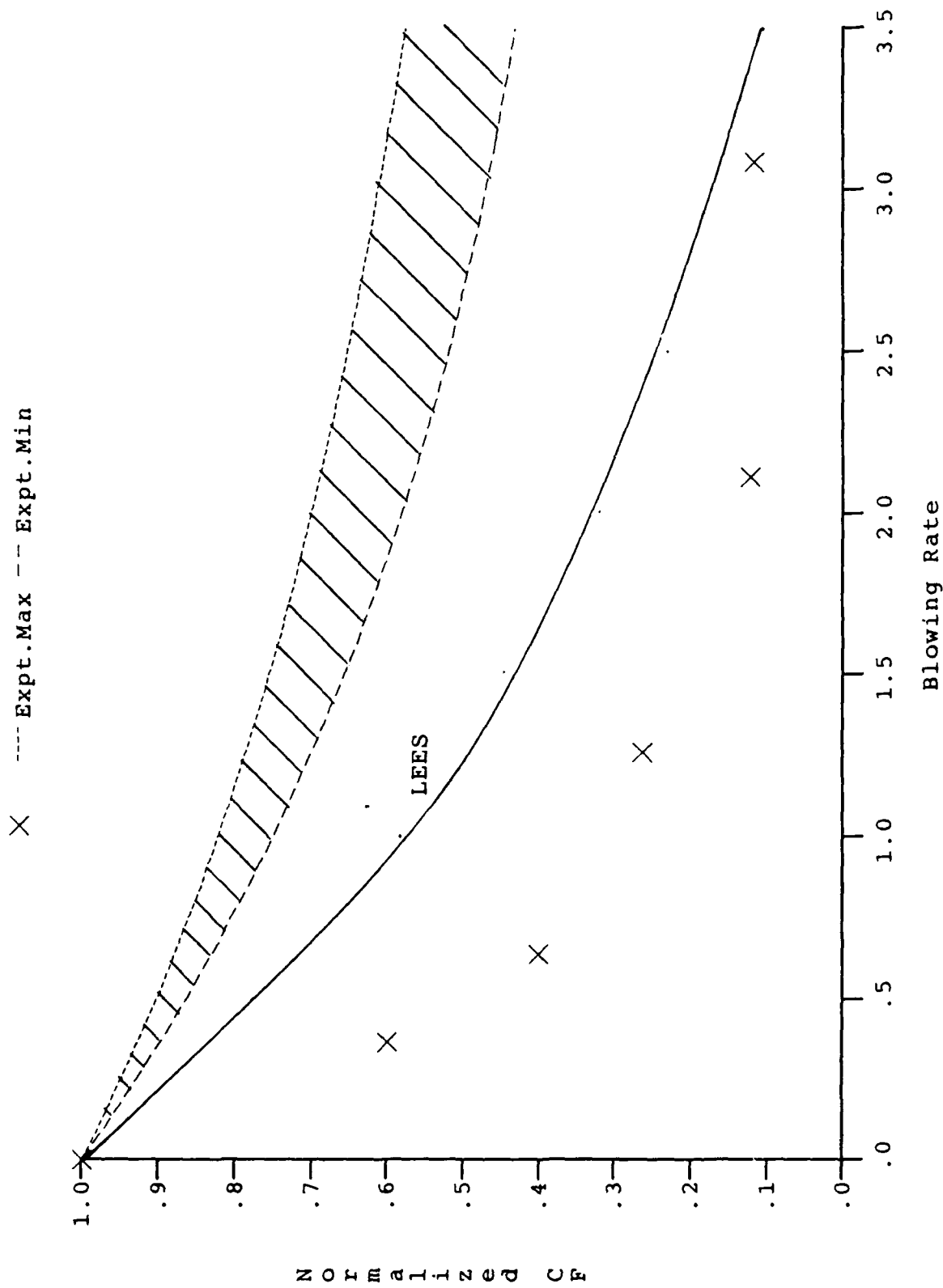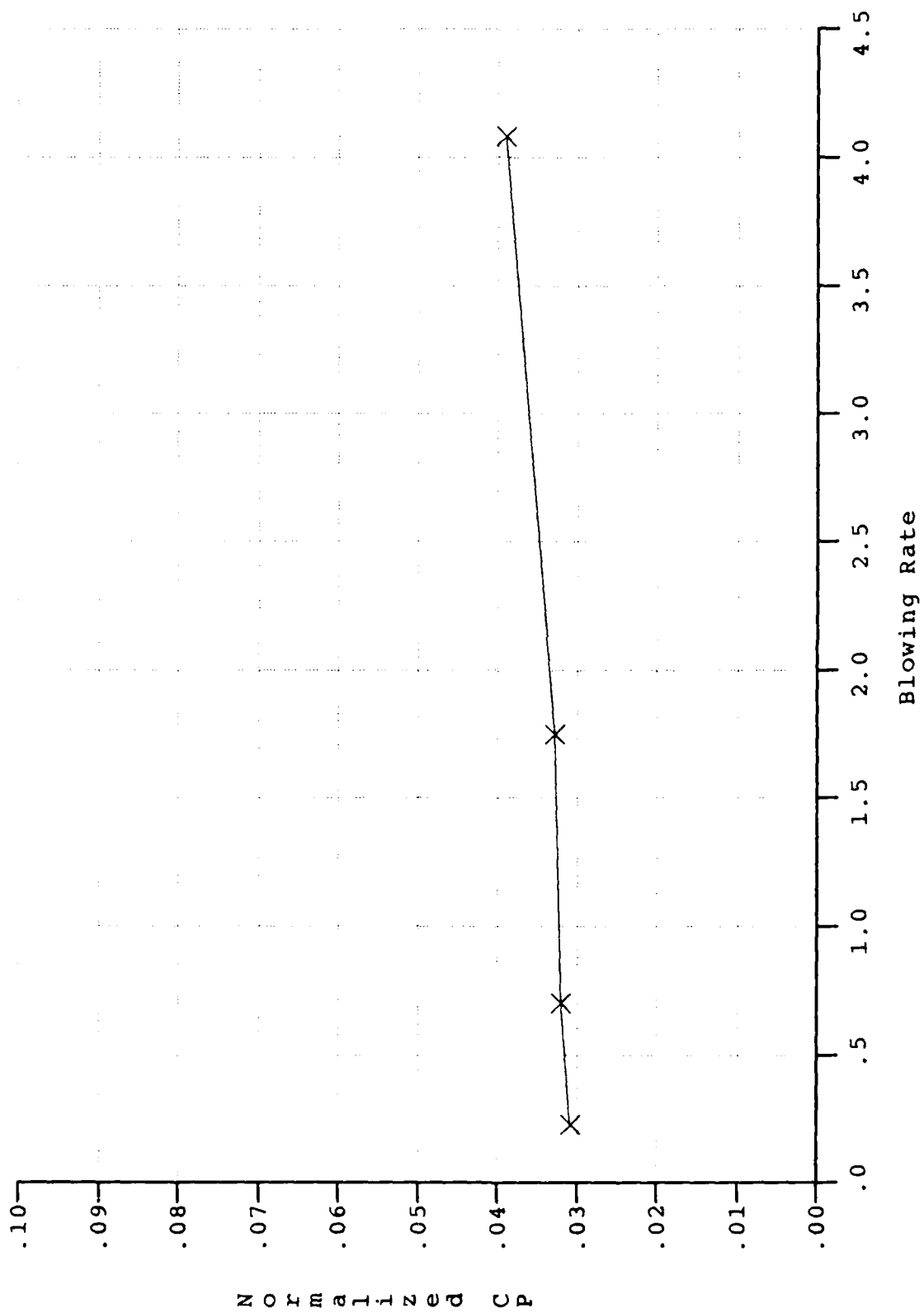Mach# = 13 (Normalized CF = CF / CFo)

117

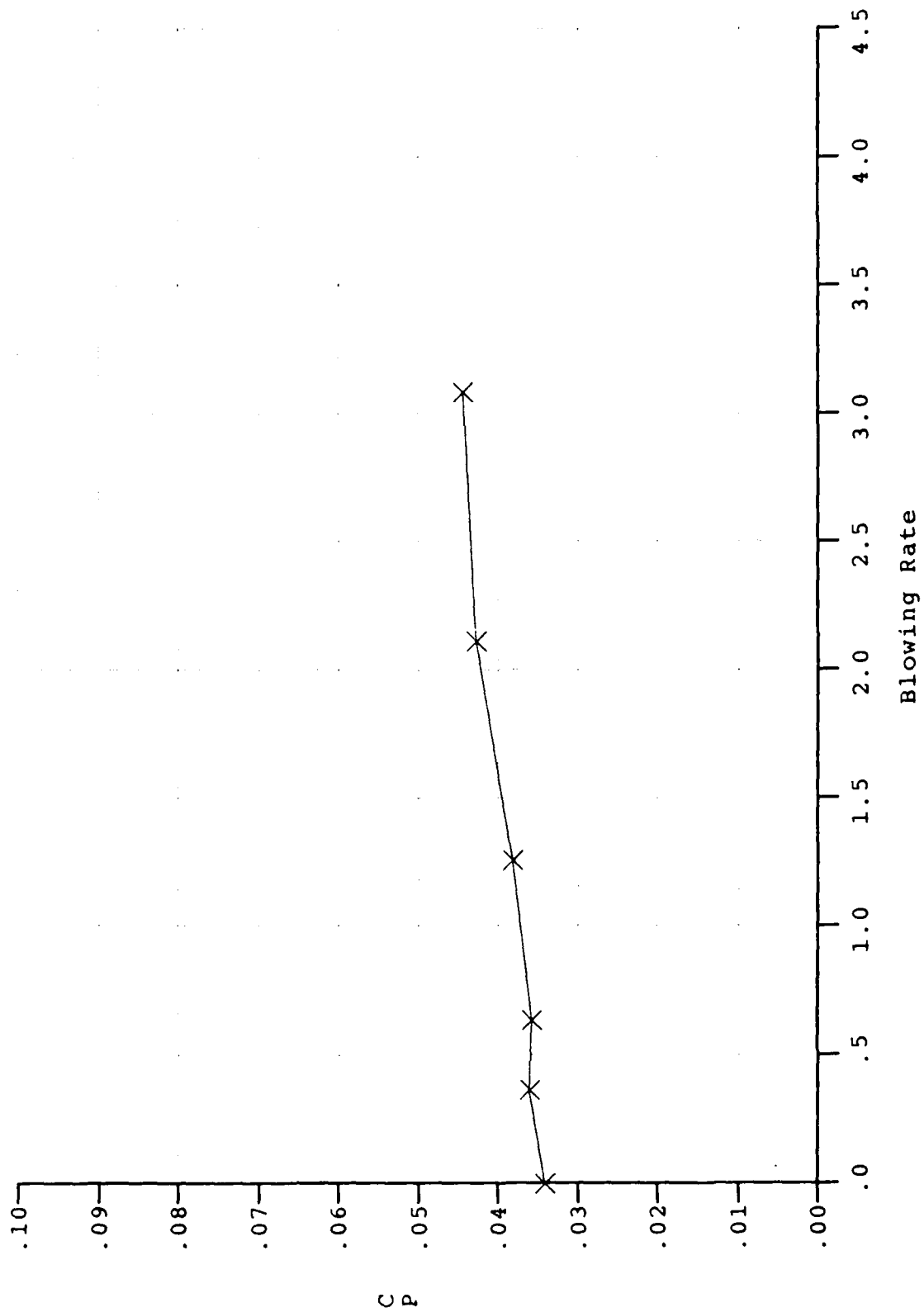Figure 68a   Variation of CP with Blowing Rate
Mach# = 11

118

Blowing Rate

Variation of CP with Blowing Rate
Mach# = 13

Figure 68b

the surface. This contention is supported by the pressure measurements shown in Figure 68 which suggest boundary "lift off" begins at values of blowing close to 1.

4.4 COMPARISONS WITH ANALYSIS AND EARLIER MEASUREMENTS

The experimental study of Voisinet[2] is the only published study which has provided information in supersonic flow on the effects of combined roughness and blowing on the skin friction to a rough porous surface. Since these studies were conducted for adiabatic wall conditions only skin friction measurements were made in this work. Almost all the theoretical approaches have investigated blowing effects on smooth surfaces, the work of Christoph[32] and Laganelli, et al[33] being the exceptions. The blowing parameter has been employed by the major segment of the community to correlate the skin friction data, where

$$B_f' = \frac{\dot{m}}{\rho_e u_e c_{F_o}}$$

where the equivalent parameter for heat transfer is

$$B_h' = \frac{\dot{m}}{\rho_e u_e c_{H_o}}$$

In the cases where the molecular weight of the injected gas differs from that of the freestream, parameters $(MW_{inj}/MW_{fs})^n$ and $(C_{p_{inj}}/C_{p_{fs}})^m$ are used to modify the skin friction and heat transfer parameters and respectively. For turbulent flows $n = 2/3$ and $m = 1$ have been selected. For flows over non-porous surfaces the relationship

$$\frac{c_f}{c_{f_o}} = \frac{B_f'}{(e^{B_f'} - 1)}$$

has been shown to be in good agreement with measurements in incompressible flows[34]. Further studies[35,36] which have included the effects of compressibility suggest that

$$\frac{c_{H_o} - c_H}{c_{H_o}} = \frac{1}{3} B_h'^{1/3}$$

is a better representation of the measurements.

In our studies there was a significant surface roughness effect at all the blowing conditions at Mach number significantly larger than the earlier work, therefore we cannot expect the earlier approaches to be totally valid. A comparison between our skin friction measurements and those of Voisinet[2] are shown in Figure 65 together

120

with the contemporary correlations for compressible flows. Here we see that our measurements fall above those of Voisinet[2] and more in line with the correlations of Walker[37] and Langanelli[33]. The heat transfer measurements plotted in an analogous format are shown in Figure 66.

Clearly we will have to await our studies on smooth bodies with and in the absence of blowing before we can make definitive statements on the effects of Mach numbers in these flows.

Section 5
CONCLUSIONS

Experimental studies have been conducted to examine the flow structure of regions of shock wave/turbulent boundary layer in hypersonic flow and the effects of roughness and blowing on attached and separated turbulent boundary layers. In the first of these studies the emphasis was on the development of sophisticated non-intrusive flowfield measurement techniques and miniature probes with which to explore the structure of complex interacting flows. Holographic interferometry and electron beam techniques were developed for use in the high Mach number high Reynolds number flows developed in a hypersonic shock tunnel. Also further refinements were made in the design and use of high frequency miniature pitot pressure and total temperature probes. In the studies of blowing and roughness, which was conducted in conjunction with a test program being conducted for AFWAL, a unique series of instrumentation were developed with which, for the first time, measurements were made of the heat transfer distribution over the roughness elements and the drag force on the roughness elements in the presence of blowing. Each program was focussed on providing detailed experimental measurements for the direct construction and verification of the models of turbulence used in the compressible time or mass-averaged Navier-Stokes equations.

A new holographic interferometry and reconstruction system, based on a system assembled by Haverner at AFWAL, was constructed specifically for studies of viscous interaction phenomena conducted in the Shock Tunnel. Measurements made using this system provide instantaneous (10 nanosecond) density contours through the interaction regions and provided further evidence to support the time-dependent nature of these flows. Measurements were made of the structure of the viscous layer and outer inviscid flow in the studies of blowing and roughness effects in hypersonic flow.

The development of the high density electron beam system provides a unique and complimentary high frequency density measurement system for density measurements up to 100 torr. Multiple systems are used to obtain simulataneous spatially-resolved fluctuations measurements across the boundary layer. This system has been calibrated and is being used to study the density fluctuations in a hypersonic turbulent boundary layer over a cone and in regions of shock wave/boundary layer interation.

In the studies of blowing and roughness effects on the characteristics of turbulent hypersonic boundary layers a unique set of measurements were obtained which provide the basis for the direct evaluation of the basic modelling of these phenomena in advanced codes. Models were constructed to simulate the separate and combined effects of roughness and blowing on the aerothermal characteristics of flows over cones with control flaps. Three new and unique transducers were developed to measure skin friction and local and average heating on rough transpiration-cooled surfaces. Experimental studies were conducted at Mach numbers of 11, 13 and 16 for turbulent flows in which the blowing parameter B' was varied from .01 to 10. Measurements and correlations are presented to show the effects of blowing on the distribution of skin friction and heat transfer over the cone/flap model and on the distribution of heating over the individual roughness elements.

REFERENCES

1. Holden, M.S., "Studies of Boundary Layer Transition and Surface Roughness Effects in Hypersonic Flow," Final Report, AFOSR Contract No. F49620-82-C-0026, October 1983.

2. Voisinet, R.L.P., "Combined Influence of Roughness and Mass Transfer on Turbulent Skin Friction at Mach 2.9", AIAA Paper 79-0003, 17th Aerospace Sciences Meeting, January 1979.

3. Holden, M.S., "Boundary Layer Displacement and Loading Edge Bluntness Effects on Attached and Separate Laminar Boundary Layer on a Compression Corner, Part II: Experimental Study," AIAA Journal, Vol. 9, No. 1, pp. 84-93, January 1971.

4. Bin, L.Z. & Harvey, J.K., "The Investigation of the Structure of Hypersonic Turbulent Boundary Layers on a 5^0 Sharp Cone Using the Electron Beam Fluorescence Technique," I.C. Aero Report, 82-02, January 1986.

5. Holden, M.S., Shock Wave Turbulent-Boundary Lyaer Interaction in Hypersonic Flow, AIAA 77-45.

6. Nikuradse, J., "Stromungsgeretze en rauken Rohren," VDI Forshuaq-shift No. 361, 1933, Translated as NACA TM 1292, 1950.

7. Schlichting, H., "Boundary Layer Theory," 4th Edition, McGraw Hill Book Co., New York, 1960.

8. Dvorak, F.A., "Calculation of Turbulent Boundary Layers with Roughness and Heat Transfer," AIAA Journal, 10, pp. 1447-1451, 1969.

9. Betterman, D., "Contribution of L'etude de la Couche Limite Turbuelent li Long Plagnes Rugueness," Rapport 65-5, Centre National de la Recherche Scientifique, Paris, France, 1965.

10. Lewis, M.J., "An Elementary Analysis for Predicting the Momentum- and Heat-Transfer Characteristics of a Hydraulically Rough Surface," Journal of Heat Transfer, 97, pp. 249-254, 1975.

11. Simpson, R.L., "A Generalized Correlation of Roughness Density Effects on the Turbulent Boundary Layer," AIAA Journal, Vol. II, N⌐ 2, pp. 242-244, 1973.

12. Lin, T.C. and Bywater, R.J., "The Evaluation of Selected Turbulence Models for High-Speed Rough-Wall Boundary Layer Calculations," AIAA Paper-80-0132, Pasadena, California, 1980.

13. Finson, J.L., and Wu, P.K.S., "Analysis of Rough Wall Turbulent Heating with Application to Blunted Flight Vehicles," AIAA Paper No. 79-0008, 17th Aerospace Science Meeting, 1979.

14. Goddard, F.E., Jr., "Effect of Uniformly Distributed Roughness on Turbulent Skin-Friction Drag at Supersonic Speeds," Journal of Aerospace Sciences, 26, pp. 1-15, 1959.

15. Dirling, R.B., Jr., "A Method for Computing Rough-Wall Heat Transfer Rates on Reentry Nosetips," MDAC Paper WD 1778, AIAA 8th Thermophysics Conference, Palm Springs, California, 1973.

16. Nikuradse, J., "Stromungsgeretze en rauken Rohren," VDI Forshuaq-shift No. 361, 1933, Translated as NACA TM 1292, 1950.

17. Schlichting, H., "Boundary Layer Theory," 4th Edition, McGraw Hill Book Co., New York, 1960.

18. Dirling, R.B., Jr., "A Method for Computing Rough-Wall Heat Transfer Rates on Reentry Nosetips," MDAC Paper WD 1778, AIAA 8th Thermophysics Conference, Palm Springs, California, 1973.

19. Simpson, R.L., "A Generalized Correlation of Roughness Density Effects on the Turbulent Boundary Layer," AIAA Journal, Vol. II, No. 2, pp. 242-244, 1973.

20. Finson, J.L., and Wu, P.K.S., "Analysis of Rough Wall Turbulent Heating with Application to Blunted Flight Vehicles," AIAA Paper No. 79-0008, 17th Aerospace Science Meeting, 1979.

21. Healzer, J.M., Moffat, R.J. and Kays, W.M., "The Turbulent Boundary Layer on a Rough Porous Plate: Experimental Heat Transfer with Uniform Blowing," Report No. HMT-18, Thermosciences Division Dept. of Mech. Eng., Stanford University, 1974.

22. Voisinet, R.L.P., "Influence of Roughness and Blowing on Compressible Turbulent Boundary Layer Flow," Naval Surface Weapons Center, NSWC Report No. TR-79-153, June 1979.

23. Nikuradse, J., "Stomungsgeretze en rauken Rohren," VDI Forshuaq-shift No. 361, 1933, Translated as NACA TM 1292, 1950.

24. Dirling, R.B., Jr., "A Method for Computing Rough-Wall Heat Transfer Rates on Reentry Nosetips," MDAC Paper WD 1778, AIAA 8th Thermophysics Conference, Palm Springs, California, 1973.

25. Healzer, J.M., Moffat, R.J. and Kays, W.M., "The Turbulent Boundary Layer on a Rough Porous Plate: Experimental Heat Transfer with Uniform Blowing," Report No. HMT-18, Thermosciences Division Dept. of Mech. Eng., Stanford University, 1974.

26. Voisinet, R.L.P., "Influence of Roughness and Blowing on Compressible Turbulent Boundary Layer Flow," Naval Surface Weapons Center, NSWC Report No. TR-79-153, June 1979.

27. Goddard, F.E., Jr., "Effect of Uniformly Distributed Roughness on Turbulent Skin-Friction Drag at Supersonic Speeds," Journal of Aerospace Sciences, 26, pp. 1-15.

28. Reda, D.C., "Compressible Turbulent Skin Friction on Rough and Rough/Wavy Walls in Adiabatic Flow," Naval Ordnance Laboratory, Report No. NOLTR 74-34, Silver Springs, MD., 1974.

29. Finson, J.L., and Wu, P.K.S., "Analysis of Rough Wall Turbulent Heating with Application to Blunted Flight Vehicles," AIAA Paper No. 79-0008, 17th Aerospace Science Meeting, 1979.

30. Lin, T.C. and Bywater, R.J., "The Evaluation of Selected Turbulence Models for High-Speed Rough-Wall Boundary Layer Calculations," AIAA Paper-80-0132, Pasadena, California, 1980.

31. Nikuradse, J., "Stromungsgeretze en rauken Rohren," VDI Forshuaq-shift No. 361, 1933, Translated as NACA TM 1292, 1950.

32. Christoph, G.H., "Low-Of-The-Wall Analysis Revisited for Reentry Vehicle Design," AIAA Paper 85-0905, Williamsburg, Virginia, 1985.

33. Laganelli, A.L., Foganoli, R.P., and Martellucci, A., "The Effects of Mass Transfer and Angle of Attack on Hypersonic Turbulent Boundary Layer Charcteristics," AFFDL-TR 75-35, April 1975.

34. Kays, W.M. and Moffat, R.J., "The Behavior of Transpired Turbulent Boundary Layers," Stanford University, Report No. H MT-20, April 1975.

35. Rubesin, M.W., "An Analytical Estimation of the Effect of Transpiration Cooling on the Heat-Transfer and Skin-Friction Characteristics of a Compressible Turbulent BOundary Layer," NACA TN 3341, December 1954.

36. Dorrance, W.H., and Dore, F.J., "The Effect of Mass Transfer on the Compressible Turbulent Boundary-Layer Skin Friction and Heat Transfer," J. Aeronautical Sciences, June 1954.

37. Walker, G.K., "Turbulent Boundary Layers with Mass Addition," G.E. Document No. TFM-8151-021, November 1963.